University of South Carolina
Scholar Commons

Theses and Dissertations

2018

Investigation Of The Spatial Dependence Of Carrier Dynamics In Semiconductor Optoelectronic Devices

Bobby G. Barker Jr.
University of South Carolina

Follow this and additional works at: https://scholarcommons.sc.edu/etd

Part of the Chemistry Commons

Recommended Citation
Barker, B. G.(2018). *Investigation Of The Spatial Dependence Of Carrier Dynamics In Semiconductor Optoelectronic Devices.* (Doctoral dissertation). Retrieved from https://scholarcommons.sc.edu/etd/4696

This Open Access Dissertation is brought to you by Scholar Commons. It has been accepted for inclusion in Theses and Dissertations by an authorized administrator of Scholar Commons. For more information, please contact digres@mailbox.sc.edu.

Investigation of the Spatial Dependence of Carrier Dynamics in Semiconductor Optoelectronic Devices

by

Bobby G Barker, Jr.

Bachelor of Science
University of Kentucky, 2013

Submitted in Partial Fulfillment of the Requirements

For the Degree of Doctor of Philosophy in

Chemistry

College of Arts and Sciences

University of South Carolina

2018

Accepted by:

Andrew B. Greytak, Major Professor

Donna Chen, Committee Member

Natalia Shustova, Committee Member

MVS Chandrashekhar, Committee Member

Cheryl L. Addy, Vice Provost and Dean of the Graduate School

© Copyright by Bobby G. Barker, Jr., 2018
All Rights Reserved.

DEDICATION

This dissertation is dedicated to my parents, who are always there to support me throughout my Ph.D. and my entire life. Their positive reinforcement, care, and education from a young age have set me up for success and I could not have had any successes without them.

ACKNOWLEDGEMENTS

I would like to express my deepest appreciation to my advisor Dr. Andrew B. Greytak for his continuous guidance and support of my Ph.D. studies. His patience, motivation, enthusiasm, and knowledge have made me feel comfortable and welcome. His help and ability to teach me content that I didn't initially understand at an instant has increased my knowledge tenfold.

Apart from my advisor, I would like the acknowledge my committee members: Dr. Donna Chen, Dr. Natalia Shustova, and Dr. MVS Chandrashekhar for their guidance and wisdom. I would like to thank them for being a part of my committee and for their ability to congratulate me when I have done well and politely disclose when they expect more of me.

I would also like to thank the NSF IGERT program as well as the lovely people at the National Institute for Materials Science in Japan for their hospitality. Dr. Kenjiro Miyano, Dr. Masatoshi Yanagida, Dr. Yasuhiro Shirai, Dr. Kunie Ishioka, and Hiromi Chinone welcomed me warmly to a new country and new experiences – both scientifically and culturally in Japan.

Lastly, I would like to express my gratitude to my co-workers, past and present. To Dr. Rui Tan, Dr. Yi Shen, Dr. Pravin Paudel, Megan Gee, Preecha Kittikhunnatham, Adam Roberge, Stephen Roberts, Mathew Kelley, John Dunlap, Fiaz Ahmed, Colin Johnson, Abby Loszko, and Cole Love-Baker, I appreciate your thoughts, criticisms, and entertainment you have provided me over the last few years.

ABSTRACT

Optoelectronic devices, such as solar cells and photodetectors, rely on separating and transporting charge through semiconductors that have excess electron-hole pairs created by photon absorption. This talk will focus of several different semiconductor materials of various dimensionality, such as lead halide perovskites, wide bandgap SiC, graphene, semiconductor nanowires (NWs), and quantum dots (QDs).

The results of Chapter 2 demonstrate the dependence of the perovskite/hole transport layer on carrier transport of perovskite films for solar cells. Efficient charge separation at the interfaces of the perovskite with the carrier transport layers is crucial for perovskite solar cells to achieve high power conversion efficiency. A systematic experimental study on the hole injection dynamics from $MAPbI_3$ perovskite to three typical hole transport materials (HTMs) is discussed.

Graphene layers grown epitaxially on SiC substrates are attractive for a variety of sensing and optoelectronic applications because the graphene acts as a transparent, conductive, and chemically responsive layer that is mated to a wide-bandgap semiconductor with large breakdown voltage. Recent advances in control of epitaxial growth and doping of SiC epilayers have increased the range of electronic device architectures that are accessible with this system. In particular, a recently introduced Schottky-emitter bipolar phototransistor (SEPT) based on an epitaxial graphene (EG) emitter grown on a p-SiC base epilayer has been found to exhibit a maximum common emitter current gain of 113 and a UV responsivity of 7.1 A W^{-1}. In Chapter 3, the sub-

bandgap performance of the device is addressed, and a visible rejection ratio is calculated. Additionally, scanning photocurrent microscopy (SPCM) shows the localized effects of the photocurrent and the presence of an 8H- stacking fault. A new device fabricated with a thinner base region and SiF_4 mediated EG growth process will be studied in Chapter 4. The spatial response of the photocurrent allows for determination of the visible rejection ratio, as well as a model of how generated carriers interact within the device.

Nanoscale optoelectronic devices of semiconductor CdS nanowires (NWs) and PbS quantum dots (QDs) are investigated in Chapter 5. The fabrication techniques, responsivities, on/off ratio, and spatial dependence of the devices will be discussed.

PREFACE

The dissertation is based on original work by the author, Bobby G. Barker, Jr. with the advice and collaboration of Dr. Andrew Greytak and members of his research group.

A version of Chapter 2 has been published in *The Journal of Physical Chemistry Letters*. Reprinted with permission from Ishioka, K.; Barker, B. G.; Yanagida, M.; Shirai, Y.; Miyano, K. *J. Phys. Chem. Lett.* **2017**, *8* (16), 3902–3907. http://pubs.acs.org/doi/10.1021/acs.jpclett.7b01663. Copyright 2017 American Chemical Society. I was the second author for this manuscript. I was the lead designer of the experiment, device fabrication, and collection of data, except for the transient transmission data and analysis. Kunie Ishioka was in charge of transient transmission measurements and analysis, as well as the primary leader in manuscript composition. Masatoshi Yanagida, Yashuo Shirai, and Kenjiro Miyano were all supervisory authors and were involved in the entirety of the project through concept formation and manuscript edits. This project was supported and possible through the National Science Foundation Integrated Graduate Research Traineeship program.

A version of Chapter 3 has been published in *2D Materials*. Reprinted with permission from Barker, B. G.; Chava, V. S. N.; Daniels, K. M.; Chandrashekhar, M. V. S.; Greytak, A. B. *2D Mater.* **2018**, *5* (1). https://doi.org/10.1088/2053-1583/aa90b1. Copyright 2018 IOP Publishing. The major experimental design and execution was performed by myself. The manuscript was primarily written by Andrew Greytak and myself with comments

and revisions from Venkata Surya N. Chava and MVS Chandrashekhar. Andrew Greytak and MVS Chandrashekhar were the supervisory authors on this project and were involved from concept formation to manuscript edits.

A portion of Chapter 4 has been published in *Applied Physics Letters*. Reprinted with permission from Chava, V. S. N.; Barker, B. G.; Balachandran, A.; Khan, A.; Simin, G.; Greytak, A. B.; Chandrashekhar, M. V. S. *Appl. Phys. Lett.* **2017**, *111* (24), 243504. https://doi.org/10.1063/1.5009003. Copyright 2017 Applied Physics Letters. The major experimental design and execution were performed by Venkata Surya N. Chava, as well as the manuscript writing. I was responsible for scanning photocurrent measurements and analysis. All authors contributed to manuscript revisions. MVS Chandrashekhar and Andrew Greytak were the supervisory authors on this project and were involved from concept formation to manuscript edits. Apart from this work, the rest of Chapter 4 is an original, unpublished project, where I was responsible for all major areas of data collection and analysis, as well as majority of the manuscript composition. Andrew Greytak and MVS Chandrashekhar were the supervisory authors on this project and were involved from the beginning of the project.

Chapter 5 is an original, unpublished project, where I was responsible for all major areas of data collection and analysis, as well as manuscript composition. Mathew Kelley Fiaz Ahmed, and Cole Love-Baker assisted with quantum dot device fabrication and data collection. Preecha Kittikhunnatham assisted with nanowire device fabrication. Andrew Greytak was the supervisory author on this project.

TABLE OF CONTENTS

Dedication iii

Acknowledgements iv

Abstract v

Preface vii

List of Tables xiii

List of Figures xiv

List of Abbreviations xvii

Chapter 1: Introduction to Charge Carriers in Semiconductor Materials 1

1.1 Semiconductors 1

1.2 Optoelectronic devices (solar cells and photodetectors) 2

1.3 Electronic transport in semiconductor materials 3

1.4 Scanning photocurrent microscopy 4

1.5 Emerging material systems and reduced dimensionality 7

1.6 Dissertation overview 14

Chapter 2: Direct Observation of Ultrafast Hole Injection from Lead Halide Perovskite by Differential Transient Transmission Spectroscopy 16

2.1 Preface 16

2.2 Introduction 17

2.3 Scanning electron microscopy and X-ray diffraction of $MAPBI_3$ films 20

2.4 Absorption characteristics of $MAPBI_3$ films 22

2.5 Emission spectra and fluorescence decay lifetime of $MAPbI_3$ films 22

2.6 Change in transient transmission of $MAPbI_3$ films measured from the near and far side of the HTM/PVK interface 23

2.7 Differential transient transmission of $MAPbI_3$ films paired with HTMs 27

2.8 Modeling the hole diffusion in perovskites to compare with the differential transient transmission results 29

2.9 Solar cell efficiency featuring the previously studied HTMs 31

2.10 Conclusions 34

2.11 Methods and materials 35

Chapter 3: Sub-bandgap Response of Graphene/SiC Schottky Emitter Bipolar Phototransistor Examined by Scanning Photocurrent Microscopy 41

3.1 Introduction 41

3.2 SPCM experimental setup and device operation..44

3.3 SPCM results under normal device operation..46

3.4 Responsivity, absorption, gain, and visible rejection ratio in graphene-emitter mode 49

3.5 Responsivity, absorption, gain, and visible rejection ratio in graphene-collector mode 50

3.6 Localized photocurrent signals – including an 8H- stacking fault 52

3.7 Band-edge response and investigation of the origins of sub-bandgap photocurrent 54

3.8 Carrier transport characteristics of EG/SiC device from SPCM and the origins

of photocurrent enhancement from an 8H- stacking fault.......................................59

3.9 Summary and future work..62

3.10 Methods and materials 63

Chapter 4: Ultraviolet and Phase-sensitive Photocurrent Mapping Reveals Large Visible Rejection Ratio and Non-local Current Generation in Epitaxial

Graphene/SiC Bipolar Phototransistors 65

4.1 Introduction 65

4.2 Device properties....................66

4.3 Initial investigation of the device 68

4.4 Scanning photocurrent images in Schottky emitter mode....................72

4.5 Scanning photocurrent images in Schottky collector mode 74

4.6 Small area excitation current-voltage characteristics 76

4.7 Photocurrent mapping of neighboring floating devices 79

4.8 AC versus DC characteristics....................82

4.9 Working hypothesis of device operation....................83

4.10 Summary and future work....................86

4.11 Methods and materials 86

Chapter 5: Photocurrent Study of Cadmium Sulfide Nanowires and Lead Sulfide Quantum Dots 89

5.1 Introduction 89

5.2 Nanowire growth....................91

5.3 Nanowire device preparation 92

5.4 Nanowire photocurrent measurements....................94

5.5 Quantum dot device preparation 98

5.6 Quantum dot photocurrent measurements....................100

5.7 SPCM of quantum dot device 103

5.8 Summary and future work....................103

5.9 Methods and materials 104

References....................109

Appendix A – Copyright Permissions 131

LIST OF TABLES

Table 2.1 Device parameters for solar cells with three different HTMs 33

Table 3.1 Responsivity of a SEPT device at V_{CE} = 60 (graphene emitter)........................50

LIST OF FIGURES

Figure 1.1 Scanning photocurrent microscope diagram 5

Figure 1.2 Example data of scanning photocurrent experiment 7

Figure 2.1 Experimental design 19

Figure 2.2 SEM and XRD of $MAPbI_3$ films 20

Figure 2.3 Absorption and external quantum efficiency of $MAPbI_3$ with and without HTMs 21

Figure 2.4 Emission and fluorescence lifetime decay of $MAPbI_3$ with and without HTMs 23

Figure 2.5 Transient transition of $MAPbI_3$ with and without HTMs................................24

Figure 2.6 Pump density dependence of transient transmission of $MAPbI_3$ 25

Figure 2.7 Different transient transmission of $MAPbI_3$ films with and without HTMs 28

Figure 2.8 Calculated hole distributions as a function of distance from the $MAPbI_3$/HTM interface 30

Figure 2.9 Calculation of carrier density in the absence of HTM as a function of distance from the surface 31

Figure 2.10 Calculated carrier distributions as a function of distance at varying times 32

Figure 2.11 Current density-voltage curves for solar cells with three different HTMs.....33

Figure 2.12 Reflectance, external quantum efficiency, and internal quantum efficiency of solar cells with three different HTMs 34

Figure 3.1 SPCM setup for analysis of EG/SiC SEPT device 43

Figure 3.2 Band diagrams of EG/SiC SEPT devices at different voltages 45

Figure 3.3 SPCM and current-voltage characteristics of an EG/SiC SEPT device 46

Figure 3.4 SPCM maps of an EG/SiC device in graphene emitter mode 47

Figure 3.5 Current-voltage characteristics of an EG/SiC SEPT device under UV illumination 48

Figure 3.6 Estimation of the absorption length of donor-acceptor pair absorption 51

Figure 3.7 SPCM map and current-voltage characteristic of a localized 8H- defect 54

Figure 3.8 Photocurrent of an EG/SiC SEPT device versus laser power 55

Figure 3.9 Action spectrum of SEPT devices 55

Figure 3.10 Photocurrent absorption function versus optical bandgap of SEPT devices ..57

Figure 3.11 Band structure of EG/SiC in graphene emitter mode showing visible and UV absorption mechanisms 61

Figure 4.1 Description of previous and studied EG/SiC SEPT devices and band diagrams of EG/SiC SEPT devices at different voltages 67

Figure 4.2 Current-voltage characteristics of EG/SiC SEPT device under wide-area Illumination in Schottky collector and Schottky emitter modes..69

Figure 4.3 SPCM maps of an EG/SiC device in Schottky emitter mode 73

Figure 4.4 SPCM maps of an EG/SiC device in Schottky collector mode........................75

Figure 4.5 Current-voltage characteristics of an EG/SiC SEPT device............................77

Figure 4.6 SPCM maps of neighboring EG mesas to an EG/SiC SEPT device 80

Figure 4.7 SPCM and phase maps of neighboring EG mesas to an EG/SiC SE device 81

Figure 4.8 Schottky emitter characteristics versus distance 83

Figure 4.9 Working illustration of the device with varying excitation locations 85

Figure 5.1 SEM and TEM images of CdS and CdSe VLS growth nanowires 92

Figure 5.2 Device preparation of CdS nanowire devices 93

Figure 5.3 Device pattern for nanowire devices 95

Figure 5.4 Current-voltage characteristics of a CdS nanowire photodetector 96

Figure 5.5 Persistent photocurrent of a CdS nanowire 97

Figure 5.6 Absorption spectrum of PbS quantum dots 99

Figure 5.7 SEM images of a PbS-EDT quantum dot film 100

Figure 5.8 Current-voltage characteristics of PbS-EDT quantum dot photodetector 101

Figure 5.9 SPCM of quantum dot photodetector 102

LIST OF ABBREVIATIONS

2DEG .... Two-Dimensional Electron Gas

2DHG .... Two-Dimensional Hole Gas

3-D .... Three Dimensional

3SSF .... Triple Shockley Stacking Fault

4SSF .... Quadruple Shockley Stacking Fault

AZO .... Aluminum-Doped Zinc Oxide

BJT .... Bipolar-Junction Transistor

CBM .... Conduction Band Minima

DAP .... Donor-Acceptor Pair

DCS .... Dichlorosilane

EDT 1,2-ethanedithiol

EG .... Epitaxial Graphene

EQE .... External Quantum Efficiency

ETL .... Electron Transport Layer

ETM .... Electron Transport Material

FET .... Field-Effect Transistor

FTIR .... Fourier Transform Infrared Reflectance

GPC .... Gel Permeation Chromatography

HEMTs .... High Electron Mobility Transistors

HTL .... Hole Transport Layer

HTM .... Hole Transport Material

IQE .... Internal Quantum Efficiency

MACl .... Methyl-Ammonium Chloride

MAI .... Methyl-Ammonium Iodide

$MAPbI_3$ .... Methyl-Ammonium Lead Iodide

$MAPbBr_3$ .... Methyl-Ammonium Lead Bromide

$MAPbCl_3$ .... Methyl-Ammonium Lead Chloride

MOSFET .... Metal-Oxide-Semiconductor Field-Effect Transistor

NWs .... Nanowires

P3HT .... Poly(3-hexylthiophee-2,5-diyl)

PB .... Photoinduced Bleach

PCE .... Power Conversion Efficiency

PEDOT:PSS .... Poly(3,4-ethylenedioxythiophene) Polystyrene Sulfonate

PIA .... Photoinduced Absorption

PL .... Photoluminescence

PMMA .... Polymethyl Methacrylate

PMTs .... Photomultiplier Tubes

PR .... Precipitation and Redissolution

PTAA .... Poly(triaryl amine)

PVK .... Perovskite

QDs .... Quantum Dots

QWIPs .... Quantum Well Infrared Photodetectors

RIE .... Reaction-Ion Etching

RC .... Resistance-Capacitance

RF .... Radio Frequency

SC .... Schottky Collector

SE .... Schottky Emitter

SEM .... Scanning Electron Microscope

SEPT ....Schottky-Emitter Bipolar Phototransistor

SF .... Stacking Fault

SLS.. Solution-Liquid-Solid

SPCM...Scanning Photocurrent Microscopy

TA .... Transient Absorption

TEM ....Transmission Electron Microscope

UV.. Ultraviolet

VBM ....Valence Band Maxima

VLS ....Vapor-Liquid-Solid

VRR ....Visible Rejection Ratio

XRD .... X-ray Diffraction

CHAPTER 1

INTRODUCTION TO CHARGE CARRIERS IN SEMICONDUCTOR MATERIALS

1.1. Semiconductors

Semiconductors are materials that have an electrical conductivity between that of conductors, such as metals, and insulators, such as glass. They possess a fundamental energy band gap based on their valence and conduction band potentials. Their optical and electronic properties can be flexibly modified by choice of material, dimensionality, application of electric or magnetic fields, heat, light, and doping levels, among other properties. Devices based on semiconductors can be used for amplification, switching, energy harvesting and energy conversion.

Semiconductors in their intrinsic state are poor conductors, as their valence bands are filled, preventing the flow of electrons. Typically, semiconductors are doped to create excess electrons (n-type) or a deficiency of electrons (p-type). The imbalance of electrons allows a current to travel through the material. By joining two differently doped semiconducting materials, one can create a semiconductor junction, resulting in transfer of electrons and holes across the interface until equilibrium is reached. By changing the electric potential or using a different semiconductor material, with a different band gap, equilibrium can be disturbed where ambipolar diffusion of electrons and holes can occur. By changing temperature or exposing the semiconductor to light, excess electrons and holes can be created by “generation” until electrons and holes return to equilibrium by “recombination.” Optoelectronic devices, such as solar cells and

photodetectors, rely on separating and transporting charge through semiconductors that have excess electron-hole pairs created by photon absorption.

1.2. Optoelectronic devices (solar cells and photodetectors)

Solar cells are electronic devices that convert light energy directly into electricity through the photovoltaic effect. Many solar cells rely on a built-in potential of a p-n junction. Photovoltaics work by absorbing light in a semiconductor (based on the semiconductor's band gap), separating the generated charge carriers across an electric field, and extracting of carriers to an external circuit to produce power. The efficiency of a solar cell depends on the absorptivity of the chosen semiconductor, the ability for charges to be separated, and the conductivity of the materials that the charges must move across. Typical efficiency losses are due to recombination losses and parasitic resistances known as series and shunt resistances. Series resistance depends on the resistance of charge carriers across the base of the solar cell, the contact resistance between the outer metal contacts and the absorbing material, and the resistance of the top and bottom metal contacts. Losses based on shunt resistance are normally due to manufacturing defects, as low shunt resistance allows an alternative current path that reduces the current flowing out through the circuit. Losses due to resistance are characterized in the solar cell by the fill factor of the device.

Photodetectors are very similar to solar cells, in that they are sensors of light energy based on p-n junctions that convert light photons into current. For solar cells, the main objective is to capture as many photons as possible, but for photodetectors the response time of the device is also important. Additionally, an externally supplied voltage may be used to increase the electric field beyond that arising at equilibrium in a semiconductor

junction. Photodetector performance is characterized by several figures of merit: spectral response, quantum efficiency, responsivity, noise-equivalent power, detectivity, gain, dark current, and response time.

1.3. Electronic transport in semiconductor materials

Electronic transport in semiconducting materials depends heavily on the mobility of charges throughout the material. When an electric field, E, is applied across a semiconductor, the electrons (or holes) move across the material with an average velocity called the drift velocity, v_d. Electron mobility, μ, is defined as the average drift velocity per electric field: $\mu = {}^{v_d}/_{E}$, given in cm^2/Vs. Mobility depends on impurity concentrations, defect concentrations, temperature, and electron and hole concentrations within the material, as well as applied electric field.

Electron mobility is typically inferred from Hall effect measurements or transistor behavior. The Hall effect states that the charge carriers in a current-carrying semiconductor under a magnetic field experience a force perpendicular to the magnetic field and the current. This pushes the charge to one side of the conductor. Charge buildup at the semiconductor edge results in a measurable voltage. The Hall mobility can then be calculated based on the sheet carrier density, n_s or p_s, and the sheet resistance, R_S: $\mu = 1/qn_sR_S$. Alternatively, mobility can be measured from field-effect transistors (FETs). FETs consist of three channels: source, drain, and gate. Carriers enter the channel through the source, leave the channel through the drain, and the gate modulates the channel conductivity. By changing the channel conductivity, σ, the carrier concentration, n or p, is modified and the mobility is measured through the transconductance, g_m: $\sigma = ne\mu$ and $g_m = \partial I_{DS}/dV_{GS} = \mu CWV_{DS}/L$ for a metal-oxide semiconductor FET (MOSFET)

configuration, where I_{DS} is the drain-source current, V_{GS} is the gate-source voltage, C is the capacitance of the dielectric layer, W is the channel width, L is the channel length, e is the elementary electron charge and V_{DS} is the drain-source voltage.

In addition to mobility, two important metrics to consider for optoelectronic devices are the diffusion length and the carrier lifetime. Diffusion length is the average distance that generated carriers can travel before they are lost to recombination. Mobility and diffusion are linked by the Einstein relation: $D = \mu k_B T / e$, where D is the diffusion constant, k_B is Boltzmann's constant, and T is the absolute temperature. Fick's first law of diffusion relates the diffusion coefficient as a proportionality constant of the diffusion current to their concentration gradient. By relating this law with the Einstein relation, a diffusion length, $L_D = \sqrt{D\tau}$, can be established where τ represents the carrier lifetime. Measuring either carrier lifetime or diffusion length is a good measure of the carrier dynamics of the system, as they can always be converted from one to another using this relationship. Long carrier lifetimes correspond to long diffusion lengths. The ability of charges to travel for long distances without recombination leads to the ability to make material thicknesses larger, allowing for greater absorption of photons in optoelectronic devices.

1.4. Scanning photocurrent microscopy

Scanning photocurrent microscopy (SPCM) is an experimental tool used to investigate optoelectronic properties of semiconductors. By raster-scanning a laser, a photocurrent is generated at each position of the device from which internal electric field, charge transport, and recombination dynamics can be evaluated.[1] This technique is similar to other scanning probe microscopy techniques, but unlike those techniques, SPCM can use a focused light beam or a probe tip to locally excite the material. Similar to a

photocurrent measurement, the laser beam excites a semiconductor, in this case locally, at which point the electrons and holes are free to relax, recombine, drift, and diffuse. If these carriers reach the electrodes before recombination, a photocurrent is measured.

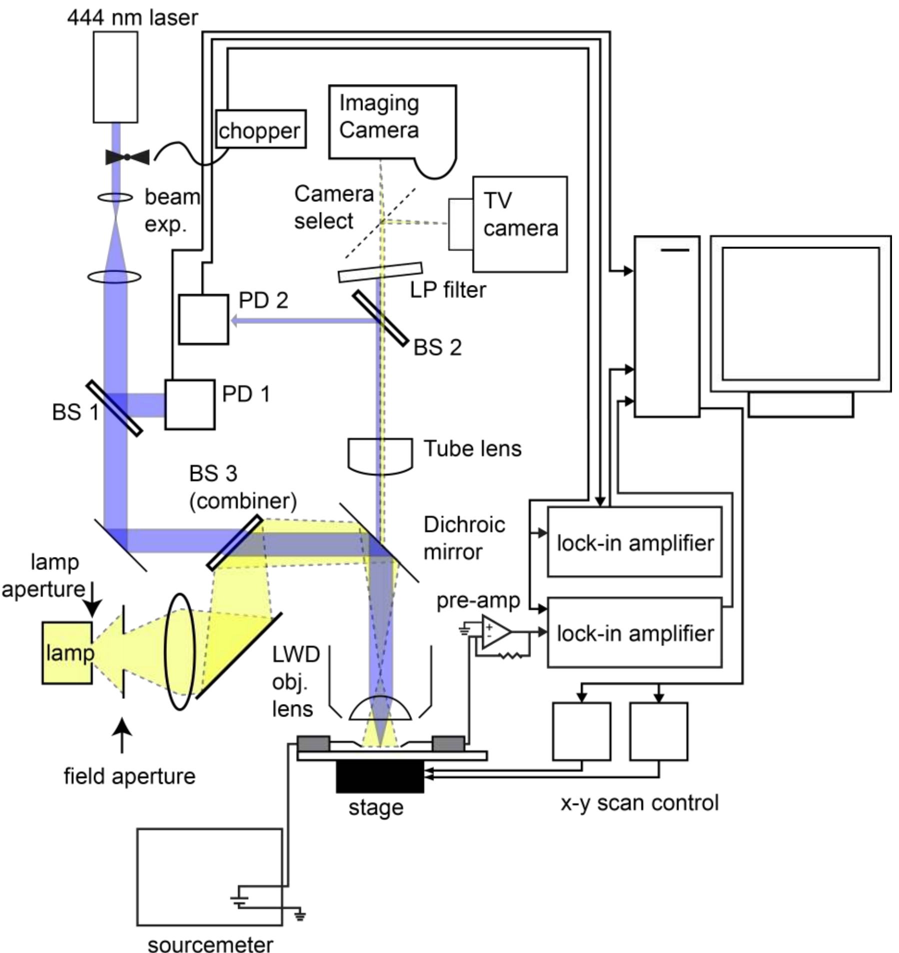

Figure 1.1. Diagram of a home-built scanning photocurrent microscope. The system utilizes a white light lamp for visual imaging and a 444 nm diode laser for the photocurrent microscopy. The system is equipped with two objective lenses − one 20x magnification with a numerical aperture of 0.42 and one 100x magnification with a numerical aperture of 0.70. Dual lock-in amplification is used to record the reflected and photocurrent signals simultaneously.

The current design for the SPCM system I have built is shown in **Figure 1.1**. A 444nm diode laser is used in conjunction with an x-y-z motion stage and a high numerical

aperture long working distance objective lens to create a diffraction-limited laser spot. A current pre-amplifier and lock-in amplifier are used to isolate the signal at the chopping frequency of the laser beam and improve the signal-to-noise ratio for measuring small currents. Using a dual lock-in amplifier setup allows for us to record a reflected signal optical micrograph alongside the photocurrent map. This allows us to couple the physical features of the device to its photocurrent signals. **Figure 1.2** (left) shows a reflected signal of a silicon photodiode, which has been covered with a mask of holes. **Figure 1.2** (right) shows the given photocurrent map for the same exact device area. A custom MATLAB script allows for analysis of a profile along the maps shown in **Figure 1.2**. The resulting profiles indicate a sharp rectangular rise in the photocurrent signal around the edges of the holes that corresponds to the drop at the same position in the reflected signal profile.

SPCM has been typically used to measure diffusion lengths in semiconducting materials, but also has applications in characterizing electronic field distribution, carrier lifetimes, doping density, and more.[1] This technique has been used to study semiconductor nanowires[2–6], carbon nanotubes[7–9], graphene[10–13], two-dimensional semiconductor materials[14], nanoporous layers of dye-sensitized solar cells[15,16], colloidal quantum dots[17,18], and perovskite absorbers[19,20]. In the simplest 1-D case, it has been shown that the electron current density of a material, J_e, is proportional to the gradient of excited carriers, Δn, leading to the following equation: $J_e = -eD_e\left({\partial \Delta n}/{\partial x}\right) \propto e^{-x/L_e}$ where D_e is the diffusion constant for electrons and L_e is the diffusion length for electrons.[1] This equation can also be equated for holes if they are the minority carrier instead of electrons. In the simplest case, by fitting the exponential decay away from the

peak photocurrent, one can solve the minority carrier diffusion length of the given material.

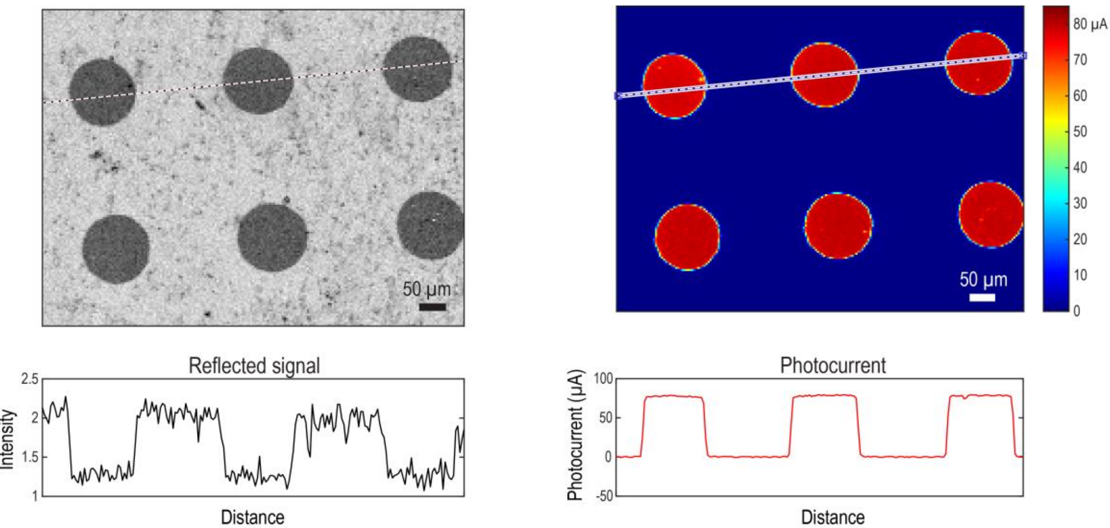

Figure 1.2. Top left and right show a reflected signal micrograph and a photocurrent map of a silicon photodetector masked by a repeated pattern of holes. When the light passes through the holes, a large photocurrent signal is observed as seen by the red colored circles. Below each map is a linear profile of the drawn dotted line on each map.

1.5. Emerging material systems and reduced dimensionality

For optoelectronic devices, choice of material is extremely important. For both solar cells and photodetectors, crystalline silicon is the most prevalent bulk material used. Typical silicon photodiodes have a spectral range of up to 200-1100 nm and single crystal non-concentrator silicon solar cells have reached an excess of 25% solar conversion efficiency.[21] While silicon technology is well studied and understood, many problems alongside intrinsic limitations still exist. Precise control of crystalline silicon seed growth is required, as well as control of oxygen defects and dopants on the surface. Additionally, silicon is an indirect bandgap material (requiring larger absorption cross sections), leading to a lower absorption coefficient and requiring a greater thickness to achieve the same absorbance compared to direct band gap materials. These fabrication processes

increase the cost for production of silicon. The search for emerging materials that may be able to deliver efficiencies close to that of silicon at lower cost have been researched for the last several decades.

Some emerging materials, such as semiconductor nanowires and quantum dots, rely on their interesting properties arising from their reduced dimensionality. In bulk semiconductors electronic states are delocalized in the material and the filled and empty electronic states are separated by an energy bandgap. The continuous electronic states result in band-like structure where the conduction band defines the electronic states and the valence band defines the hole states. In bulk semiconductors, electrons remain unconfined and experience the periodic electric potential of the crystal lattice. The bandgap of the materials determines not only what wavelengths the material can absorb, but also determines the wavelength of photons emitted by radiative recombination of electrons and holes. In bulk materials, these properties are independent of size. When the size of one or all dimensions of a semiconducting material are reduced to a length scale similar to the Bohr radius for electron-hole pairs, the material changes from the three-dimensional (3-D) bulk to 2-D quantum wells, to 1-D quantum wires, to 0-D quantum dots. Consequently, the density of electronic and hole states changes measurably from continuous states to discrete states (0-D) or sub-bands (1-D, 2-D) governed by quantum mechanical solutions to the confined potential. In this regime, the semiconductor demonstrates size-dependent properties, such as bandgap tunability. This leads to unique advantages in emerging materials with lowered dimensionality, such as quantum dots or quantum nanowires. In the following paragraphs, four emerging material systems will be

discussed that will be investigated in the following chapters: lead-halide perovskites, epitaxial graphene on SiC, semiconductor nanowires, and quantum dots.

1.5.1 Perovskites

In the last few years, tremendous growth has been achieved in the research of lead halide perovskite solar cells. Efficiencies of greater than 20% have been achieved.[21] These materials have garnered high interest because of their unique electronic properties, composition of abundant elements, and their ease of processing methods. Perovskite absorbers also offer flexibility as they possess direct bandgaps that can be tuned by adjusting their inorganic and organic components.

Perovskites are defined as any materials that adopt the same structure as calcium titanate, $CaTiO_3$, with a general formula of ABX_3. Traditionally, perovskite materials are fabricated by solid-state synthesis at high temperatures.[22] However, hybrid organic/inorganic lead halide perovskite solar cells can be fabricated at low temperatures by simple solution processable methods, which make them of interest for low cost solar cells. Three main compositions of lead halide perovskite materials have been studied for use in solar cells, namely methyl-ammonium lead iodide $CH_3NH_3PbI_3$ ($MAPbI_3$), methyl-ammonium lead bromide $CH_3NH_3PbBr_3$ ($MAPbBr_3$), and a mixed halide of methyl-ammonium lead iodide/chloride $CH_3NH_3PbI_{3-x}Cl_x$ ($MAPbI_{3-x}Cl_x$). However, much work has begun on more sophisticated perovskite structures employing cesium (in place of the organic cation), tin (in place of lead), and other materials.[23] Halide perovskite materials are usually either deposited on mesoporous scaffolds, such a TiO_2, or employed as a thin film in a planar heterojunction. In either configuration, the perovskite is paired with electron and hole transport layers to extract the generated carriers in the perovskite layer.

An organic molecular layer of spiro-OMeTAD began as the hole transport material (HTM) of choice, but researchers are beginning to search for higher mobility materials. Spiro-OMe-TAD only shows a hole mobility of around 10^{-4} $cm^2/V/s$, which can be increased by doping.[24] To achieve the highest fill factors, high-mobility transport layers are needed. Other organic materials such as poly (triaryl amine) (PTAA) and poly(3,4-ethylenedioxythiophene) polystyrene sulfonate (PEDOT:PSS) have been studied, however most organic transport layers result in less stable perovskite devices, which naturally decompose over a few days. In an attempt to move past spiro-OMe-TAD, some research has shifted towards inorganic HTMs. Subbiah et al. employed NiO and CuSCN as hole collectors in planar mixed halide perovskite solar cells.[25] Solar cells using NiO demonstrated a 7.3% efficiency with an open-circuit voltage similar to cells using spiro-OMe-TAD. NiO-based solar cells have also demonstrated much greater stability, showing stable performance for 60 days.[26] Investigation of the stability and performance of perovskite solar cells using different HTMs is of utmost importance to commercialize perovskite solar cells.

1.5.2 Epitaxial graphene on silicon carbide (SiC)

Graphene is one of the fastest developing material during the last several years. Graphene is a sheet of sp^2 bonded carbon atoms arranged in a honeycomb lattice. Carriers in graphene possess up to ~10x higher mobilities than conventional semiconductors.[27] High mobility, current density, optical transparency (~2.3% absorption per layer) and thermal conductivity have made it an appealing material for emerging electronic technologies.[28]

Most of the aforementioned properties are related to pristine graphene in idealized conditions, however, graphene is typically used in more complex structure and at specific conditions targeted at specific applications. Several techniques have been developed to produce high quality graphene for electronics. Micromechanical exfoliation of graphene is the most common growth method to produce quality graphene for condensed matter physics experiments.[28] However, this process is time consuming and the resultant graphene cannot be well controlled on a large scale, making this method unsuitable for industrial scale. Chemical vapor deposition (CVD) growth of graphene on transition metals has led to high quality graphene that may be produced on a large scale. With this method, the as-grown graphene must be transferred to an appropriate substrate. This transfer process commonly causes dislocations, grain boundaries, and other substrate issues that lower the quality of the graphene layer.

To avoid the problems from micromechanical exfoliation and CVD-growth on transition metals, one approach has been to grow graphene by thermal decomposition of SiC.[29] This method allows for graphene to be directly obtained on a commercially available substrate, which allows for scalable graphene growth without the need for transfer. Due to the vapor pressure of carbon being negligible compared to the vapor pressure of silicon, silicon can be evaporated from the surface to allow carbon atoms to rearrange to form graphene at high temperature.[29] Epitaxial graphene (EG) based SiC devices have been used as FETs, radio frequency (RF) transistors, integrated circuits, and as sensors.[27]

1.5.3 Semiconductor nanowires

Semiconductor nanowires are quasi one-dimensional nanostructures fabricated with control of diameter, length, composition, and crystalline phase. Typically, these materials have diameters ranging from few nanometers to hundreds of nanometers and length of microns to millimeters. Their specific geometry and unique properties separate these materials from their bulk counterparts and has led to nanowires being used in many fields: nanosensors, photonics, lasers, thermoelectrics, photovoltaics, artificial photosynthesis, lithium-ion batteries, and more.[30] Nanowires with diameters on the scale of the Bohr radius or shorter can exhibit quantum confinement, which allows for tuning of the optical bandgap by the given NW size. Among various semiconductors, nanowires of binary groups III-V and II-VI compounds, such as ZnS[31], InAs[32], GaAs[32], CdS[31], and GaN[33] have been studied, along with single elements of group IV, such as Si[34] and Ge[34]. Wide band gap II-VI semiconductors, such as CdSe and CdS, have been studied widely due to their potential in photodetector applications. Their visible absorption and potential for high quantum efficiency compared to silicon-based devices, which have a quantum efficiency of around 10%, demonstrates their potential for innovation.[35]

Nanowires possess potential for photovoltaic applications due to their tunable geometric effects, high carrier mobility compared to thin films, and inexpensive processing at a relatively low temperature. One key geometric advantage is the ability to separate absorption and charge separation length scales. For example, the ability to absorb light along the nanowire axis and separate charges radially, which removes the competing length scales of absorption depth and diffusion length found in traditional

planar cells.[36] Other advantages include decreased net reflectance, increased junction area, and reduced material use.[37]

1.5.4 Quantum dots

Quantum Dots (QDs) are zero-dimensional crystalline semiconductor nanoparticles typically with inorganic composition of groups II-VI, III-V, and IV-VI.[38] Due to their confined electronic states in all three dimensions, they exhibit tunable optical and electronic properties. By changing the QD size, shape, composition, or structure, the wavelength of absorption and emission can be tuned, along with the mobility and charge carrier dynamics.[39] Due to these unique properties, they have been used in biomedical imaging, light-emitting devices, photodetectors, and solar cells.[40] Properties of QD solid films are additionally sensitive to their spacing and organization within the solid. As the interparticle distance between QDs decreases, the interaction of wavefunctions of the QDs increases, possibly leading to long range QD superlattices.

QDs are typically grown with insulating, long-chain alkyl stabilizing ligands to retain the size, surface, and colloidal stability of the QD. These are unfavorable for electronic applications, so post-synthetic treatments, such as ligand exchange of QDs, are necessary for efficient optoelectronic devices. Chemical methods have been used to exchange ligands for various types of shorter or conjugated organic molecules and inorganic ligands. Generally, as the ligand chain length decreases, the mobility of the QD film increases.[41]

Great advances in recent QD devices have shown an increase to mobilities of $\geq$10 cm^2 V^{-1} s^{-1}.[38] This increase has greatly depended on the evolution of charge transport in QDs from “hopping” like behavior between localized states, to band-like transport throughout

the extended QD film. In QD solid films, large inhomogeneities in QD size and shape, disordered packing, incomplete ligand exchanges, and trap sites caused by unpassivated atoms on the surface continue to lower the mobility of QD films. QD film mobilities still lag behind traditional semiconductors and other nanostructures, such as semiconductor nanowires, and QD solar cell efficiency remains below 15%. To take advantage of their unique properties, solution-based processing, and ability to be printed on flexible substrates, much research remains to be done in the QD electronics field.

1.6. Dissertation overview

In this thesis, the studies are focused on measuring critical length scales, figures of merit, conductive pathways, and carrier dynamics of several optoelectronic devices. By creating working mechanisms of how charges move and interact in devices, optoelectronic devices can be more readily developed with an idea of how to interface given semiconductors and improve performance. The last three chapters will employ the home-built SPCM system described in Chapter 1 to study carrier dynamics.

The first study in Chapter 2 is focused on studying the diffusion and mobility of charges across perovskite solar cells. Transient transmission spectroscopy is used to study the dynamics of generated carriers near and far away from the HTM/perovskite interface in a planar perovskite solar cell. This technique, in addition to several others, allows for an estimation of the diffusion constant of the perovskite and compares the differing results between three HTMs with respect to actual device performance.

Chapter 3 focuses on studying a Schottky-emitter bipolar phototransistor (SEPT) based on an epitaxial graphene (EG) emitter grown on a p-SiC base epilayer. Devices created with this architecture have exhibited large current gains and high UV responsivity. The

high performance and relatively novel operational principles of this device make it critically important to analyze the visible response of the device. Employing scanning photocurrent microscopy (SPCM) with sub-bandgap light as well as a variety of other techniques, the device was investigated to determine the possible sources of visible absorption.

Chapter 4 continues the study on SEPT devices. In this chapter, a new SETP device is created with a thinner base epilayer and a new graphene grown method using SiF_4. This device showed better performance than the device created in Chapter 3. SPCM is once again used not only to classify sub-bandgap absorption, but also UV absorption. By mapping the photocurrent in different modes using different excitation wavelengths, a working model of charge generation and carrier dynamics in the device is proposed.

Chapter 5 focuses on photocurrent studies of low-dimensional semiconductors – namely semiconductor nanowires and colloidal quantum dots. By establishing a measurement system and device fabrication routine for these materials in our lab, it opens many possible research directions for optoelectronic devices employing these materials. SPCM is also used to clarify photocurrent generation and to demonstrate the ability of our microscope to resolve small nanostructures.

CHAPTER 2

DIRECT OBSERVATION OF ULTRAFAST HOLE INJECTION FROM LEAD HALIDE PEROVSKITE BY DIFFERENTIAL TRANSIENT TRANSMISSION SPECTROSCOPY[1]

2.1. Preface

In August 2013, I received a National Science Foundation Integrative Graduate Education and Research Traineeship (NSF IGERT) grant. This grant supported two years of research and an overseas internship experience. The IGERT program aimed to bring together different scientific departments within the university to promote interdisciplinary collaborative research. Through this research program, students were to develop teamwork skills and diversify their education towards contribution to solving complex research problems of significant scientific and societal importance at the national and international level. One such problem is the energy crisis and the development of cleaner and sustainable energy.

As I mentioned previously, one component of the IGERT program is a 3 to 6-month international internship. Several opportunities were presented to us from different universities and institutes across Asia. While many of my fellow students chose to study catalysis, I opted to study perovskite solar cells at the National Institute for Materials Science (NIMS) in Japan under Dr. Kenjiro Miyano. I was drawn to this topic due to developing interest in solar energy production from my previous experiences in the

[1] Reprinted with permission from Ishioka, K.; Barker, B. G.; Yanagida, M.; Shirai, Y.; Miyano, K. Direct Observation of Ultrafast Hole Injection from Lead Halide Perovskite by Differential Transient Transmission Spectroscopy. *J. Phys. Chem. Lett.* **2017**, *8* (16), 3902–3907. Copyright 2017 American Chemical Society.

IGERT program, as well as my own personal interests in the quickly emerging research based on perovskite solar cells.

While at NIMS, I made several solar cells featuring various hole transport materials and tested them with techniques such as current-voltage curves to measure power conversion efficiency (PCE), external quantum efficiency (EQE), transmission spectroscopy, photoluminescence (PL), time-resolved PL, x-ray diffraction (XRD), scanning electron microscopy (SEM), and infrared spectroscopy. I also led a project looking at carrier dynamics using transient absorption (TA) while probing in the infrared region. While progress on this project was slow, I met with Dr. Kunie Ishioka to measure the same samples I fabricated using her TA system probing in the visible region. This led to a fruitful collaboration, in which my previous data from the techniques mentioned above were combined with her expertise in transient transmission to produce a collaborative research journal article. In this article, I prepared the samples, measured the samples using the previously listed techniques, and then forwarded them to Dr. Ishioka to measure. Upon collection of the data, I routinely met with her to discuss the resulting analysis of the data and this analysis was compiled into a complete journal article described in this chapter.

2.2. Introduction

Lead halide perovskite photovoltaic cells have been developing rapidly in the past few years, with their power conversion efficiency (PCE) now exceeding 22%.[21] Perovskites are direct semiconductors, and their photovoltaics can in principle work as a model p–i–n diode.[42] The difficulty in the controlled impurity doping in perovskites can be circumvented by sandwiching the perovskite film between thin layers of electron- and

hole-transporting materials (ETM and HTM) in a planar heterojunction structure.[43] These carrier transporting layers enable efficient and irreversible separation of the electrons and holes photoexcited in the perovskite and thereby lead to the high PCE of the perovskite solar cells. Whereas various inorganic and organic materials have been explored as ETMs and HTMs, based on their conduction and valence band energy offsets with respect to those of the perovskite, the actual device performance shows only a weak correlation with the energy levels.[43,44]

Time-resolved photoluminescence (PL) and transient absorption (TA) spectroscopies have been employed extensively to investigate the microscopic effects of the ETM and HTM layers on the carrier dynamics in the perovskites. The previous PL studies monitored the injections of the photoexcited carriers into the transport layers indirectly as the suppression of the PL intensity emitted at their recombination and the acceleration in the PL decay time on a tens of nanosecond time scale.[45–49] Excitation density dependences of the PL decay time and of the solar cell external quantum efficiency (EQE) revealed a carrier-injection bottleneck at the interfaces with TiO_2 and spiro-OMeTAD at high excitation densities.[50] The extraordinarily long electron and hole diffusion lengths in the perovskites were confirmed by the PL and TA measurements in the visible and THz ranges on perovskites with and without the ETM and HTM.[51–54] The time scale of the charge injection from the perovskite to the HTM layer itself remains controversial, however, despite the extensive TA studies that aimed to directly time-resolve the injection dynamics.[51,55–63] The time constant of the hole injection from $CH_3NH_3PbI_3$ ($MAPbI_3$) to spiro-OMeTAD in the previous reports, for example, scattered widely from <80 fs[55] to 0.7 ps[56,57] to 8 ps.[58] The hole injection to NiO_x was reported to be

complete on the sub-picosecond time scale,[59] whereas those to poly(triarylamine) (PTAA), poly(3-hexylthiophee-2,5-diyl) (P3HT), and poly[2,6-(4,4-bis(2-ethylhexyl)-4H-cyclopenta[2,1-*b*;3,4-*b′*]dithiophene)-*alt*-4,7-(2,1,3-benzothiadiazole)] (PCPDTBT) were reported to occur on sub-nanosecond time scales.[60] The apparent inconsistency among the different studies can be contributed by the different sample crystalline and interfacial qualities as well as the difficulty in separating hole injection from other carrier dynamics observed in the spectroscopic signals.

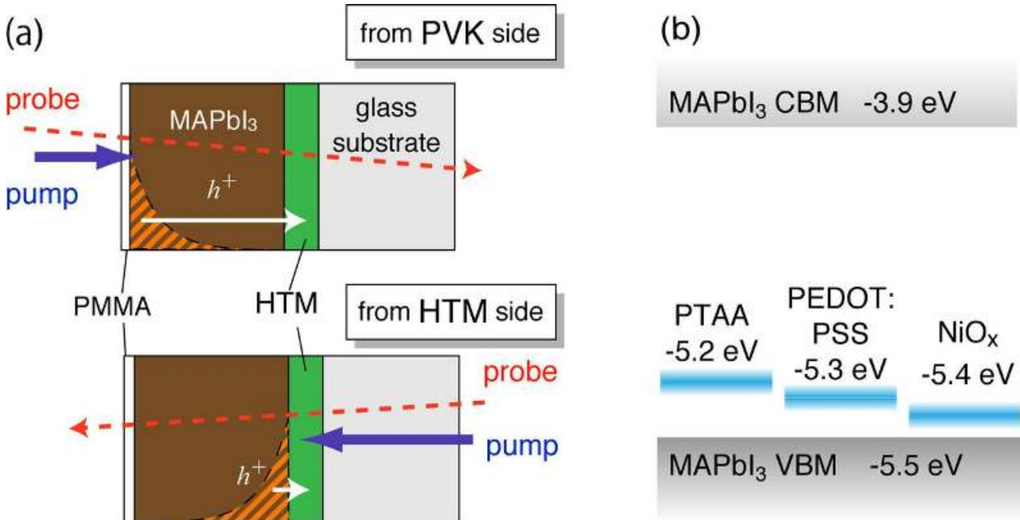

Figure 2.1. (a) Schematics of the two different configurations of the pump–probe transmission measurements of the $MAPbI_3$/HTM sample. The photoexcited region inside of the $MAPbI_3$ film is designated by the hatched area. (b) Energy levels of the valence band maxima (VBM) of the HTMs in comparison with the VBM and the conduction band minimum (CBM) of $MAPbI_3$. Copyright 2017 American Chemical Society.

In this work, we propose a differential transient transmission method to extract the carrier injection dynamics near the interface of the perovskite and the carrier transport layer. We measure transient transmission from both sides of the perovskite sample, the HTM side and the back (PVK) side, as shown schematically in **Figure 2.1a**, and take the difference between the two signals. By using excitation light whose optical absorption length is considerably shorter than the perovskite film thickness, we can exclusively

monitor the carrier dynamics at the interface with the HTM. We systematically apply this method to the interface of $MAPbI_3$ with three organic and inorganic HTMs typically used in the planar solar cells, PTAA, poly(3,4-ethylenedioxythiophene):poly(styrenesulfonate) (PEDOT:PSS) and NiO_x, whose valence band maxima (VBM) lie at slightly different energies (**Figure 2.1b**).

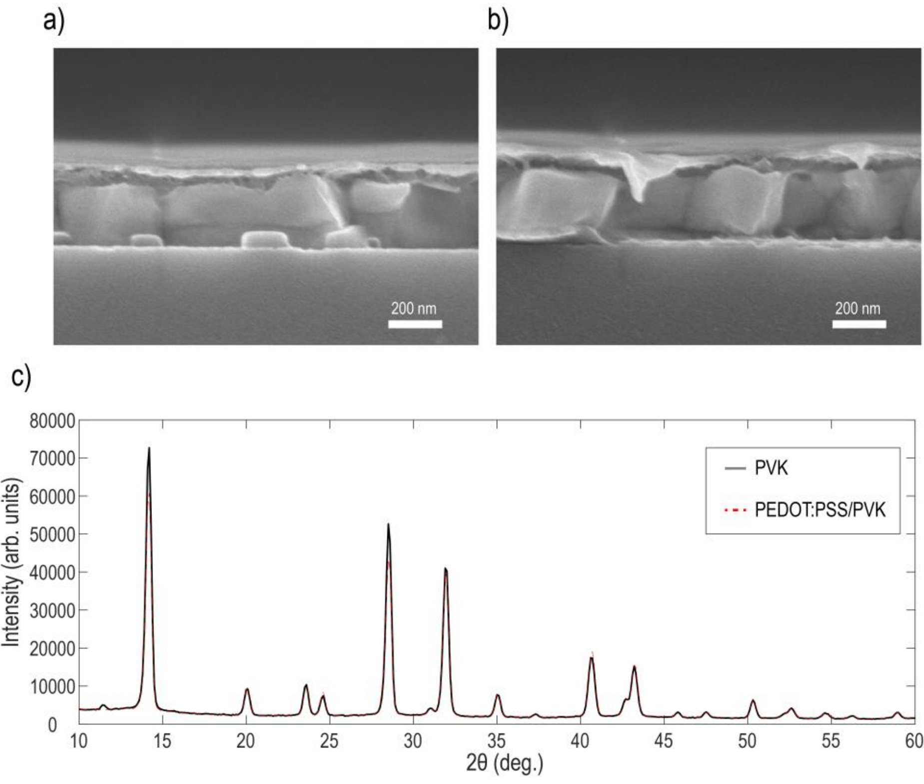

Figure 2.2. (a,b) Scanning electron microscope image of a $MAPbI_3$ film on a glass substrate and on a PEDOT:PSS film on a glass substrate, respectively. (c) X-ray diffraction pattern of the films in (a,b) showing a near identical tetragonal pattern.

2.3. Scanning electron microscopy and X-ray diffraction of $MAPbI_3$ films

Samples for spectroscopic measurements consist of a glass substrate, a thin layer of HTM (either PTAA, PEDOT:PSS, or NiO_x),[64,65] a 250 nm thick crystalline $MAPbI_3$ film,[66,67] and a poly(methyl methacrylate) (PMMA) capping layer, as schematically shown in **Figure 2.1a**. For comparison, we also prepare a sample without

the HTM layer. $MAPbI_3$ films are prepared using chlorine-mediated interdiffusion, which has been shown to produce higher quality films.[66,67] A cross-sectional scanning electron microscope image of a $MAPbI_3$ film grown on a glass substrate is shown in **Figure 2.2a**, alongside a $MAPbI_3$ film grown on PEDOT:PSS deposited onto a glass substrate is shown in **Figure 2.2b**. Both samples are capped with PMMA for protection from the atmosphere. Perovskite samples appear to be of similar quality with large crystal domains of continuous $MAPbI_3$ film. Further characterization of the films by X-ray diffraction (XRD) of these two samples show nearly identical diffraction patterns, corresponding to a tetragonal perovskite structure (**Figure 2.2c**).[68] Further work on NiO_x samples is required, although they have been shown to create quality perovskite films using similar preparation methods.[64,65]

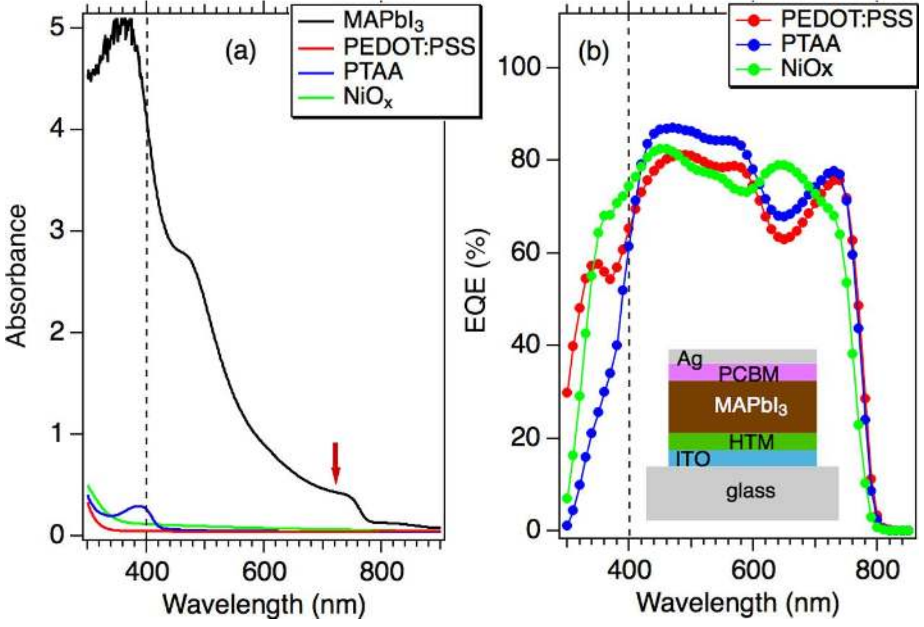

Figure 2.3. (a) Absorption spectra of the $MAPbI_3$ film without HTM and of the HTM layers only. The broken line and arrow indicate the wavelengths of the pump and probe lights. (b) EQEs for the solar cells with three different HTMs. The inset in (b) schematically illustrates the solar cell structure. Copyright 2017 American Chemical Society.

2.4. Absorption characteristics of $MAPbI_3$ films

Transient transmission measurements are performed using 400 nm pump and 720 nm probe light pulses with 150 fs durations. The pump light has an absorption length considerably shorter than the perovskite film thickness (α^{-1} = 42 nm[69]) and thus provides inhomogeneous photoexcitation only near the HTM interface or near the back surface, as shown in **Figure 2.1a**. The probe light has an absorption length exceeding the film thickness (α^{-1} = 820 nm[69]) and monitors the carrier dynamics up to ∼0.1 eV above the band edge of $MAPbI_3$ over the whole film thickness. The $MAPbI_3$ film has broad absorption in the visible range, whereas the absorption of the pump and probe lights by the HTM layer is negligible except for the small absorption by PTAA at 400 nm, as shown in **Figure 2.3a**.

2.5. Emission spectra and fluorescence decay lifetime of $MAPbI_3$ films

Figure 2.4a shows the emission spectrum recorded for several $MAPbI_3$ films deposited on glass substrates with and without HTMs. For nearly every sample, a broad emission peak appears around 760 nm. In the presence of a HTM, the emission intensity decreases; this is due to photogenerated holes being transferred into the HTM, resulting in less holes available to recombine and emit. The fluorescent lifetime decay of several samples, including those with and without the chlorine-interdiffusion treatments mentioned earlier,[66,67] are shown in **Figure 2.4b**. The presence of MACl promotes an increase in the lifetime of the perovskite-only sample from 349 to 408 ns. Upon the addition of HTMs PEDOT:PSS and PTAA, the average lifetime decreases to 30 ns and 2.4 ns, respectively, indicating quenching of photogenerated holes. The large difference in the lifetime of the sample using PEDOT:PSS and PTAA may indicate more efficient hole scavenging in

samples employing PTAA as a HTM in comparison to samples using PEDOT:PSS. Investigation of samples involving NiO_x are still needed; however, a reduction of the average lifetime of a perovskite sample has been shown to decrease from 145 ns to 70 ns in the presence of NiO_x.[26]

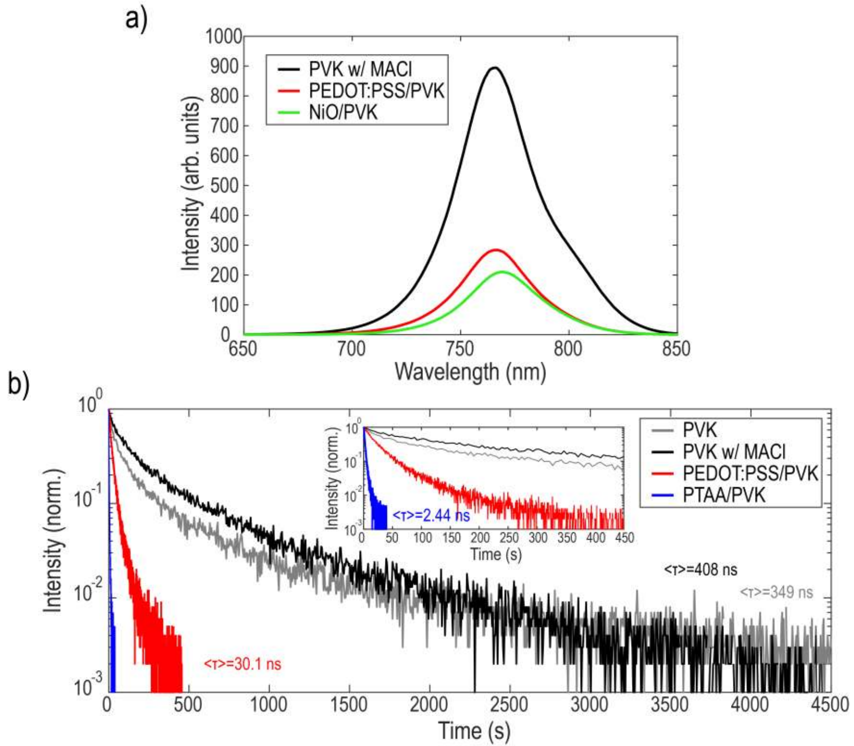

Figure 2.4. (a) Emission spectrum of $MAPbI_3$ films deposited on glass substrates with and without HTMs. (b) Fluorescence lifetime decays of $MAPbI_3$ films with and without MACl treatment deposited on HTMs. Inset shows lifetime decay <500 ns. (c) The average lifetime, <*t*>, of the films shown in (b).

2.6. Change in transient transmission of $MAPbI_3$ films measured from the near and far side of the HTM/PVK interface

Figure 2.5 compares the transient transmission changes $\Delta T_{PVK}/T$ and $\Delta T_{HTM}/T$ measured from the PVK and HTM sides of the samples. The transient signals of the perovskite without HTM show no systematic difference between the two

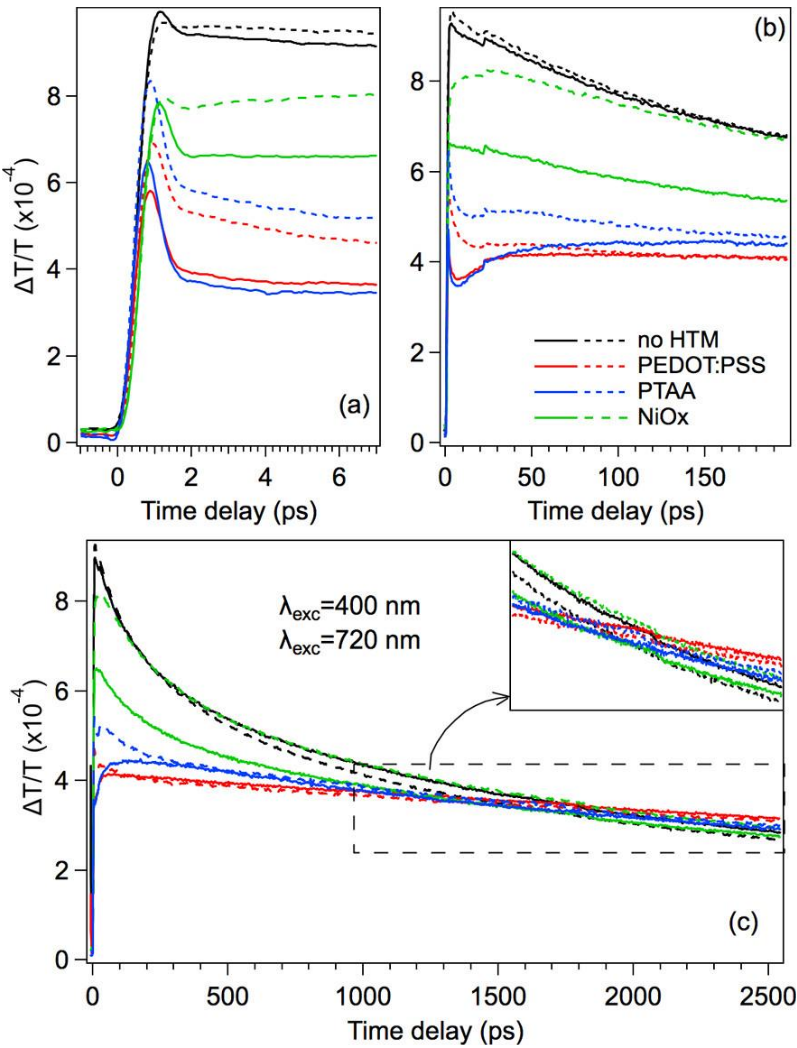

Figure 2.5. Transient transmission changes of $MAPbI_3$ with different HTMs and without, pumped at 400 nm and probed at 720 nm on picosecond (a), sub-nanosecond (b), and nanosecond (c) time scales. Solid and broken curves denote the transient transmission photoexcited on the HTM and PVK sides, $\Delta T_{\mathrm{HTM}}/T$ and $\Delta T_{\mathrm{PVK}}/T$, as illustrated in **Figure 2.1a**. The pump density is 0.5 μJ/cm^2. Copyright 2017 American Chemical Society.

configurations; they both rise instantaneously (<~1 ps) after photoexcitation and then decrease biexponentially, with time constants of τ_1 = 0.16 and τ_2 = 1.6 ns at a pump density of 0.5 μJ/cm^2. Previous studies reported that either the short-wavelength tail of the photoinduced bleach (PB) of probe light[55,70–72] or the long-wavelength tail of the photoinduced absorption (PIA) by photoexcited carriers[62,73] can be dominant at 720 nm in the TA of $MAPbI_3$, depending on the experimental conditions such as the perovskite

crystalline quality, film thickness, aging history, the presence of the HTM and ETM layers, and the interfacial qualities, as well as the wavelength and density of the excitation. In the present study, the transient transmission change appears always positive ($\Delta T > 0$), indicating that the PB dominates.

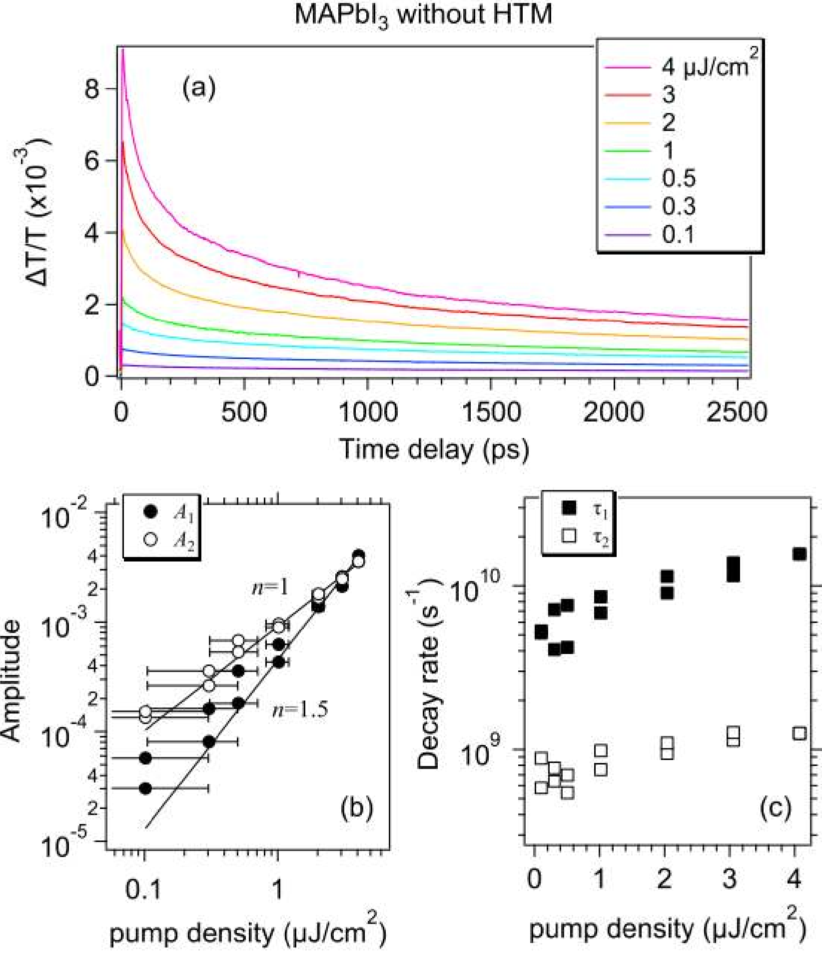

Figure 2.6. (a) Transient transmission changes of $MAPbI_3$ without HTM pumped at 400 nm with a range of pump densities. (b,c) The amplitudes A_1, A_2 and decay rates τ_1^{-1}, τ_2^{-1}, obtained from fitting of the transient transmission traces to a biexponential decay, as a function of the pump density P. Solid lines in (b) represent fitting to a power function $A(P) = A_0P_n$, with $n = 1.5$ and 1 for A_1 and A_2.

The transient transmission of the $MAPbI_3$ without HTM shows no systematic difference when measured from the two sides of the sample. The obtained transmission signals, shown for different pump densities in **Figure 2.6a**, rises instantaneously (≤1 ps) after photoexcitation, followed by a monotonic decrease that can be fitted to a biexponential decay: $f(t) = A_1 e^{-t/\tau_1} + A_2 e^{-t/\tau_2} + C$. With increasing pump density, the amplitude A_1 of the fast-decaying component grows superlinearly, whereas that of the slow-decaying one, A_2, grows linearly, as shown in **Figure 2.6b**. The decay rates τ_1^{-1} and τ_2^{-1} increases monotonically with the pump density, as shown in **Figure 2.6c**. Above pump density of 4 μJ/cm^2 the transmission signal undergoes irreversible change during the time delay scan. Based on the observed pump density-dependences we attribute the fast- and slow-decaying components to the Auger (trimolecular) and non-geminate (bimolecular) recombinations.[54,74] The observed carrier dynamics are consistent with a previous report on a 60 nm thick $MAPbI_3$ film pumped and probed at the same wavelengths.[71]

By contrast, the $\Delta T_{HTM}/T$ (dotted lines) signals of the perovskite films with HTMs are systematically smaller than the $\Delta T_{PVK}/T$ signals (solid lines) of the same sample at early time delays shown in **Figure 2.5a** and **Figure 2.5b**. This can be interpreted as the smaller hole population at the $MAPbI_3$/HTM interface than that at the $MAPbI_3$/PMMA interface. After undergoing complicated decays and rises on picosecond time scales, the signals measured from the two sides eventually converge on sub-nanosecond time scales, as shown in **Figure 2.5b** and **Figure 2.5c**, confirming that both sides of the perovskite films are excited at the same pump density. On the even longer time scale, the signals from both sides decay biexponentially (**Figure 2.5c**), like we have already seen for the

perovskite without HTM. The presence of the HTM layer reduces the amplitude of the faster component. In the case of $MAPbI_3$ with PEDOT:PSS and PTAA, the decay time of the slower component becomes longer (τ_2 = 5.2 and 3.0 ns, respectively), indicating that the electrons photoexcited in the perovskite film survive longer as a result of the deprivation of holes.

2.7. Differential transient transmission of $MAPbI_3$ films paired with HTMs

The time evolutions of the transient transmission signals of the samples with HTM on picosecond time scales appear to be common to $\Delta T_{HTM}/T$ and $\Delta T_{PVK}/T$ and therefore not specific to the HTM interface. Moreover, $\Delta T_{PVK}/T$ for the samples with HTM is systematically smaller than that without HTM at the early time delays shown in **Figure 2.5a** and **Figure 2.5b**. This is not because of the absorption of the probe light by the HTM layer, since $\Delta T/T$ is the pump-induced fractional change. These results instead suggest that the presence of the HTM may cause other effects than the interfacial hole injection, such as PIA by the HTM layer and modification of the transport and recombination dynamics within the whole perovskite film. To extract the carrier dynamics directly related with the $MAPbI_3$/HTM interface and cancel out other effects, we hereafter focus on the differential transient transmission $\Delta T_{diff}/T \equiv (\Delta T_{PVK} - \Delta T_{HTM})/T$ plotted in **Figure 2.7**. This quantity can be regarded to be proportional to the difference in the hole populations photoexcited in the perovskite in the two configurations, $N_{diff}(t)$, if we neglect the small tail of the absorption bands of the oxidized species or polarons that have peaks at ~1000 and ~500 nm for PEDOT:PSS and PTAA.[75,76] We see that $\Delta T_{diff}/T$ is very small for the perovskite without HTM, which guarantees the quantitative reproducibility of our measurements.

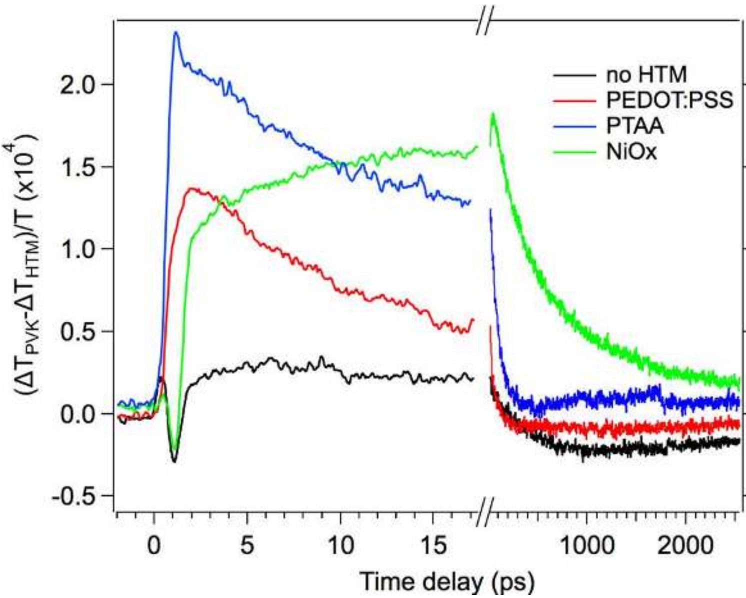

Figure 2.7. Differential transient transmission $\Delta T_{diff}/T = (\Delta T_{PVK} - \Delta T_{HTM})/T$ of $MAPbI_3$ with different HTMs and without. Copyright 2017 American Chemical Society.

In the presence of the HTMs, $\Delta T_{diff}/T$ rises and then decays to nearly zero on different time scales for different HTMs. The rise implies the disappearance of holes at the $MAPbI_3$/HTM interface due to the injection to the HTM layer (and other interfacial processes, if any). The decay can be interpreted as a result of the hole diffusion in the perovskite film, making the hole distribution more homogeneous. $\Delta T_{diff}/T$ for $MAPbI_3$/PTAA rises rapidly after photoexcitation and reaches a maximum at $t = 1$ ps, providing direct evidence for the hole injection to be complete on the sub-picosecond time scale. The hole injection time observed here is comparable to those in the previous report on the sub-picosecond injection at $MAPbI_3$/spiro-OMeTAD[55,56] but orders-of-magnitude faster than that reported for the $MAPbI_3$/PTAA.[60] The differential signal for $MAPbI_3$/PEDOT:PSS exhibits similar behavior, except that the maximum is reached at a slightly later time ($t = 2$ ps). For $MAPbI_3/NiO_x$, by contrast, $\Delta T_{diff}/T$ exhibits a distinct two-step rise, whose first step is almost as fast as those for PTAA and PEDOT:PSS, but

the second step is considerably slower, reaching a maximum at $t = 44$ ps. The observation can be interpreted in terms of two injection paths to NiO_x with different rates, for example, direct injection and injection via interfacial defect levels, or injections of holes with different excess energies. Either fast or slow step can, in principle, be contributed to by other interfacial processes as well, such as recombination, trapping by interfacial defects, and energy transfer from the HTM.

2.8. Modeling the hole diffusion in perovskites to compare with the differential transient transmission results

We perform numerical simulations on the hole diffusion in the perovskite to understand the decay of the $\Delta T_{diff}/T$ signals quantitatively. The previous studies reported different values of the diffusion constant D, ranging from 0.01 to 4 cm^2/s, for different $MAPbI_3$ crystalline qualities.[51,58,77–79] We therefore calculate the depth- and time-dependent hole distributions $N_{PVK}(z, t)$ and $N_{HTM}(z, t)$ for excitation on the PVK and HTM sides, as shown in **Figure 2.8a**, **Figure 2.9,** and **Figure 2.10**, using different values of D. We then obtain the differential hole population $N_{diff}(t) = N_{PVK}{}^{S}(t) - N_{HTM}{}^{S}(t)$, as plotted in **Figure 2.8b**, where $N_i^S(t) = \int_0^d N_{PVK}(z,t)dz$ with i = PVK or HTM is the depth-integrated hole population. We find that $N_{diff}(t)$ decays on 100 ps and 1 ns time scales when calculated with $D = 4$ and 0.4 cm^2/s. The former decay time is in rough agreement with the experimental $\Delta T_{diff}/T$ signals for $MAPbI_3$ with PTAA and PEDOT:PSS, whereas the latter is with that with NiO_x. The relatively large D confirms the good crystalline quality of the perovskite films fabricated on top of the PTAA and PEDOT:PSS layers, whereas the smaller D suggests poorer quality for that on NiO_x. If we take 4 cm^2/s as a good estimate of the diffusion constant of the perovskite and the

lifetime as ~400 ns from the photoluminescence decay shown in **Figure 2.4**, the calculated diffusion length is ~12.65 μm, which is in good agreement with diffusion lengths measured on perovskite films by scanning photocurrent microscopy.[19,80,81]

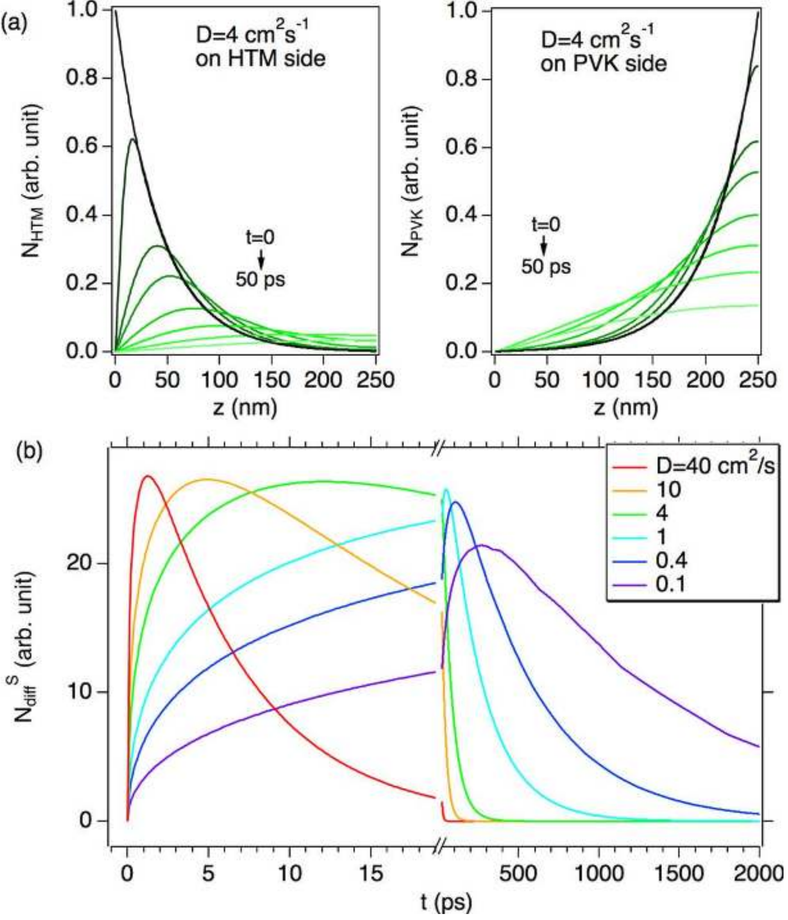

Figure 2.8. (a) Calculated hole distributions N_{PVK} and N_{HTM} as a function of distance z from the perovskite/HTM interface for excitation on the PVK and HTM sides at different times t. Diffusion constant $D = 4$ cm^2/s is used. (b) Calculated differential number of holes N_{diff}^S as a function of time after photoexcitation for different values of D. Copyright 2017 American Chemical Society.

The calculated $N_{diff}(t)$ cannot reproduce the overall time evolution of the experimental $\Delta T_{diff}/T$ signals quantitatively; $\Delta T_{diff}/T$ tends to rise faster and decay more slowly than $N_{diff}(t)$. The failure suggests that the hole transport in the vicinity of the $MAPbI_3$/HTM interface (within the hatched area of the "from HTM side" in **Figure 2.1a**)

is dominated by faster mechanisms than the diffusion. A previous photoemission study[82] reported that the stoichiometry of $MAPbI_3$ within a few nm of the interfaces can be affected by the substrates, and the interface can have a band bending as a result of the dipole formation. A comparative study on the device performance[44] also explained the insensitivity of V_{oc} to the VBM of the HTMs in terms of ionic accumulation at the interface causing steep band bending at the interface and a flat band in the rest of the perovskite. Such band bending with narrow width can induce ultrafast drift of the photoexcited holes only near the $MAPbI_3$/HTM interface and thereby enable sub-picosecond hole injection into the HTMs without significantly affecting the diffusion dynamics in the rest of the perovskite film.

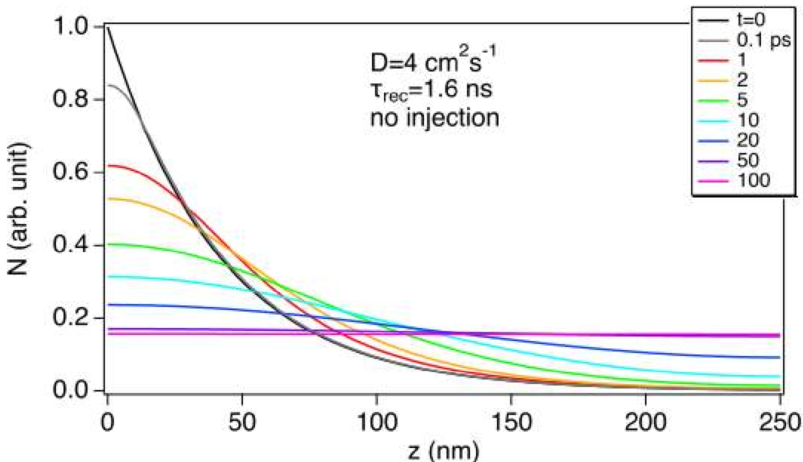

Figure 2.9. (a) Calculated carrier density N in the absence of HTM as a function of distance z from the photoexcited surface at different times t. Diffusion constant $D = 4\ cm^2/s$ and recombination time of $\tau = 1.6$ ns are used. The initial density at $t = 0$ has an exponential distribution corresponding to the absorption length of 42 nm.

2.9. Solar cell efficiency featuring the previously studied HTMs

We also fabricate the solar cells containing the same $MAPbI_3$/HTM interfaces and measure their EQE and current density–voltage (J–V) characteristics,[83] whose results are summarized in **Figure 2.3b** and **Table 2.1** as well as in **Figure 2.11** and **Figure 2.12**.

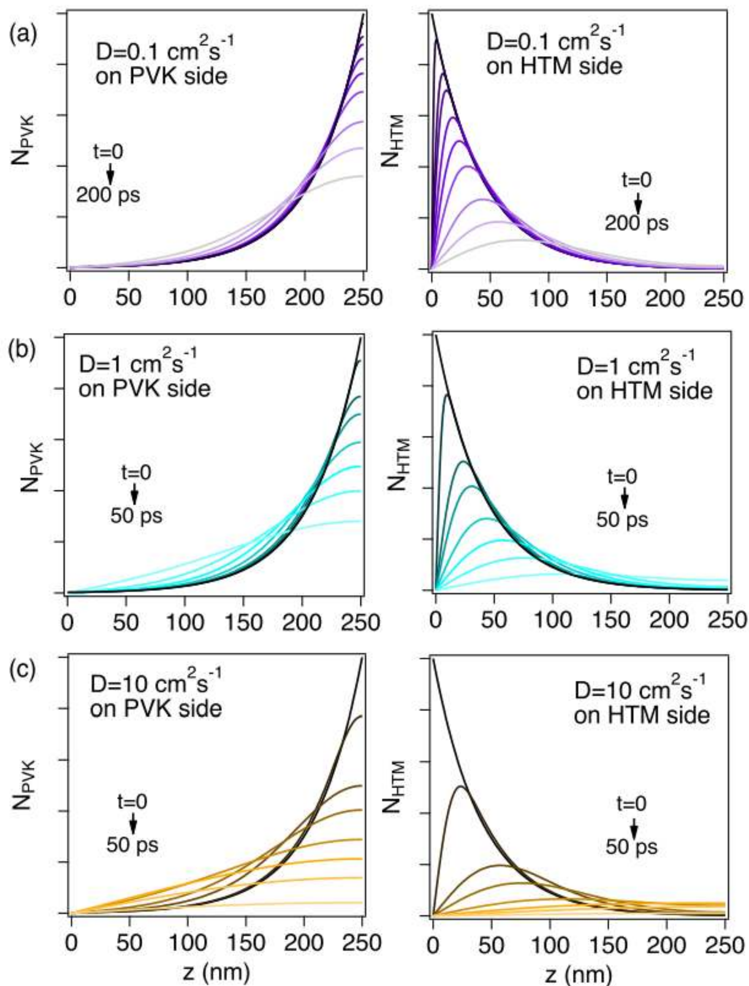

Figure 2.10. (a) Calculated carrier distributions $N_{PVK}(z,t)$ and $N_{HTM}(z,t)$ for photoexcitations on HTM and PVK sides as a function of distance z from the perovskite/HTM interface at different time after photoexcitation: in the case of diffusion constant $D = 0.1$ cm^2/s (a), 1 cm^2/s (b), and 0.1 cm^2/s (c). The recombination time of $\tau = 1.6$ ns is used in the calculations.

The solar cells with all of the HTMs exhibit good reproducibility in their device performance.[65,66,84] On one hand, the EQE at 400 nm hardly depends on the HTM despite the absorption by PTAA, suggesting comparable recombination near the $MAPbI_3$/HTM interfaces under the short-circuit condition. On the other, the values of V_{oc} do not directly correspond to the energy offset in the VBMs but are reduced considerably for the solar

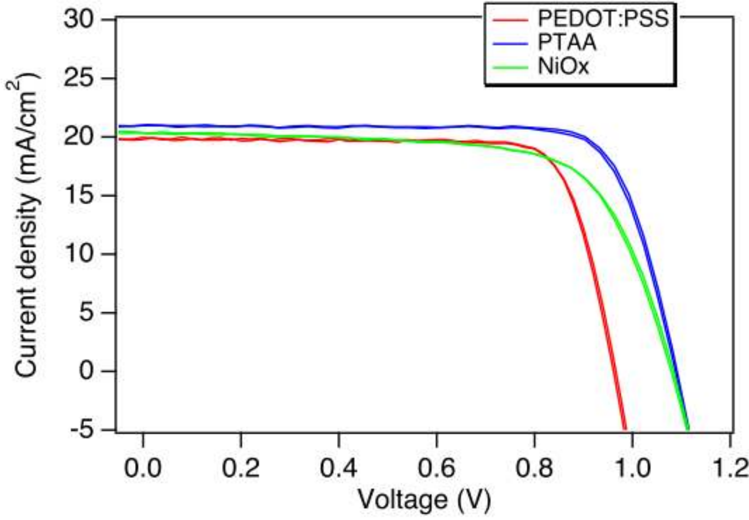

Figure 2.11. Current density-voltage curves for the solar cells with three different hole transport materials.

Table 2.1. Device parameters for solar cells with three different HTMs

HTM	J_{SC} (mA cm^{-2})	V_{OC} (V)	FF	PCE (%)	R_s (Ω cm^{-2})	R_{sh} (Ω cm^{-2})
PTAA	20.99	1.09	0.79	18.0	4.89	>10000
PEDOT:PSS	19.88	0.96	0.79	15.2	3.37	5701
NiO_x	20.34	1.08	0.69	15.2	5.99	1337

Parameters: short-circuit current density (J_{SC}), open-circuit voltage (V_{OC}), fill factor (FF), power conversion efficiency (PCE), series resistance (R_s), and shunt resistance (R_{sh}).

cells with PEDOT:PSS and NiO_x in comparison with those with PTAA. This is consistent with the most efficient hole injection to PTAA revealed in the present time-resolved study. Moreover, the solar cell with NiO_x shows the highest R_s and the lowest R_{sh}, indicating the poorest transport at the interface and in the perovskite as well as the largest power loss due to defects. It is likely that NiO_x, a hard inorganic semiconductor, induces more disorder and defects in the perovskite film fabricated on top of it due to the chemical reaction between the two materials[82] than the other two soft organic

semiconductors and thus results in the relatively poor device performance. Such a defective interface would also lead to slower hole injection, as we have seen in our transient transmission signals for the $MAPbI_3/NiO_x$ interface. The correlation between the carrier dynamics and the device performance will be further investigated over a wider range of HTMs, ETMs, and perovskites by the differential transient transmission technique. The physical mechanism behind the correlation will be examined by monitoring the carrier dynamics of the actual solar cells under working conditions in the transient reflection geometry.

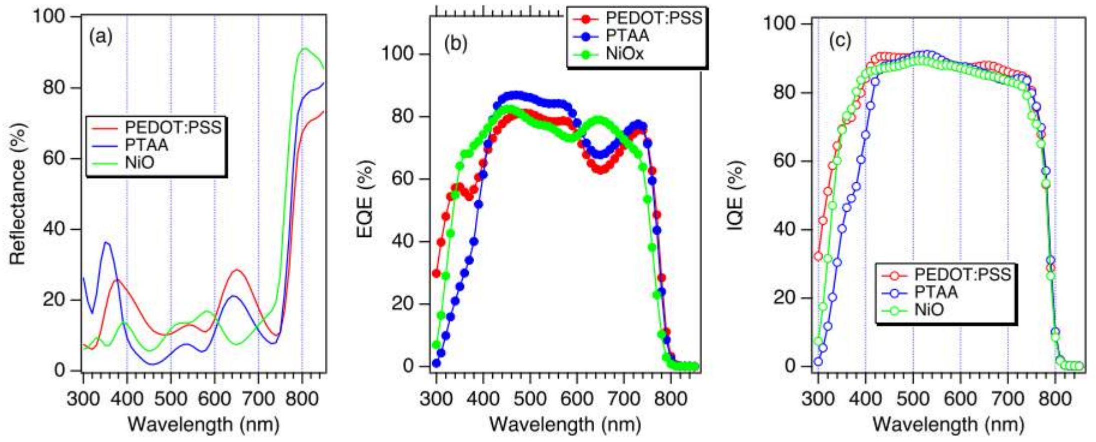

Figure 2.12. Reflectance (a), external quantum efficiency (b), and internal quantum efficiency (c) of the solar cells with three different hole transport materials.

2.10. Conclusions

In conclusion, we have directly monitored the hole injection dynamics at the interfaces of $MAPbI_3$with three different HTMs. The differential transient transmission signals have shown that the hole injection is complete within 1 and 2 ps at the $MAPbI_3$/PTAA and $MAPbI_3$/PEDOT:PSS interfaces. By contrast, the hole injection at the $MAPbI_3/NiO_x$ comprises two steps and takes 40 ps to be complete. The obtained carrier dynamics are consistent with the poor device performances of the solar cell with the HTMs examined. The differential transient transmission measurements thus proved to be

a powerful tool to investigate the interfacial carrier dynamics using a simple linear optical technique, and the knowledge obtained will contribute to explore novel HTM materials that enable high photovoltaic performance.

2.11. Methods and materials

2.11.1 Materials and preparation

All chemicals were purchased from commercial suppliers and used as received, unless stated otherwise. Perovskite precursors were prepared by dissolving PbI_2 [Kanto-chemical, 98% purity] in anhydrous N, N-dimethylformamide (400 mg mL^{-1}), and by dissolving the mixture of methyl ammonium iodide (MAI) and methyl ammonium chloride (MACl) [Wako Chemicals, battery grade] in the ratio of 19:1 in ethanol (50 mg mL^{-1}). Poly [bis(4-phenyl)(2,4,6-trimethylphenyl) amine] (PTAA) used for the hole transport layer (HTL) was dissolved in anhydrous chlorobenzene at 0.5 wt%. $PC_{61}BM$ [Sigma Aldrich, 99% purity] used as the electron transport layer (ETL) in the solar cells was dissolved in anhydrous chlorobenzene at 2 wt. %. All solutions were filtered through 0.45 μm syringe filters to avoid the risk of particle formation. Aluminum-doped zinc oxide (AZO) nanoparticle ink (Nanograde N-21X) was used to prepare the AZO layer.

2.11.2 Preparation of hole transport layers

Samples for spectroscopic measurements and solar cells for device characterizations were fabricated on glass substrates (S9111, Matsunami Glass) and on patterned ITO-coated glass substrates (15 Ω/square), respectively. A thin film of HTL, made of either PEDOT:PSS, PTAA or NiO_x was first prepared on the substrate. The PEDOT:PSS (Clevios, Al4083) film of ~30 nm thickness was formed by spin coating at 3000 rpm and subsequently drying at 120°C for 15 minutes on a hot plate in ambient air.[66] The PTAA

film of the similar thickness was prepared by spin coating the solution at 1000 rpm in a glove box filled with nitrogen and subsequently drying at 100°C for 5 min on a hot plate in nitrogen ambient.[84] The NiO_x ($2 < x < 3$) film of 60-70 nm thickness was prepared using an rf magnetron sputtering system (SVC-700 RFIINA, Sanyu Electron, Japan). The substrates were treated with ultraviolet-ozone for 20 minutes immediately before being loaded into the vacuum chamber (base pressure < 2 x 10^{-3} Pa). Sputter deposition was carried out at room temperature in an argon gas pressure of 0.5 Pa at a radio frequency power of 50 W, with sintered 99.9% pure NiO (Kojundo Chemical Laboratory co. Ltd., Japan) as the sputter target.[64,65]

2.11.3 Perovskite film fabrication

The rest of the fabrication procedures were performed in a glove box filled with nitrogen and with <1.0 ppm O_2 and H_2O. A PbI_2 film was first spin-coated at 3000 rpm for 90s and then the mixture of MAI and MACl was spun onto the PbI_2 layer at 4000 rpm for 90s to promote Cl-mediated interdiffusion.[66] The as-grown $MAPbI_3$ perovskite films were put into a closed container side by side with MACl powders and heated on hot plate at 100°C to promote crystallization.[67] The samples for the spectroscopic measurements were then coated with polymethyl methacrylate (PMMA) to make the surface inert.

2.11.4 SEM and XRD analysis

The scanning electron microscopy images were recorded at 5kV using an FE-SEM at 80x magnification (Hitachi FE-SEM S-4800). The XRD patterns were collected using an X-ray diffractometer (Rigaku SmartLab, Japan) (Cu Kα radiation, $\lambda = 1.54050$ Å).

2.11.5 Device fabrication

To fabricate the solar cells for device characterization, an ETL and a metal electrode were added on top of the perovskite instead of the PMMA coating. A thin layer of $PC_{61}BM$ was spun at 700 rpm for 60s, followed by coating with the AZO layer at 3000 rpm for 30s, as the ETL. A 100-nm thick Ag film was then deposited as a metal contact in an evaporation chamber at a pressure < 10^{-4} Pa that is connected to the glove box. Solar cell devices with area of ~0.26 cm^2 were then sealed using UV-curable resins (UV RESIN XNR5516Z, Nagase ChemteX, Japan) before the characterization in ambient conditions.

2.11.6 Device performance characterization

The current density-voltage (J-V) curves of the solar cells, shown in **Figure 2.11**, were measured by a commercial software (SYSTEMHOUSE SUNRISE corp., Japan) using 1 SUN illumination (AM1.5G) from a solar simulator (Bunkokeiki, Japan). The devices with area of 0.19 cm^2 were defined by an aperture mask. Short circuit current J_{SC}, open circuit voltage V_{OC}, fill factor FF, photoconversion efficiency PCE, series and shunt resistances R_s and R_{sh} were derived from the J-V curves, as summarized in **Table 2.1**. The external quantum efficiencies (EQE) and the reflectance R were measured and plotted in **Figure 2.12**. The internal quantum efficiencies IQE were obtained from the relation IQE=EQE/(1-R).

2.11.7 Photoluminescence decay characterization

The emission spectra reported in **Figure 2.4a** were taken using excitation light at 470 nm using a fluorescence spectrometer (JASCO, FP8500). The fluorescence lifetime decay curves in **Figure 2.4b** were recorded using a picosecond fluorescence lifetime system

equipped with a pulse laser at 403 nm for excitation. The emission decays were recorded at 760 or 765 nm.

2.11.8 Transient transmission measurement methods

Pump-probe transmission measurements on the $MAPbI_3$/HTM samples are performed under ambient conditions using a Ti:sapphire regenerative amplifier (RegA-9000, Coherent) with 150-fs duration and 100-kHz repetition rate as the light source. The second harmonic of the amplifier at 400-nm wavelength is used as the pump, whereas the output of an optical parametric amplifier (OPA, Coherent) at 720-nm wavelength serves as the probe. The pump and probe beams are focused onto an identical spot on the sample surfaces with their spot sizes of 500 and 200 μm in diameter. The pump density is kept at ~ 0.5 $\mu J/cm^2$ (carrier density ~ 2 x 10^{17} cm^{-3}) to avoid the irreversible photodegradation of the sample, unless otherwise noted. The pump beam is modulated at 1.98 kHz for lock-in detection. The probe lights before and after transmitting the sample are detected by a pair of balanced Si PIN photodetectors. Pump-induced changes in the transient transmission $\Delta T{=}T$ are recorded as a function of time delay between pump and probe pulses t using a conventional slow scan technique. The transient transmission changes $\Delta T_{HTM}{=}T$ and $\Delta T_{PVK}{=}T$ are obtained with the pump and probe lights incident on the HTM and perovskite (PVK) sides of the $MAPbI_3$/HTM samples, respectively. The differential transient transmission $\Delta T_{diff} / T \equiv (\Delta T_{PVK} - \Delta T_{HTM}) / T$ is calculated to extract the carrier dynamics occurring in the direct vicinity of the HTM interface.

2.11.9 Diffusion simulations

We perform numerical simulations to estimate the hole transport dynamics in the perovskite film. We consider the diffusion equation for the hole density $N(z, t)$ as a

function of the distance z from the perovskite/HTM interface and time t after photoexcitation:

$$\frac{\partial N}{\partial t} = D\frac{\partial^2 N}{\partial z^2} - \frac{N}{\tau}$$

Here D and τ denote the diffusion constant and the hole recombination time. The initial condition is given by:

$N_{HTM}(z, t = 0) = N_0 e^{-\alpha z}$ for excitation on HTM side

$N_{PVK}(z, t = 0) = N_0 e^{[-\alpha(d-z)]}$ for excitation on PVK side

with α and d being the absorption coefficient of the pump light in the perovskite and the perovskite film thickness. The boundary conditions in the absence of the HTM are given by:

$$\left.\frac{\partial N}{\partial z}\right|_{z=0} = \left.\frac{\partial N}{\partial z}\right|_{z=d} = 0.$$

In the presence of the HTM layer, the boundary conditions are:

$$N_{HTM}(z = 0, t) = 0; \quad \left.\frac{\partial N_{HTM}}{\partial z}\right|_{z=d} = 0$$

for excitation on the HTM side and

$$\left.\frac{\partial N_{PVK}}{\partial z}\right|_{z=0} = 0 \quad ; \quad N_{PVK}(z = d, t) = 0$$

for excitation on the PVK side.

Because the diffusion constant D reported in previous studies ranges widely depending on the crystalline quality, from 0.01 to 4 cm^2/s,[51,58,77–79] we calculate the diffusion with different values of D. **Figure 2.9** plots the calculated hole distribution $N(z; t)$ in the absence of the HTM layer in the case of D=4 cm^2/s. The distributions in the presence of the HTM layer are similarly calculated but in the two measurement geometries, whose

examples are shown in **Figure 2.10** as well as in **Figure 2.8a**. We then obtain the differential population of the holes in the film:

$$N_{diff}(t) \equiv N_{PVK}^{S}(t) - N_{HTM}^{S}(t) = \int_0^d N_{PVK}(z,t)dz - \int_0^d N_{HTM}(z,t)dz$$

whose results are summarized in **Figure 2.8b**, to compare the simulation results direction with the experimental differential transient transmission $\Delta T_{\text{diff}} / T$.

CHAPTER 3

SUB-BANDGAP RESPONSE OF GRAPHENE/SIC SCHOTTKY EMITTER BIPOLAR PHOTOTRANSISTOR EXAMINED BY SCANNING PHOTOCURRENT MICROSCOPY[2]

3.1. Introduction

Ultraviolet (UV) detection is an important detection tool for military, industrial, chemical, and biological applications. Typical UV detection includes the use of photomultiplier tubes (PMTs) or semiconductor *p-n* junction photodiodes that collect electron-hole pairs generated by UV photons. UV radiation is above the bandgap of typical semiconductors based on Si, SiC, GaN, AlGaN, InGaAs, and GaAs, making detection easy in principle. However, UV makes up only a small portion of the daylight spectrum and visible light absorption can easily overwhelm the typical UV signal. Moreover, penetration of UV into such materials is very limited with much absorption occurring in heavily-doped near-surface "dead" layers. The inherent visible blindness found in wide-bandgap semiconductors is therefore a desirable quality for UV detectors if architectures with high detectivity and UV-transparent contacts can be identified.

Recently, UV detection has been demonstrated in bipolar phototransistors featuring a transparent epitaxial graphene (EG) emitter grown on a *p*-SiC base epilayer on *n*-type SiC substrates. This Schottky-emitter bipolar phototransistor (SEPT) relies on efficient minority carrier injection from the carefully prepared *p*-type Schottky barrier. In

---

[2] Reprinted with permission from Barker, B. G.; Chava, V. S. N.; Daniels, K. M.; Chandrashekhar, M. V. S.; Greytak, A. B. *2D Mater.* **2018**, *5* (1). https://doi.org/10.1088/2053-1583/aa90b1. Copyright 2018 IOP Publishing.

particular, a maximum common emitter current gain of 113 with minority carrier injection efficiency of >99% has been demonstrated.[85] However, the visible rejection ratio (VRR) and localized photocurrent response were not analyzed in the initial report. Due to the high UV responsivity previously reported (7.1 A/W)[85], it is important to determine whether the visible-rejection ratio has been sacrificed in the attempt to improve performance.

There are several possible origins of sub-bandgap response, including heteropolytype junctions, donor-acceptor pair (DAP) absorption, and internal photoemission. The Franz-Keldysh effect can lead to sub-bandgap absorption but is not expected to play a large role here due to the modest electric field and indirect bandgap. SiC exists in several polytypes with varying band gaps. In this particular device, 4H-SiC (3.23 eV) is used to absorb UV light. Stacking faults in SiC manifest as other polytypes with smaller bandgaps, specifically 3C- (2.40 eV), 6H- (3.0 eV), or 8H-SiC (2.86 eV),[86] which could lead to a spatially dependent visible response within the device area. A more homogenous contribution to sub-bandgap photocurrent is expected within the area of the EG contact from the other effects mentioned. Due to the large dopant ionization energies in SiC, DAP states have been shown to lead to luminescence and photoconductivity in the visible region.[87,88] Thermal equilibrium between DAPs and band-edge states could give rise to carriers with a sufficient effective mobility to explain the transistor action. Internal photoemission can be evaluated on the basis of the photon energy dependence.

Here, we used scanning photocurrent microscopy (SPCM) with sub-bandgap excitation (444 nm) to map the spatial extent of the photocurrent response and examine the influence of localized polytypes on the sensitivity to sub-bandgap light. SPCM is a

technique that uses a raster-scanned local excitation spot to identify spatial variations in photocurrents, which can be used to identify localized defects and examine characteristic length scales for carrier transport devices. SPCM has emerged as a valuable tool for functional imaging of optoelectronic materials[1], such as semiconductor nanowires[2–5], two-dimensional semiconductor materials[14], nanoporous layers of dye-sensitized solar cells[15,16], and perovskite absorbers[19,20]. The spatial resolution of SPCM allows for clear representation of polytype heterojunctions, should they exist, and allows for us to discriminate between localized and homogenous origins of sub-bandgap response. By choosing to illuminate at 444 nm, we can resolve SiC polytypes that exist in the visible absorption range. Additionally, we directly measured the action spectrum using collimated monochromatic light.

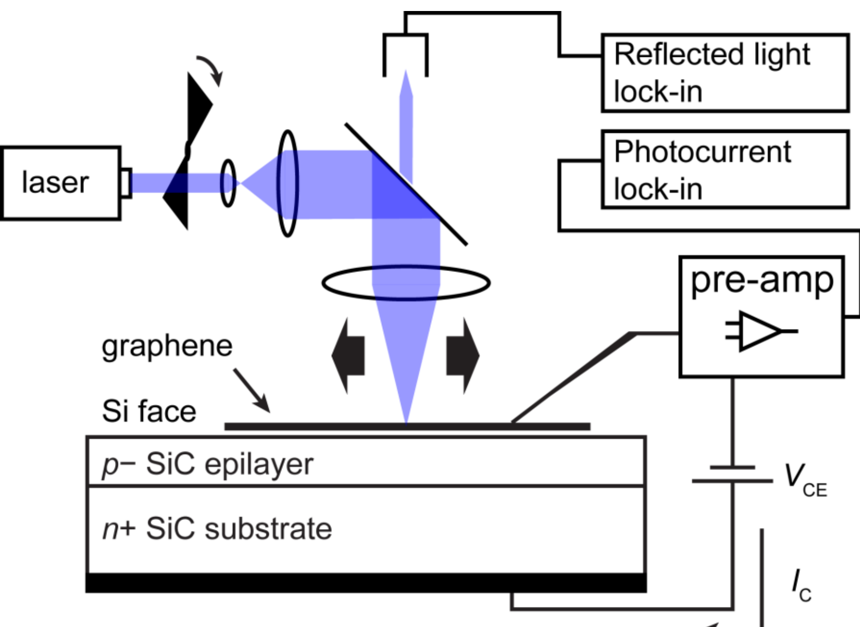

Figure 3.1. Schematic of SPCM setup for analysis of EG/SiC SEPT device. Voltage is applied through a tungsten probe arm contacted to the graphene surface. A pre-amplifier and lock-in amplifier are used to isolate the photocurrent signal at the frequency of the chopped laser light. The reflected laser signal is also captured and is used to map the physical features of the device. Copyright 2018 IOP Publishing.

3.2. SPCM experimental setup and device operation

Figure 3.1 schematically represents the device architecture and contact arrangement. A *p*-SiC base epilayer with acceptor concentration ~3×10^{14} cm^{-3} and thickness ~30 μm is grown by CVD on commercially available (0001) 4° off-axis Si-face n^+-SiC wafers. The EG is grown by thermal sublimation of the *p*-SiC epilayer surface in vacuum at 1350°C. The fabrication of this device and spectroscopic investigation of similar EG film samples are described elsewhere.[85,89,90] The EG is a continuous film 2-3 monolayers thick and oxygen plasma reactive ion etching is used to define 275 μm diameter circular emitter contacts. The etching process removes EG outside of the contact area but does not penetrate the *p*-SiC base epilayer. The sample was then placed in an Aixtron horizontal hot-wall reactor where the sample was ramped to 1400°C, in 60 slm of Ar flow at 200 mbar to prevent additional growth of EG and promote the desorption of water and other molecules possibly on the EG surface after being exposed to air. The sample was cooled to 1050°C, and gas switched to H_2 flowing at 80 slm at 900 mbar for 60 minutes. This causes hydrogen passivation of the Si dangling bonds on the SiC epilayer, eliminating the covalent bonding between the epilayer and the first carbon layer, 6√3 buffer layer, which is promoted to an additional monolayer of EG and forms quasi-freestanding EG. The polarization field from the hexagonal epilayer gives rise to a *p*-type charge density of ~1×10^{13} cm^{-2} in the quasi-freestanding EG, from ~$5x10^{12}cm^{-2}$ *n*-type observed prior to intercalation.[91]

Under operation, the graphene film is contacted directly through the use of a tungsten probe. The voltage between the substrate (contacted through the bottom side) and probe is controlled to bias the device. A potential barrier of ~0.5eV is reported for EG/n-SiC

and a high barrier of ~2.7eV for p-SiC on the SiC substrate (0001) surface.[90,92] **Figure 3.2** shows a band diagram for the SEPT device in three different operating modes. **Figure 3.2a** shows the device at zero bias. When the substrate is brought to positive voltage with respect to the probe, such that the graphene acts as the emitter and the substrate as the collector, this defines "graphene emitter" mode, with $V_{CE} > 0$ (**Figure 3.2b**). If the graphene is instead brought to positive voltage with respect to the substrate, so that the EG/SiC contact acts as the collector, this defines "graphene collector" mode (**Figure 3.2c**). To avoid confusion, we will use negative values of V_{CE} to denote measurements in graphene collector mode.

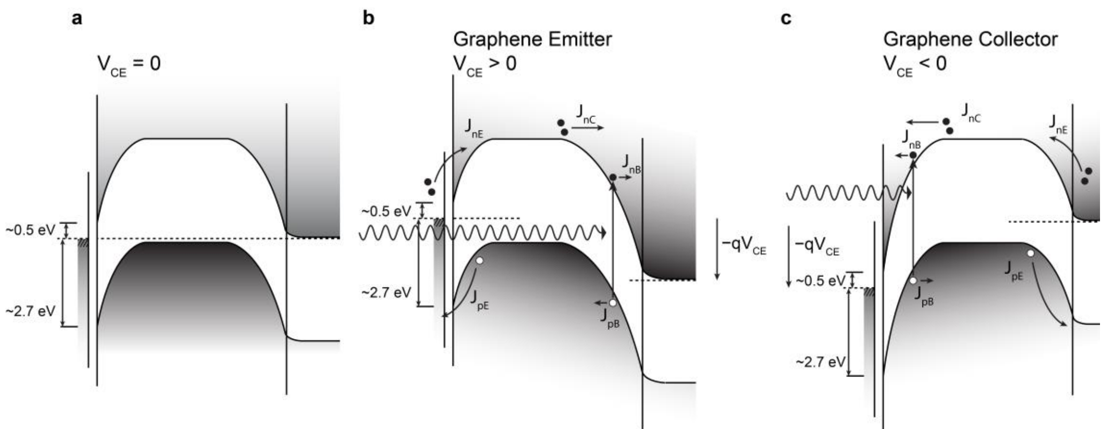

Figure 3.2. (a) SEPT device at V_{CE}=0. (b) SEPT device in graphene emitter mode (V_{CE}>0). Electron-hole pairs are generated by light absorption. Holes are reflected from the graphene by the large Schottky barrier, and in response, electrons are injected from the graphene emitter into the base region and move to the collector region, contributing gain. (c) SEPT device in graphene collector mode (V_{CE}<0). Copyright 2018 IOP Publishing.

To form SPCM images, a mechanically chopped, focused laser spot is scanned over the sample. Dual lock-in amplifiers allow for simultaneous recording and mapping of the resulting photocurrent and the specularly reflected laser beam, enabling good registry of SPCM maps with structural features. The photocurrent measured through the lock-in

amplifier represents only the photocurrent that occurs at the same frequency as the scanned laser beam.

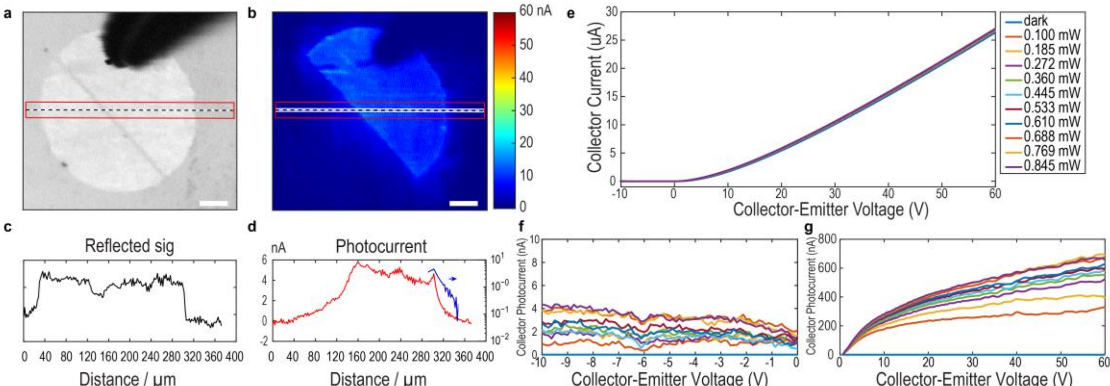

Figure 3.3. (a,b) Simultaneously recorded reflected light and AC photocurrent maps of a SEPT device in graphene collector mode under 444nm (sub-bandgap) excitation (V_{CE}=−10 V, 2.24 mW, chopped at 284 Hz). The circular graphene electrode has been scribed to form two separate devices; photocurrent is only detected from the device contacted by the tungsten probe arm (dark shape at the top of images). Scale bars, 50 µm. (c,d) Signal profiles of the reflected light and photocurrent images along the lines indicated in (a,b). Signals are averaged in the orthogonal direction within the width indicated by the red boxes. Blue trace in d shows the near-exponential decay of the falling edge signal in the photocurrent profile. (e) Current-voltage characteristics of the device from V_{CE}=−10V (graphene collector) to V_{CE}=60V (graphene emitter). A large dark current results from the base-collector junction at positive voltages due to poor isolation of the junction. (f) DC photocurrent of the device in graphene collector mode ($V_{CE} < 0$). (g) DC photocurrent of the device in graphene emitter mode ($V_{CE} > 0$). Copyright 2018 IOP Publishing.

3.3 SPCM results under normal device operation

Figure 3.3 presents an SPCM image, as well as spot current-voltage (I-V_{CE}) curves, recorded for a representative device under 444 nm excitation. In this particular device, the circular EG electrode has been scribed to form two separate semi-circular devices, as can be seen in the specular reflection map (**Figure 3.3a**). The SEPT devices generally display a large dark current at positive V_{CE} (graphene emitter mode), likely because the SiC *p-n* junction, which is at reverse bias in this condition, is poorly rectifying because it is not mesa isolated. In contrast, very little dark current ($\ll$ 1 nA) is observed at $V_{CE} < 0$

(graphene collector mode), suggesting a high degree of rectification at the EG/*p*-SiC Schottky junction.

Notably, a non-zero photocurrent is detected under 444 nm illumination in both modes, indicating that this radiation is capable of exciting a base current. However, the maximum responsivity is much smaller, by a factor of $\sim 10^3$, than that recorded under UV. The photocurrent in graphene emitter mode is more than 100 times larger than for graphene collector, a contrast that is also observed under UV illumination of this and similar devices, suggesting a common carrier transport process for photocurrent appearing under visible and UV excitation.

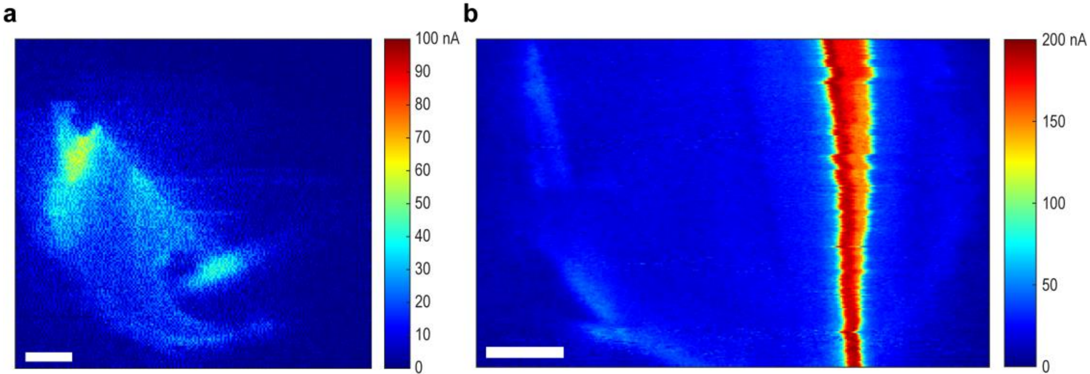

Figure 3.4. (a) SPCM map of a SEPT device in graphene emitter mode (V_{CE} = 20V) on the opposite side of the same device in **Figure 3.3**. (b) SPCM map of a SEPT device in graphene emitter mode (V_{CE} = 20V) on the same device as **Figure 3.7** showing a localized stacking fault. Scale bar = 50 µm.

Figure 3.3b shows a representative SPCM map of this device at $V_{CE} = -10$V (graphene collector). The response is clearly seen to be strongly localized to the graphene electrode that is directly contacted by the probe arm. The fact that photocurrent is only collected from one of two devices in close proximity confirms the role of EG as a transparent and conductive emitter (or collector) contact in the device architecture. The high in-plane conductivity of the EG layer is illustrated by a flat response within the contiguous region.

A similar pattern is observed in graphene emitter mode (**Figure 3.4a**); however, the very low dark current and low gain in graphene collector mode results in detailed functional SPCM images. The edge of the EG region results in a sharp cutoff in the reflected signal of the device as seen in the profile plotted in **Figure 3.3c**. In contrast, the edge of the corresponding photocurrent signal (**Figure 3.3d**) shows a measurable roll-off with distance with an approximately exponential profile. The logarithmic slope suggests a decay constant of about 10 µm.

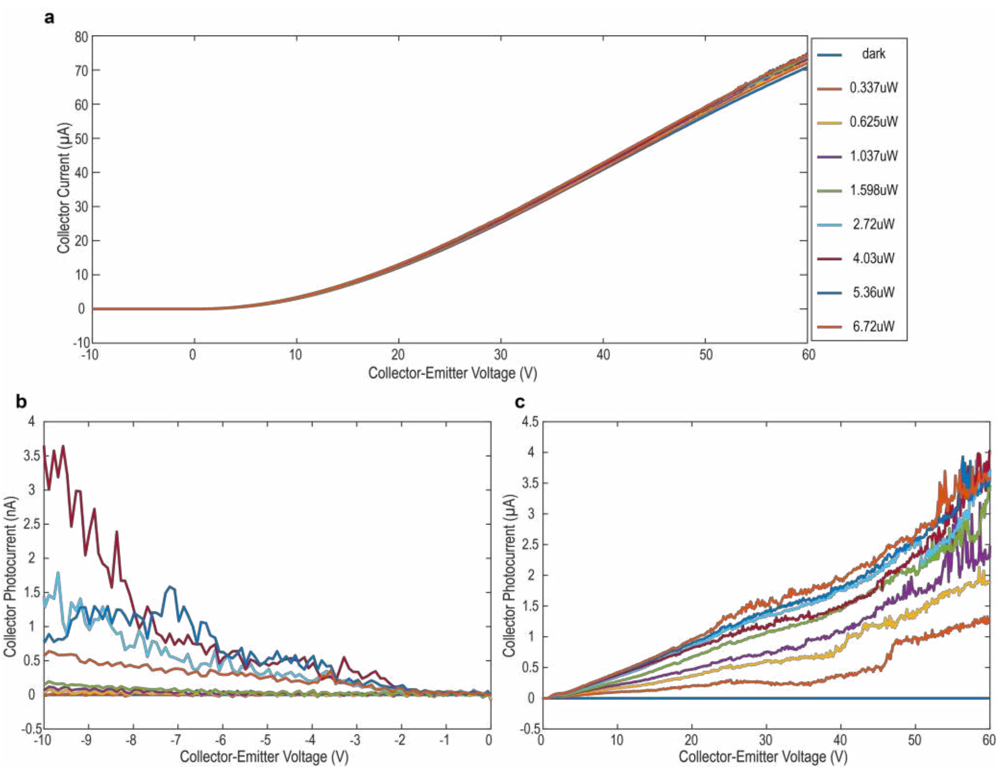

Figure 3.5. (a) Current-voltage characteristics of the device from V_{CE}=-10V (graphene collector) to V_{CE}=60V (graphene emitter) in the dark and under UV (365 nm) illumination. (b) Photocurrent of the device in graphene collector mode ($V_{CE} < 0$). (c) Photocurrent of the device in graphene emitter mode ($V_{CE} > 0$).

3.4. Responsivity, absorption, gain, and visible-rejection ratio in graphene-emitter mode

The large UV responsivity observed for the SEPT device is a direct consequence of the large photocurrent gain h_{FE} that is achieved in graphene-emitter mode. In the previous report, h_{FE} was calculated on the basis of the observed photocurrent, and an estimate of the maximum base current that could be generated by light absorption within the entire base width W_B from the known absorption coefficient α_{abs} of 4H-SiC (80 cm^{-1} at 365 nm).[93] An absorbing layer of thickness W that has absorption coefficient α_{abs} at photon energy E_λ can be expected to generate a maximum "base responsivity" R_b, corresponding to transit of one electron per photon absorbed, given by: $R_b = \frac{1-e^{-\alpha_{abs} \cdot W}}{E_\lambda}$, where R_b is in A/W and E_λ is given in eV. This can be compared to the measured total responsivity responsivity $R = I/P$. For a bipolar phototransistor, R_b represents the base current, and R is related to it by the optical gain h_{FE}: $R = \frac{I}{P} = (1 + h_{FE}) \cdot \frac{I_B}{P} = (1 + h_{FE})\, R_b$. For SiC under 365 nm illumination, the absorption coefficient is 80 cm^{-1}. Accordingly, the maximum base responsivity at this wavelength considering absorption along the entire base layer width ($W = W_B$ = 30um) is: $R_b = \frac{1-e^{-\alpha \cdot W_B}}{E_{365}} = 0.0627$ A/W.

In spot measurements under 365 nm excitation, the photocurrent responsivity was found to increase slowly with increasing V_{CE} and was maximized at low incident power (**Figure 3.5** and **Table 3.1**). The maximum observed responsivity was 3.7 A/W, comparable to the 7.1 A/W reported previously, and indicating current gain of at least h_{FE} = 58 for the present device. For sub-bandgap excitation at 444 nm, the maximum responsivity was 3.3×10^{-3} A/W, corresponding to a visible-rejection ratio $>10^3$ between

365 and 444 nm. The 4H- polytype is nominally transparent at 444 nm (bandgap ca. 3.2 eV or 387 nm), but comparison of the observed responsivities can be used to assign a minimum absorption coefficient $\alpha_{abs} \approx 0.052$ cm^{-1} at 444 nm if h_{FE} is considered to be independent of the photon energy: that is, that the transport process following visible excitation is fundamentally the same as following UV excitation. As discussed below, a plausible explanation for this absorbance is DAP excitation in the base epilayer that results in base current through thermal or field-assisted ionization into band-edge states.

Table 3.1. Responsivity of a SEPT device at V_{CE} = 60 (graphene emitter).

Laser Power at 444 nm (μW)	Photocurrent (nA)	Responsivity (A/W)	Incident Power at 365 nm (μW)	Photocurrent (μA)	Responsivity (A/W)
100	333	3.31×10^{-3}	0.337	1.25	3.70
185	367	1.98×10^{-3}	0.625	1.91	3.05
272	533	1.96×10^{-3}	1.037	2.68	2.58
360	533	1.48×10^{-3}	1.598	3.55	2.22
445	567	1.27×10^{-3}	2.72	3.90	1.43
533	567	1.06×10^{-3}	4.03	3.99	0.99
610	633	1.04×10^{-3}	5.36	3.57	0.67
688	667	9.69×10^{-4}	6.72	3.65	0.54
769	667	8.67×10^{-4}			
845	633	7.50×10^{-4}			

3.5. Responsivity, absorption, gain, and visible-rejection ratio in graphene-collector mode

In graphene-collector mode, a much smaller photocurrent is detected than for graphene-emitter, both under UV excitation and at 444 nm. This value indicates minimal gain corresponding to base transport factor $\alpha_T \ll 1$. A possible reason for this is a large surface recombination velocity at the EG/SiC interface. The absence of bipolar gain in this mode offers another opportunity to examine the absorption coefficient below the SiC bandgap. For a photodiode at reverse bias, photocurrent should scale with depletion width W_D as it

is in this region that carriers can be most effectively separated. If so, the photocurrent should increase approximately as the square root of the applied voltage, and such an increase is indeed observed up to $V_{CE} \approx -10$ V. Larger biases led to noisy signals and were thus avoided in the present studies. The expression for the base-collector depletion width, W_D, under applied bias is as follows: $W_D = \sqrt{\frac{2\varepsilon(V_{bi}-V)}{qN_a}}$, where ε is the dielectric permittivity of the semiconductor ($\varepsilon = \varepsilon_r\varepsilon_0$ with $\varepsilon_r = 10$ for SiC), V_{bi} is the built-in voltage (taken as 2.7 V), V is the applied bias (= $-V_{CE}$), q is the elementary charge, and N_a represents the net ionized acceptor density.

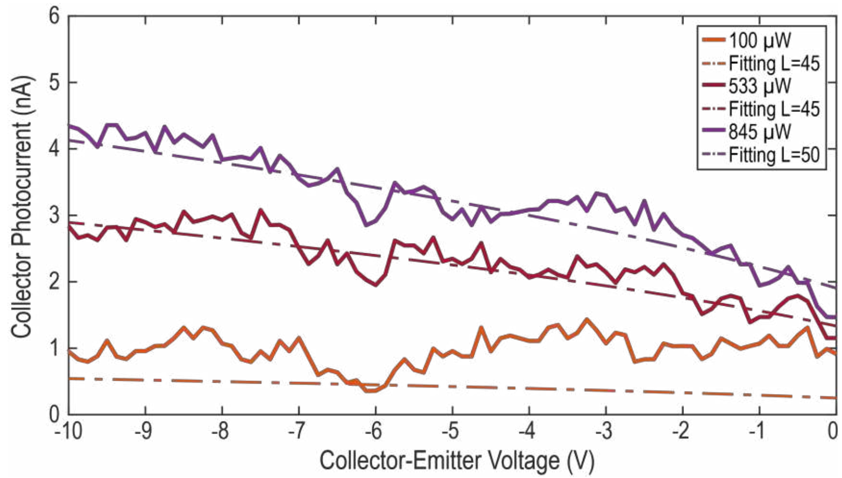

Figure 3.6. Estimation of the absorption length of donor-acceptor pair absorption in a SEPT device measured at $V_{CE} < 0$V (graphene collector) under 444 nm illumination.

Given the low gain in graphene-collector mode, we can model the dependence of the photocurrent on voltage by considering photocurrent generation to be limited to the depletion zone ($W = W_D$), with the absorption length $L = \alpha_{abs}^{-1}$ entering as a parameter: $I \propto \frac{P(\lambda)}{E_\lambda} = \frac{P_0(\lambda)}{E_\lambda}\left(1 - e^{-W_D/L}\right)$, where $P_0(\lambda)$ is the incident laser power at a given wavelength and E_λ is the photon energy in electron volts. **Figure 3.8** shows the predicted I vs $-V_{CE}$ curve overlaid on the experimental data at several optical powers assuming one

electron per absorbed photon, and a value of $L \approx 50$ cm as indicated. This corresponds to $\alpha_{abs} \approx 0.02$ cm^{-1} at 444 nm, which represents a lower bound for the absorption coefficient, as the actual quantum yield may be less than unity. Overlaying calculated photocurrent vs. voltage curves on the data from **Figure 3.3f** (**Figure 3.6**) allows the assignment of a minimum $\alpha_{abs} \approx 0.02$ cm^{-1}, which is on the same order as α_{abs} estimated in graphene-emitter mode.

3.6. Localized photocurrent signals – including an 8H- stacking fault

Notably, the photocurrent signal profile (**Figure 3.3g**) shows that photocurrent generation is localized to the portion of the device connected to the probe arm, confirming the role of the EG/p-SiC junction in the function of the SEPT device. However, the large difference in responsivity between graphene collector and graphene emitter modes suggests that carrier transport may be strongly limited by recombination at the EG/*p*-SiC interface. In a bipolar phototransistor, the majority of base current generation occurs at the base-collector interface, as this region is depleted and possesses the largest electric field. Consequently, surface recombination is expected to much more strongly influence the gain in graphene-collector mode. Surface recombination will also tend to limit lateral transport of electrons in the base over distances larger than the depletion width W_D (in graphene-collector mode) or base width W_B (in graphene-emitter mode). Consistent with this picture, the photocurrent response is more strongly localized in graphene-collector than in graphene-emitter mode.

SPCM also reveals localized features in these SEPTs that increase visible photoresponse. In the SPCM micrograph in **Figure 3.7a**, recorded for a different device on the same chip as the device in **Figure 3.3**, the circular shape of the graphene electrode

is overlaid by a prominent feature with the shape of a slender right triangle that displays an elevated response under 444 nm excitation. This feature is prominent in graphene collector and graphene emitter mode SPCM images and is not associated with any surface features visible in the reflected light image. The shape and orientation of these responses provide insight as to the type and origin of the defect. In 4H-SiC epitaxial structures, basal plane dislocations have been shown to nucleate stacking faults (SF) of smaller bandgap 3C- and 8H- polytypes[94,95] that absorb blue light.[96] The shape and orientation of this defect are hallmarks of a triple or quadruple Shockley stacking fault (3SSF or 4SSF) in the 4H-SiC base epilayer.[97,98] The length of the defect, which extends to the projected length of the epilayer thickness, indicates an in-grown stacking fault propagating from the substrate interface. With the 4° miscut and 30 µm p-SiC epilayer used here, the resulting stacking faults should extend $30\mu m/_{\tan 4°} \approx 400\mu m$ before intercepting the surface, as is observed here. Such defects most commonly appear as the 4SSF type.[98] The 4SSF can equivalently be described as the inclusion of a complete layer of 8H-SiC, with thickness ~2 nm, within the 4H-SiC crystal. The localized character of this feature and the low and flat background response make it prominent in SPCM images.

Figure 3.7c and Figure 3.7d show the photocurrent resulting from the absorption of 444 nm light centered on the apparent stacking fault in graphene collector and graphene emitter mode, respectively. In graphene collector mode, as the bias is increased, the photocurrent reaches a constant value that varies linearly with light intensity (**Figure 3.7c and Figure 3.8a**), possibly indicating an activated process for base current generation following initial excitation of states specific to the SF. In graphene-emitter mode, the

impact of the SF is most prominent at low voltage (<10 V) and light intensity, as the response with respect to power and voltage appears to saturate at modest values. When operated at V_{CE}=60 V, a responsivity of 4.60×10^{-3} A/W was measured on the feature at under 100 μW of 444 nm illumination, which is only slightly larger than the 3.31×10^{-3} A/W reported for the device in **Figure 3.3** and is also much lower than the responsivity under UV excitation. This indicates that this SEPT architecture may be resilient to the influence of common SiC defects under normal operation.

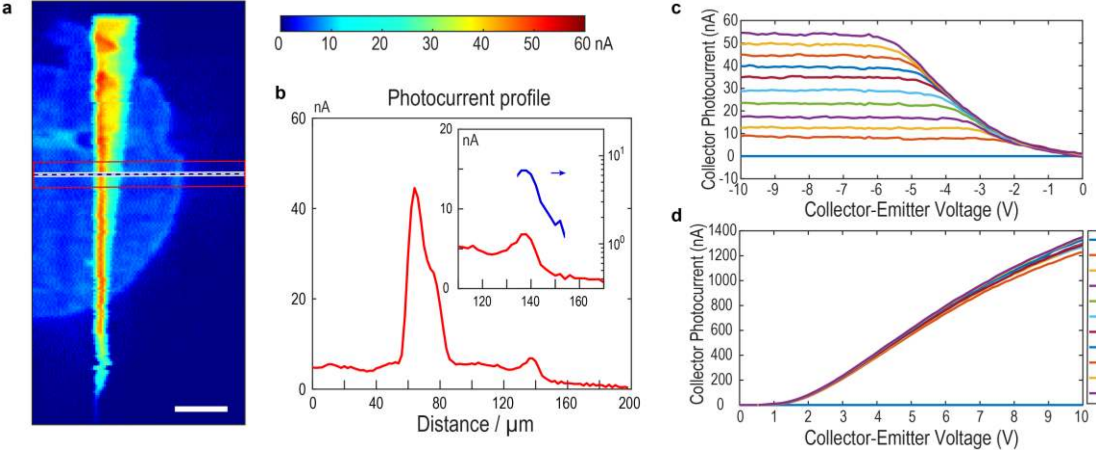

Figure 3.7. (a) AC photocurrent map of a separate SEPT device in graphene collector mode showing the presence of a localized region of enhanced sub-bandgap response, using same measurement condition as in **Figure 3.3**. Scale bar, 50 μm. (b) Photocurrent profile along the line indicated in a. Inset: Magnified view and log scale trace of falling edge of graphene contact. (c,d) Photocurrent-voltage characteristics of the device when illumination is centered on the bright feature in graphene collector and graphene emitter mode, respectively. Copyright 2018 IOP Publishing.

3.7. Band-edge response and investigation of the origins of sub-bandgap photocurrent

To characterize the band edge response and possible origins of sub-bandgap photocurrent generation in the SEPT devices, we recorded the action spectrum (responsivity versus wavelength) of the devices shown in **Figure 3.3** and **Figure 3.7**, in

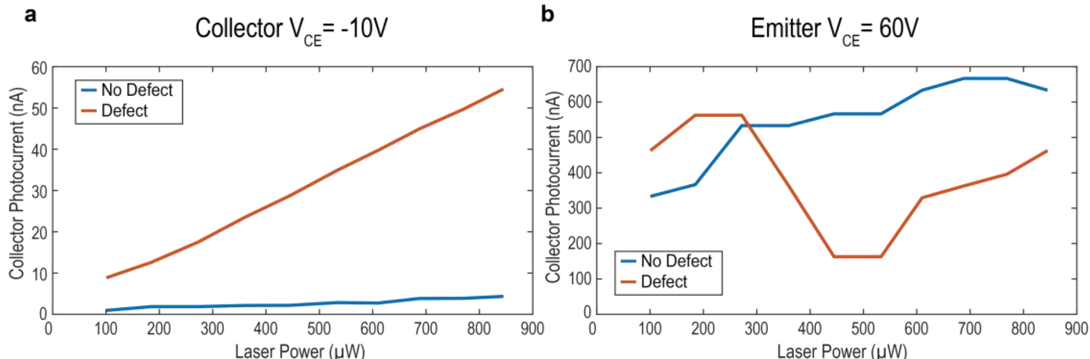

Figure 3.8. (a) Photocurrent versus laser power for a device without stacking faults (blue) and with a localized stacking fault (orange) at V_{CE} = -10V (graphene collector) under 444 nm illumination. (b) Photocurrent versus laser power for a device without stacking faults (blue) and with a localized stacking fault (red) at V_{CE} = 60V (graphene emitter) under 444 nm illumination. While the total photocurrents of these devices are different, the shape of the signals are similar in graphene emitter mode, but the stacking fault introduces a significantly increased linearly dependent photocurrent in collector mode.

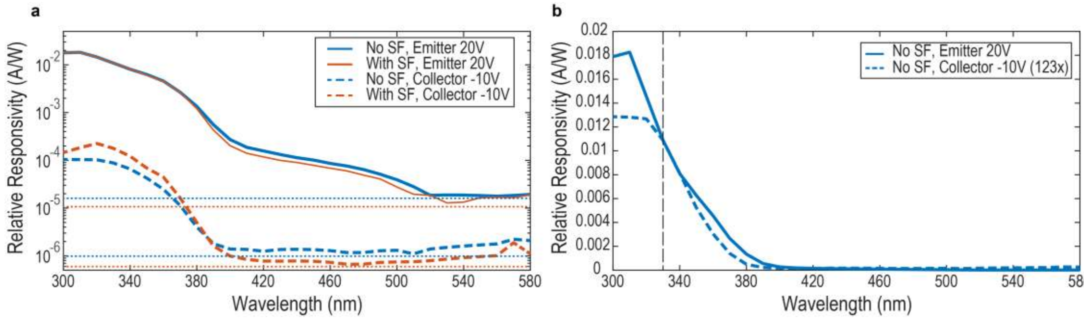

Figure 3.9. Action spectrum (relative responsivity versus wavelength) for SEPT devices under collimated illumination at 287 Hz. (a) Log-scale action spectra at V_{CE}=+20V and V_{CE}=−10V for each of the devices shown in **Figures 3.3** and **3.4**. Incident optical power is obtained by measured photon flux by EG mesa area. The detection limit marked by correspondingly colored fine dotted lines. The two devices have slightly different detection limts based on their active areas. (b) Action spectra of device without SF in graphene emitter and graphene collector modes, plotted on a linear scale. The action spectrum in graphene collector (V_{CE}=−10V) has been multiplied to give the same value at 330 nm to facilitate comparison. Copyright 2018 IOP Publishing.

graphene emitter and graphene collector modes. **Figure 3.9** shows results recorded under collimated, wide-area excitation light emerging from a monochromator paired with a xenon lamp. The photon flux was measured with a calibrated Si diode and was multiplied

by the active SEPT device area to obtain the incident optical power, by which responsivity was calculated from the measured photocurrent.

The spectral shape between the two samples in each mode is similar, with the photocurrent rising steeply at wavelengths shorter than the SiC band edge. This indicates that a majority of the photocurrent signal in response to UV radiation at 365 nm, as previously reported, results from excitation of carriers across the SiC bandgap. At lower photon energies (longer wavelengths), the log-scale plot reveals a weak sub-bandgap response extending out to ~520 nm for both devices tested in graphene emitter mode. This response is not seen in graphene collector mode but may lie beneath the detection limit of $\sim 10^{-6}$ A/W. Notably, the presence of the 4SSF does not appear to strongly perturb the action spectrum in graphene emitter mode, despite its prominence in SPCM images. We emphasize that spot illumination was used in SPCM while wide-area illumination at much lower power density is used to measure the action spectrum. The differing relative contribution of the SF under the two conditions could be related to differing saturation rates of responsivity vs. power between the SF and surrounding active region. In graphene collector mode, a slightly elevated above-bandgap responsivity is seen in the action spectrum of the device with SF. The sub-bandgap responsivity could not be compared as it falls below the detection limit for both devices due to the absence of significant bipolar gain in this mode.

From the action spectrum, it is possible to extract additional information on the band-edge characteristics in the active layer of the device. In an indirect bandgap semiconductor, the absorption coefficient varies approximately linearly with the square of the photon energy above the band edge: $\alpha_{\text{abs}} = k(E_\lambda - E_g)^2$, where k is a constant.

Accordingly a plot of $\alpha_{abs}^{½}$ vs. E_λ should give a straight line.[93] This property can be used to estimate the band edge energy from the measured responsivity R by taking into account the amount of light absorbed by a layer of thickness W, and a gain g that is taken to be independent of photon energy: $R = g\,R_b = g\,\frac{(1-e^{-\alpha_{abs}W})}{E_\lambda}$. This equation can be re-arranged to find: $\alpha_{abs}W = -\ln\left(1-\frac{R\,E_\lambda}{g}\right)$, so that $\left[-\ln\left(1-\frac{R\,E_\lambda}{g}\right)\right]^{1/2} = \left(\frac{k}{W}\right)^{1/2}\left(E_\lambda - E_g\right)$.

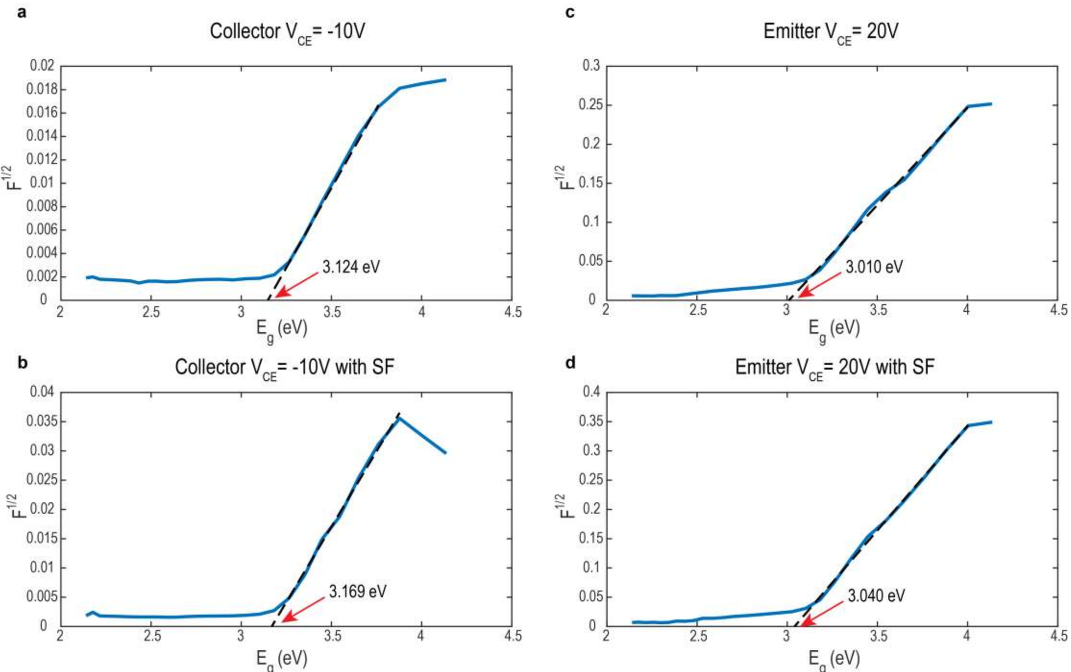

Figure 3.10. (a,b) Photocurrent absorption function ($F^{1/2}$) vs. optical bandgap (E_g) at V_{CE}=−10V for a device without and with the presence of a stacking fault, respectively. (c,d) $F^{1/2}$ vs. optical bandgap at V_{CE}=+20V for a device without and with the presence of a stacking fault, respectively. Dashed lines indicate linear fits, where the energy-intercept indicates the effective indirect bandgap of the absorbing material within the device. Copyright 2018 IOP Publishing.

A plot of the left-hand side vs. E_λ is expected to yield a straight line that should allow the band gap to be read off by extrapolating the data to the x intercept. A challenge is that the true gain g is not necessarily known independently, and it may be diminished from its

DC value in an AC lock-in measurement. Accordingly, a nominal gain g' can be introduced to define a value F based on the observed responsivity: $F = -\ln\left(1 - \frac{RE_\lambda}{g'}\right)$. Nonetheless, we see that in the limit of low light absorption near the band edge, ($\alpha_{\text{abs}}W \ll 1$), linear approximations for $\alpha_{\text{abs}}W$ and F are valid and they will differ by constant factor: $\alpha_{\text{abs}}W = -\ln\left(1 - \frac{R\,E_\lambda}{g}\right) \approx \frac{RE_\lambda}{g} \approx F\frac{g'}{g}$. As a result, a plot of $F^{½}$ vs. E_λ should approximate a straight line even if an inaccurate value of g' is selected. In our analysis of the effective optical bandgap (**Figure 3.10**), we have used $g' = 1$.

Figure 3.10 displays $F^{½}$ vs. photon energy for each device in graphene emitter and graphene collector modes. Notably, linear fits to the above-bandgap portions of the graphene collector mode plots reveal intercepts close to 3.2 eV for both devices, representative of the band gap of 4H-SiC. However, fits to the graphene emitter mode responses show a slightly smaller effective bandgap, just over 3.0 eV (410 nm). To explain this discrepancy, we first note that the two measurements are most sensitive to light absorption at different depths within the device. In graphene collector mode, we expect photocurrent generation near the surface. In graphene emitter mode, base current generation is expected to be localized to the collector *p-n* junction between the epilayer and substrate. Since illumination is provided from the top (graphene side), the light that reaches the base-collector junction in this mode has been filtered by absorption in the near-surface portion of the epilayer. This could result in an ultraviolet response that rises less rapidly with energy and could create the appearance of a smaller band gap. However, such internal filtering is expected to attenuate the incident light by only 21% at 365 nm based on the published absorption coefficient for 4H-SiC,[93] suggesting that additional factors may play a role.

The sub-bandgap tail visible in the graphene emitter mode signals can be considered in the context of photoluminescence results on similar 4H-SiC epilayers (without graphene), which showed emission at ~515 nm attributed to DAP recombination.[87,88] This indicates that photons at 444 nm have sufficient energy to excite localized DAP states. The action spectrum and SPCM results are consistent with excitation of DAPs, followed by thermal and/or field-assisted dissociation to yield free carriers, as the source of the sub-bandgap response and the limiting factor in the VRR in the devices studied to date. In contrast, we note that the observed behavior is inconsistent with internal photoemission at the EG/p-SiC junction. Firstly, based on the band alignment, internal photoemission would be expected to cut in at 2.7 eV or ~460 nm, the energy required to transfer a hole from graphene to the SiC valence band. Secondly, the gain is small in graphene-collector mode, indicating that holes excited across the EG/SiC junction are not efficient in providing a base current. In the PL results, DAP emission was found to scale with boron content.[87,88] This offers a potential route to improvement in the VRR. In particular, in site-competition epitaxy, boron, the characteristic acceptor impurity, is crowded out by growing SiC at a low C/Si ratio, leading to low-B epilayers that may show better VRR.[99] Another approach is through the use of TaC coated reactor furniture, where the free Ta in the coatings acts as a getter for boron.[100]

3.8. Carrier transport characteristics of EG/SiC device from SPCM and the origins of photocurrent enhancement from an 8H- stacking fault

The scanning photocurrent images can be used to examine carrier transport length scales in the SEPT devices. In particular, if we interpret the ~10 μm decay length of photocurrent with distance outside the edge of the graphene electrode (**Figure 3.3d**) as

the characteristic distance L_n for lateral electron diffusion near the EG/p-SiC interface, a lifetime $\tau_n \approx 50$ ns is obtained based on the reported electron mobility ~900 cm^2/V-s for 4H-SiC at 300 K.[101] Considering recombination to be dominated by a single interface indicates a surface recombination velocity S up to $W_B/\tau_n \sim 10^5$ cm/s. Such recombination velocities have been reported for SiC p/n^+ epilayers[102], though the larger gain and slower roll-off in graphene emitter mode indicates a dominant role of the EG/p-SiC interface in the present case. We note that surface state densities at the EG/SiC interface can be modulated through chemical treatments, such as H-intercalation.[90,103–106]

We now briefly consider the mechanism by which an 8H- stacking fault might lead to local enhancement of the sub-bandgap photocurrent. The reported bandgap for 8H-SiC is 2.86 eV (435 nm),[107] with most of the offset with 4H- predicted to fall in the conduction band.[86] However, reports on 3SSF and 4SSF defects have found PL emission at 2.58 eV and 2.70 eV respectively.[97] As such, in either case the 444 nm excitation light used in SPCM falls close to the band edge and could lead to significantly enhanced excitation on the defect compared to elsewhere. A simple estimate of the photocurrent that might be expected from such a defect, obtained by considering 2.70 eV to be the 4SSF band gap energy and using the same takeoff of α_{abs} with respect to energy that is found for 4H-SiC, predicts $\alpha_{abs} \approx 20$ cm^{-1} at 444 nm (2.80 eV),[93] giving base responsivity $R_b \approx \alpha_{abs} W/E_{ph} \approx 1.4\times10^{-6}$ A/W for W=2 nm. This value is small compared to the 5.6×10^{-5} A/W we detected for DAP absorption in the absence of the SF and is exceeded by the DC spot photocurrent measurements recorded on the defect in graphene collector mode, suggesting that an improved model of light absorption and/or elevated bipolar gain in the presence of such defects is necessary. Indeed, the maximum graphene-collector mode

photocurrent on the SF ($\approx 10^{-4}$ A/W, **Figure 3.8**) exceeds R_b for DAP absorption in the full base width as established in emitter-mode measurements on the SF-free device.

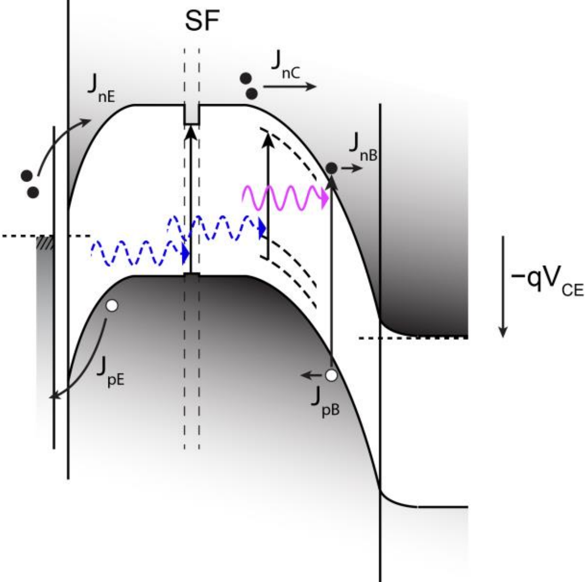

Figure 3.11. Band structure of the device in graphene emitter mode showing visible (dotted blue arrows) and UV (solid violet arrow) absorption mechanisms. Visible light can be absorbed by stacking faults (SF) that shrink the bandgap, allowing longer wavelengths of light to be absorbed. Donor-acceptor pairs (DAP) create sub-bandgap states (dotted black lines) that also absorb visible light. UV absorption can also occur at SFs or DAP states, alongside bandgap absorption. Copyright 2018 IOP Publishing.

Figure 3.11 shows the band diagram and sub-bandgap excitation processes that we have identified in the SEPT devices studied here. A small and diffuse contribution arises from DAPs that occur throughout the base region but are most effective in generating band-edge carriers in depletion regions. In contrast, in considering the SF contribution, we note that the depth of the SF varies with position in the device studied in **Figure 3.3** according to the 4° miscut, and yet a photocurrent signal is observed along its length in both operating modes, indicating some photocurrent generation occurs from the defect even when it does not locally lie within the base-collector depletion region. The low gain in graphene collector mode was attributed to a high surface recombination velocity, *S*, but

the SF will introduce excitation deeper within the structure that yields base current and enables gain. Indeed, an elevated total photocurrent with voltage dependence characteristic of bipolar gain is seen for excitation on the defect in graphene collector mode as shown in **Figure 3.7c**. Overall, SEPT device operation on the basis of electron injection at the EG/*p*-Si Schottky emitter contact is confirmed, to the exclusion of simple photoconductive gain, from the strongly asymmetric photocurrent response with respect to bias direction.

3.9. Summary and future work

As has been demonstrated here, the presence of DAP absorption and stacking faults, discovered by SPCM, can alter the visible rejection ratio. The pairing of 4H- and 8H- SiC polytypes results in a quasi-type-II heteropolytype junction (**Figure 3.11**). We note that by changing the polytypes forming such junctions, the conduction band offset can be controlled, leading to controllable quantum well depths.[86] These types of heterostructures have been shown to trap two-dimensional electron gases (2DEG) and two-dimensional hole gases (2DHG) in 3C-/4H- and 3C-/6H-SiC heterojunctions on the carbon and silicon faces, respectively.[108–110] Similar heterostructures based on III-V materials, such as GaN/AlGaN, exhibit suitable performance for high frequency and high power applications through the use of polarization doped high-electron mobility transistors (HEMTs).[111,112] Additionally, polytype heterojunctions that result in reproducible quantum wells could potentially be used as quantum well infrared photodetectors (QWIPs). By tuning the intersubband transition energy, the detection wavelength can be changed. This has been well documented, studied, and commercialized using III-V semiconductors.[113] SiC has been shown to have very minimal thermal expansion of the

lattice in the growth of different polytypes.[114] This small lattice difference opens an avenue for heteropolytype structures formed by a sudden, unstrained change in crystal structure or stacking, instead of the traditional method of abrupt compositional change, as used in GaAs/AlGaAs.

In summary, scanning photocurrent microscopy is a valuable tool in detection of polytypes in SiC-based transistors. Further inspection of I-V characteristics and the device action spectrum indicates the visible rejection ratio of this UV phototransistor is estimated to be on the order of 10^3. Control of quantum wells produced through polytype heterojuctions could lead to new applications for SiC, including quantum well photodetectors. This shows promise that the evolution of polytypes in SEPTs do not compromise its role as a UV photodetector and open these structures up to new applications. Additionally, control of these defects will remain an important and interesting metric in the performance of SiC-based power devices. The spatially-resolved polytype heterojuction revealed by sub-bandgap SPCM confirms the value of this approach in analyzing the electronic properties of such junctions.

3.10. Methods and materials

3.10.1 SPCM and current-voltage characteristics.

A home-built microscope with a motion-controlled stage was used for simultaneous reflection imaging and photocurrent mapping. A diode laser (λ = 444 nm) is mechanically chopped (~287 Hz) and focused to a diffraction-limited spot through a 20x objective lens (NA = 0.42, Mitutoyo Corporation). At each point the reflected signal was recorded for imaging by a lock-in amplifier (Ametek 7230), and the photocurrent was recorded by a pre-amplifier (DL Instruments 1211) and lock-in amplifier combination (SRS SR830). A

Keithley 2636A sourcemeter was used to apply voltage, as well as measure spot current-voltage characteristics. Reflected and photocurrent maps were plotted and analyzed using MATLAB. All images were measured at a 2 μm step size.

3.10.2 Action spectrum.

Collimated, wide area illumination was produced from a monochromator paired with a xenon lamp at 10 nm wavelength intervals. The excitation light was then mechanically chopped at ~287 Hz and directed onto the SEPT device to induce a photocurrent. The photocurrent was then measured using a lock-in amplifier (SRS SR830). The photon flux was measured with a calibrated Si diode and was multiplied by the active SEPT device area to obtain the incident optical power, by which responsivity was calculated from the measured photocurrent.

CHAPTER 4

ULTRAVIOLET AND PHASE-SENSITIVE PHOTOCURRENT MAPPING REVEALS LARGE VISIBLE REJECTION RATIO AND NON-LOCAL CURRENT GENERATION IN EPITAXIAL GRAPHENE/SIC BIPOLAR PHOTOTRANSISTORS[*†]

4.1. Introduction

Recently, there has been interest in the epitaxial graphene(EG)/SiC material system due to the tunable native Schottky junction[92] and potential for SiC integrated circuit manufacturing on 6-in. wafers. UV detection has been demonstrated in bipolar phototransistors featuring a transparent EG emitter grown on a *p*-SiC base epilayer on *n*-type SiC substrates. EG is a UV transparent material, which enables large area windows for high responsivity UV-detection. EG/SiC based UV detectors with improved responsivities were demonstrated by reducing the reflection/absorption losses at the detector surface.[115] The Schottky-emitter bipolar phototransistor (SEPT) structure reported in Chapter 3 showed a high responsivity of up to 7 A/W and bipolar gain of 113 at 365 nm in Schottky emitter mode due to efficient minority carrier injection from EG into the carefully prepared *p*-type SiC Schottky barrier.[85,116] Minority carrier injection, normally a minimal contribution in Schottky junctions, is efficient at EG/*p*-SiC junction because of high electron mobility, large barrier for holes, and very large recombination velocity at the SiC *p*-*n* junction leading to large diffusion current for electrons through

[*] Reprinted with permission from Chava, V. S. N.; Barker, B. G.; Balachandran, A.; Khan, A.; Simin, G.; Greytak, A. B.; Chandrashekhar, M. V. S. *Appl. Phys. Lett.* **2017**, *111* (24), 243504. https://doi.org/10.1063/1.5009003 with permission of AIP Publishing.
[†] (in preparation) Barker, B. G.; Chava, V. S. N.; Balachandran, A.; Khan, A.; Simin, G.; Chandrashekhar, M. V. S; Greytak, A. B. **2018**

the base. However, this device suffered from a large dark current due to lack of base/collector junction mesa isolation and poor visible rejection <10^2 at 400 nm (~10^3 at 444 nm) in Schottky emitter mode. Moreover, this device did not show appreciable gain in Schottky collector mode.[116] For detection applications, these issues must be resolved.

Here, I used scanning photocurrent microscopy (SPCM) with sub-bandgap excitation (444 nm) and above-bandgap (370 nm) illumination to map the spatial extent of the photocurrent response and to examine the working principles of the device under both types of illumination. By interpreting the spatial photocurrent response, we have proposed a working model of the excited carriers in this device, in both Schottky emitter and Schottky collector modes, under 444 nm and 370 nm light.

4.2. Device properties

In this work, we study a bipolar junction transistor (BJT) device similar to the previously reported device in Chapter 3[85,116] having an EG/*p*-SiC/n^+-SiC structure with a thinner base (12.8 μm) to improve the base transit factor and hence collection of the minority carriers injected by bipolar action.[85] EG was grown on SiC using a homoepitaxy-compatible SiF_4 gas precursor.[117] This EG growth method allows for accelerated growth of EG due to being more thermodynamically favorable, allowing for a wider range of EG thicknesses and quicker device preparation.[117] **Figures 4.1a** and **4.1b** schematically represents the device architecture of the previous device and the device discussed here.

For phototransistor device fabrication, the 12.8 μm thick *p*-SiC base epilayer is grown on an 8°offcut n^+-4H-SiC (0001) substrate by a CVD reactor. The resultant doping of the epilayer, due to site-competition epitaxy,[99] was found to be *p*-type 3.7×10^{14} cm^{-3} by the

Hg-probe capacitance-voltage (C-V) measurement. This thickness was based on previous work, where a diffusion length of ~10 μm was measured in the 30 μm base.[85,116] Thus, to improve the base transit factor and hence the current gain, a thinner layer was used, although this always comes at the expense of lower light absorption for long wavelengths (~30 μm for λ = 365 nm[85,116]). To achieve reasonable absorption in the range of 250–400 nm,[118] while maintaining adequate current gain, the 10 μm base thickness range was chosen, with the resultant 12.8 μm base obtained for our standard 30 min growth. The thickness of the EG is estimated to be ~15 monolayers. Circular graphene regions of diameter ~250 μm are defined for the device, using photolithography followed by O_2 plasma reactive-ion etching (RIE).

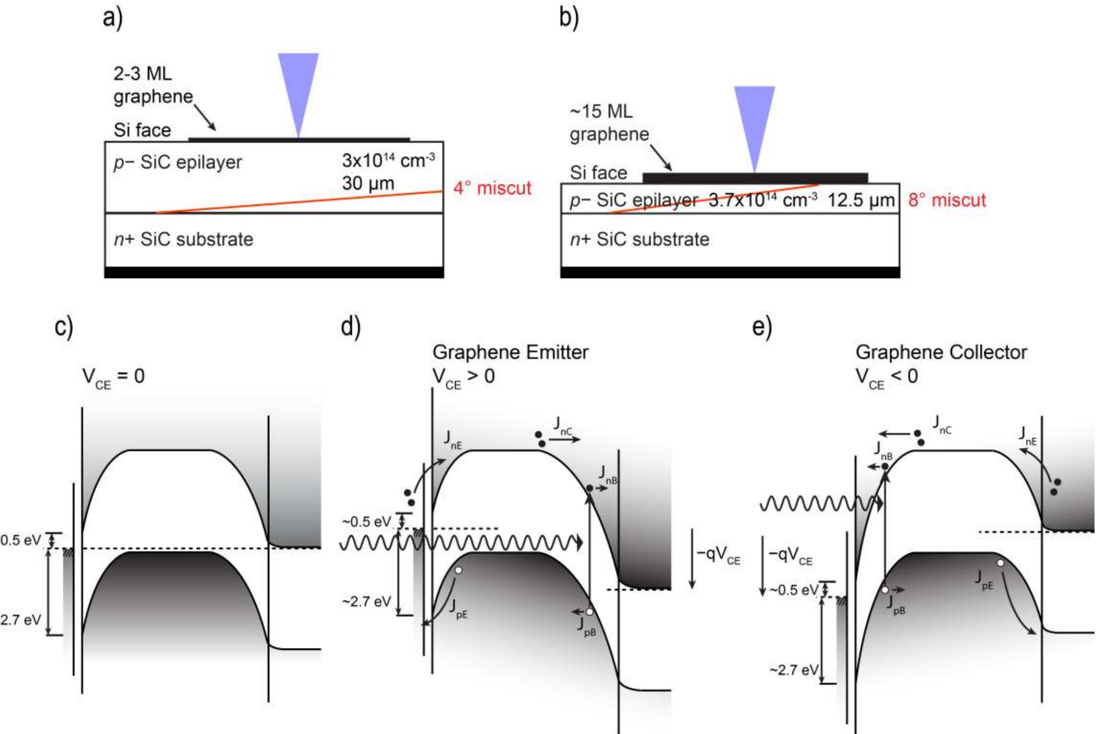

Figure 4.1. a) Previous SEPT device as described in Chapter 3, featuring a 30 μm base epilayer and 2-3 ML of EG. b) Device under study in this work, featuring a 12.8 μm base epilayer and ~15 ML of EG. c) Band structure of the device at short-circuit. d) Band structure of the device in Schottky emitter mode ($V_{CE} > 0$). e) Band structure of the device in Schottky collector mode ($V_{CE} > 0$).

Under operation, the graphene film is contacted directly by a tungsten probe. The voltage between the substrate (contacted through the bottom side) and probe is controlled to bias the device. A potential barrier of ~0.8 eV is reported for EG/*n*-SiC[119] (higher than the 0.5 eV barrier height reported for thermally grown EG/SiC junctions[90,92]) and a high barrier of ~2.7 eV for p-SiC on the SiC substrate (0001) surface. The device is operated in two different modes according the bias supplied, which are shown in **Figures 4.1c**, **4.1d**, and **4.1e**. When the EG/*p*-SiC junction is forward biased and the *p*-SiC/n^+-SiC junction is reversed biased, the graphene acts as the emitter and the substrate as the collector − this defines "Schottky emitter" mode (SE), with $V_{CE} > 0$. When the *p*-SiC/n^+-SiC junction is forward biased and the EG/*p*-SiC junction is reversed biased, the graphene acts as the collector and the substrate as the emitter − this defines "Schottky collector" mode (SC), with $V_{CE} < 0$. To avoid confusion, we will use negative values of V_{CE} to denote measurements in SC mode.

4.3. Initial investigation of the device

4.3.1 Current-voltage characteristics

Initially, the current-voltage characteristics of the device are measured in the dark and under light in both SC (**Figure 4.2a**) and SE (**Figure 4.2b**) modes using a monochromatic light source (10 nm bandpass), from which the action spectra are reconstructed. Dark currents of 230 pA and 670 nA are observed in SC and SE modes at 20 V. The significantly larger dark current in the SE mode is due to the lack of mesa isolation at the 10 μm deep backside SiC *p-n* junction, which is 1 cm^2, compared to the ~4.9×10^{-4} cm^2 area of the graphene/SiC Schottky top junction, leading to a corresponding increase in the leakage area. However, the dark current in the SE-mode

devices, 670 nA, was still 3 orders of magnitude lower than 100 μA observed in our previous devices.[85] We attribute this decrease to the significant optimization of our SiC epitaxy which has led to defect reduction in our epilayers.[119–121] Mesa-isolation of the base-collector SiC *p-n* junction should significantly reduce the dark current in SE mode to values comparable to SiC *p-n* diodes, which are among the lowest of any wide bandgap UV detectors.[122]

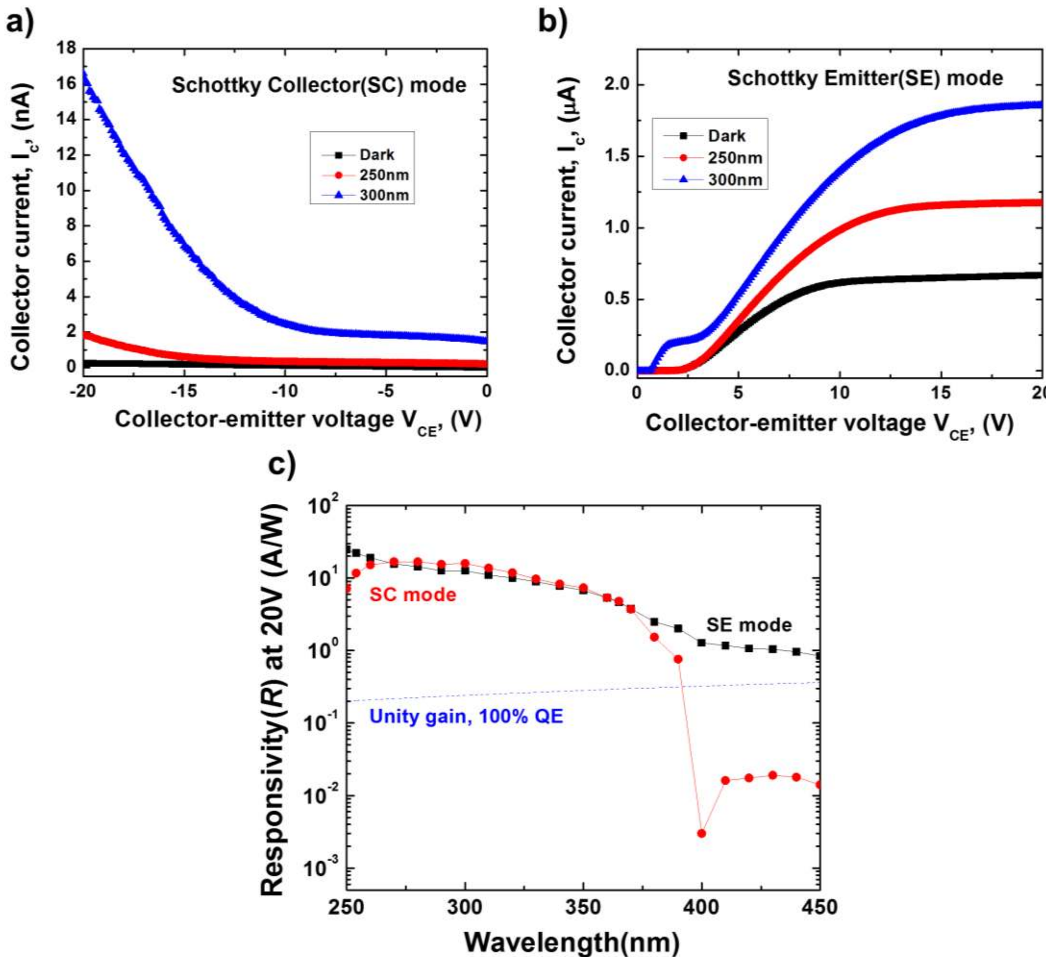

Figure 4.2. Experimentally measured dark and light current-voltage characteristics in SE (a) and SC (b) modes. c) A plot for the comparison of spectral responsivity of the phototransistor device in SE and SC modes of operation at V_{CE} = 20 V from 250 to 450 nm. Copyright AIP Publishing.

In SE mode, the current increases starting at $V_{CE} = 2$ V, in agreement with the 2.4 eV *p* EG/SiC Schottky barrier estimated in **Figure 4.1d**. A small hump is seen near ~0.7 V, which we attribute to the presence of a Schottky barrier height from the edge, in addition to the larger one from the bulk. As the emitter-base junction turns on, the influence of the parasitic smaller barrier is eventually overwhelmed by the bulk owing to the much larger area associated with the higher barrier. This could be due to independent contributions from bulk and periphery of the graphene contact.

In SC mode, bipolar behavior is seen until V_{CE} ~ -10 V, beyond which the photocurrent increases sharply due to avalanche effects from the electric field concentration at the reverse-biased EG/SiC Schottky barrier periphery.[123] In SE mode, there is no periphery due to the lack of mesa-isolation, so avalanche breakdown at the device periphery is not expected.

4.3.2. Responsivity and gain

Figure 4.2c shows the responsivity (*R*) of the device versus wavelength. *R*(λ) is defined as the ratio of the observed photocurrent (difference of current under illumination and in the dark) to the optical power incident on the device. The dependence of *R* on wavelength (λ) was measured under wide area illumination by comparison to a calibrated Si photodiode. To account for the difference in the collection area discussed above, the absolute responsivity, *R*, was calibrated to measurements performed at 365 nm with illumination through a microscope focused to an area < the device area. The *R*(λ) values are higher than expected from 100% quantum efficiency (dashed line in **Figure 4.2c**) for above bandgap (~390 nm for SiC) light illumination, indicating current gain in both SE and SC modes. A peak *R* (250 nm) = 25 A/W is observed in SE mode which corresponds

to current gain $g > 120$, as given by[124]: $R(\lambda) = \left({}^{\lambda\eta}/_{hc}\right) qg = \left({}^{\lambda(nm)}/_{1.24 \times 10^3}\right) g$, where R is the measured responsivity (in A/W), λ is the incident light wavelength, h is Planck's constant, c is the speed of light, and q is the electron charge, where we assume a quantum efficiency, η = 1, to estimate a lower bound on g in the final expression.

In SC mode, a peak R (270 nm) = 17 A/W is measured, corresponding to $g > 78$ although as discussed above, this is due to a combination of bipolar gain and avalanche gain from the device periphery at $V_{CE} = -20$ V. At $V_{CE} > -10$ V, avalanche gain from the periphery is effectively suppressed, and R is also reduced, leading to bipolar current gain, g ~10. In SC mode, the short absorption lengths in SiC (~1 μm at 270 nm) for short wavelength photons result in lower R due to the recombination of the photogenerated carriers at the EG/SiC Schottky collector junction.

4.3.3. Recombination velocity

In a long-base bipolar device, where we assume a minority carrier injection efficiency of ~1 and that g is limited by base transit, we estimate the recombination time, τ_{rec}, from[125]

$g \approx {}^{2D_n\tau_{rec}}/_{W_{QNR}{}^2}$, where W_{QNR} is the quasi-neutral region width at a given voltage from the difference in the base-width and the depletion region at the collector side, and $D_n = 23$ cm^2/Vs is the diffusivity of electrons in SiC.[126] This leads to τ_{rec} ~20 ns in both modes. In SC mode, the recombination velocity, S, at the EG/SiC interface is estimated from $W_{QNR}/\tau_{rec} \sim 10^5$ cm/s at $V_{CE} = -10$ V, which is in excellent agreement with that estimated for sub-bandgap illumination previously.[116]

4.3.4 Visible rejection

The UV-visible rejection ratio (VRR), *R* (270 nm)/*R* (400 nm), is better in SC mode ~5600 compared to ~12.3 in SE mode. We attribute the poor visible rejection in SE mode to absorption of sub-bandgap light by donor acceptor pairs (DAP)[116] present in the highly doped n^+-SiC substrate but not in the low-doped *p*-SiC, since the collection region in this mode spans the n^+-substrate unlike in SC mode. Our $R(\lambda)$ and visible rejection values compared well with those of other wide bandgap photodetectors.[122,127–131] We also note that our high responsivity is achieved at a relatively low bias voltage of 20V compared to > 100V for the avalanche photodiodes.[130]

4.3.5 Wide-area illumination versus small-area illumination

The results described above were determined under wide-area illumination using a monochromatic light source. The avalanche behavior seen in SC mode, should be a localized effect at the device edge, where the electric field is strongest. Additionally, localized measurements of the SEPT device using small-area illumination has been valuable in determining the sources and mechanisms of sub-bandgap response previously.[116] To compare with the wide-area illumination characteristics and to determine the effect of the new device design on sub- and above-bandgap excitation processes, SPCM images in both SE and SC modes are imaged and small-area excitation current-voltage measurements were performed.

4.4. Scanning photocurrent images in Schottky emitter mode

SPCM images in SE mode (V_{CE} = 20 V) are shown in **Figures 4.3a** and **4.3b**, under 444 nm and 370 nm light, respectively. In both images, there are present a small, but non-zero, photocurrent in the center of the graphene mesa, an enhanced photocurrent located

at the edge of the graphene mesa, a photocurrent signal (resembling a "halo") that decays as the excitation spot moves away from the graphene mesa, and the outline of the tungsten probe in the top right of each image. The enhanced photocurrent signal present directly underneath the tungsten probe in **Figure 4.3a** is due to absorption of scattering photons off the surface of the probe. The striking similarities between the photocurrent generation above- and sub-bandgap suggest that generated carriers experience similar band transport. The conduction at the edge of the mesa is thought to be enhanced photocurrent due to scattering at the graphene mesa edge, as well as possible increased

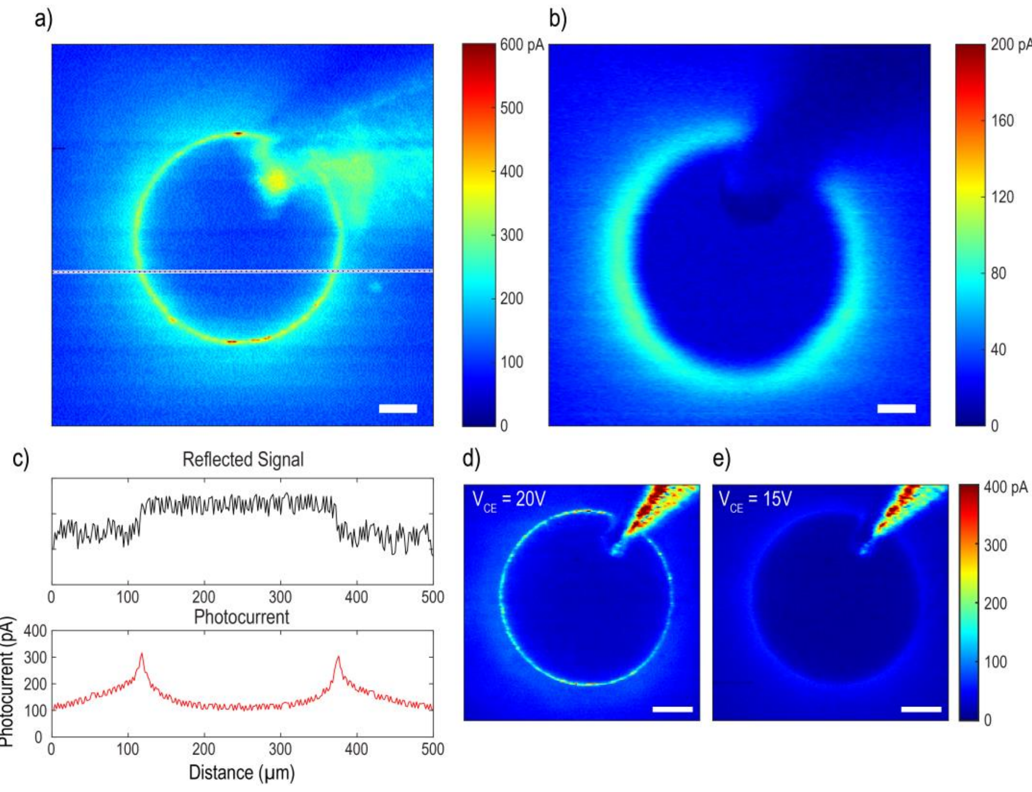

Figure 4.3. a) SPCM map of a device in SE mode (V_{CE} = 20 V) under 1.120 mW of 444 nm light. b) SPCM map of the same device in SE mode (V_{CE} = 20 V) under 32 nW of 370 nm light. c) Profile intensities of the device shown in a) measured along the indicated dotted line. d), e) SPCM maps of a SEPT device in SE mode at varying voltages, V_{CE} under 177 μW of 444 nm light. All resultant signals decrease in intensity versus voltage. All SPCM maps are recorded at an excitation frequency of 287 Hz. All scale bars are 50 μm.

current due to avalanche effects.[132,133] To achieve a photocurrent signal, generated electrons must be collected through the n^+-SiC substrate. To achieve bipolar gain, electrons must emit from the graphene emitter into the base *p*-SiC epilayer and then be collected. The presence of holes at the emitter-base junction promotes emission of electrons. Therefore, the decaying photocurrent away from the edge is indicative of a characteristic roll-off length for majority carriers (holes) generated in the *p*-SiC base. Within this length, they may travel to the emitter-base junction to lower the barrier for minority carrier injection. **Figure 4.3c** shows a photocurrent profile of the dotted line shown in **Figure 4.3a**. The exponential decay away from the edge suggests length of ~150 μm.

A direct comparison of two SE SPCM maps of a different device on the same chip are shown in **Figure 4.3d** and **Figure 4.3e** at V_{CE} = 15 V and V_{CE} = 20 V, respectively. As the voltage increases, so does the photocurrent enhancement around the edge (suggesting possible avalanche gain) and the photocurrent signal from the resulting "halo" surrounding the graphene mesa. The angle of the tungsten probe used to contact the device is sharp and the photocurrent signal from scattering light into the *p*-SiC base is relatively large as light is scattered over a large area of the "halo".

4.5. Scanning photocurrent images in Schottky collector mode

SPCM images in SC mode (V_{CE} = -20 V) are shown in **Figures 4.4a** under 444 nm excitation and in **Figure 4.4c** for 370 nm light. In all both images, a photocurrent is observed in the center of the graphene mesa that quickly decays to zero as the excitation spot moves off the graphene mesa. A dark shadow of the tungsten probe is present in the top right of each image. Similar to SE mode, photocurrent generation above- and sub-

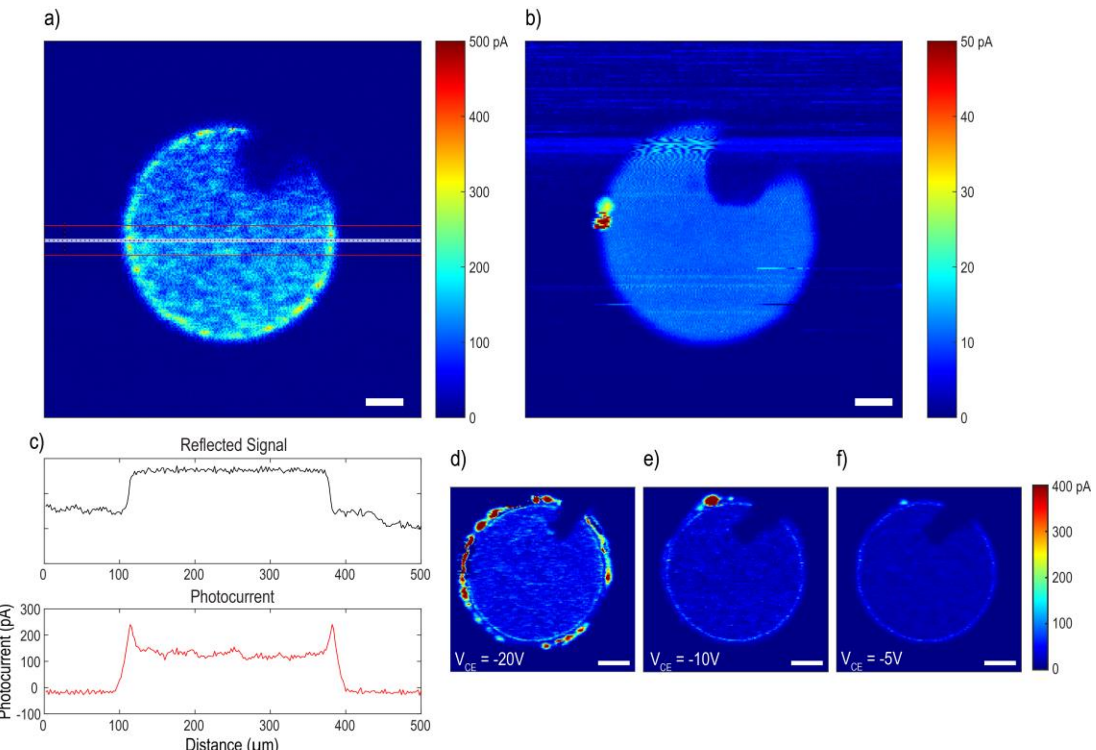

Figure 4.4. a) SPCM map of a device in SC mode (V_{CE} = -20 V) under 1.120 mW of 444 nm light. b) SPCM map of the same device in SC mode (V_{CE} = -20 V) under 32 nW of 370 nm light. c) Profile intensities of the device shown in a) measured along the indicated dotted line and integrated over a profile width indicated by the red box. d), e) SPCM maps of a SEPT device in SC mode at varying voltages, V_{CE} under 177 µW of 444 nm light. All resultant signals decrease in intensity versus voltage. As the magnitude of the voltage is reduced, the photocurrent spots outside of the device due to avalanche disappear. All SPCM maps are recorded at an excitation frequency of 287 Hz. All scale bars are 50 µm.

bandgap are extremely similar, suggesting that generated carriers experience similar band transport. The sharp decaying photocurrent away from the edge is indicative of a diffusion length for minority carriers (electrons) generated in the *p*-SiC base that are collected at the graphene contact. To be collected at the graphene mesa, electrons must be generated near the graphene mesa or they are likely to recombine with the abundant number of holes in the *p*-SiC base. **Figure 4.4c** shows a photocurrent profile of the dotted line shown in **Figure 4.4a**. The exponential decay away from the edge suggests a

minority carrier diffusion length of <7μm, which approaches the resolution of the microscope (inferred from the reflected signal profile).

Figures 4.4d, **4.4e**, and **4.4f** show SC SPCM maps at V_{CE} = -5 V, V_{CE} = -10 V, and V_{CE} = -20 V. As previously seen in the current-voltage response for SC mode in **Figure 4.2**, avalanche gain is observed at V_{CE} < -10 V. The sharp spots of large photocurrent generation slightly off the edge of the graphene mesa are the result of avalanche effects that are sometimes present in SC mode. These spots are clearly voltage dependent as large number of them appear at V_{CE} = -20 V compared to $V_{CE} \geq$ -10 V. The spots are similar to previously reported photocurrent signals generated from edge breakdown in SiC avalanche photodiodes.[132,133]

4.6. Small area excitation current-voltage characteristics

4.6.1 Current-voltage characteristics

The previous responsivity values were measured with wide-area illumination. To better compare the response of the device with the observed SPCM maps, current-voltage curves were taken with a small-area excitation spot located on the graphene mesa using the same illumination setup as the SPCM experiments.

Current-voltage characteristics under 444 nm and 370 nm light in SE mode are shown in **Figure 4.5a**. As seen previously, the SEPT device displays a large dark current at positive V_{CE} (SE mode) due to lack of mesa isolation. The photocurrent-voltage curves are shown in **Figure 4.5b**. The photocurrent increases with increasing sub-bandgap illumination power, demonstrating a maximum responsivity of 6.47 × 10^{-4} A/W under 0.300 mW of 444 nm light. The responsivity decays sharply with increased laser power, similar to our previous devices.[85,116] In comparison, 32 nW of 370 nm above-bandgap

excitation leads to a responsivity of 3.88 A/W. While the illumination powers are not similar, the photocurrent generated is similar in magnitude and leads to a VRR of ~5990 in SE mode (370:444 nm). This value is much larger than the reported ~12.3 (270:400 nm) above for wide area illumination. This may be due to the large collection area of current for sub-bandgap illumination, which has been shown in the AC SPCM measurement to exist on the order of hundreds of μm away from the graphene mesa. By comparing the responsivities of the current from the SPCM maps under 444 nm and 370 nm light (**Figures 4.3a** and **4.3b**), a VRR of 6278 is calculated in SE mode – in agreement with the current-voltage measurements.

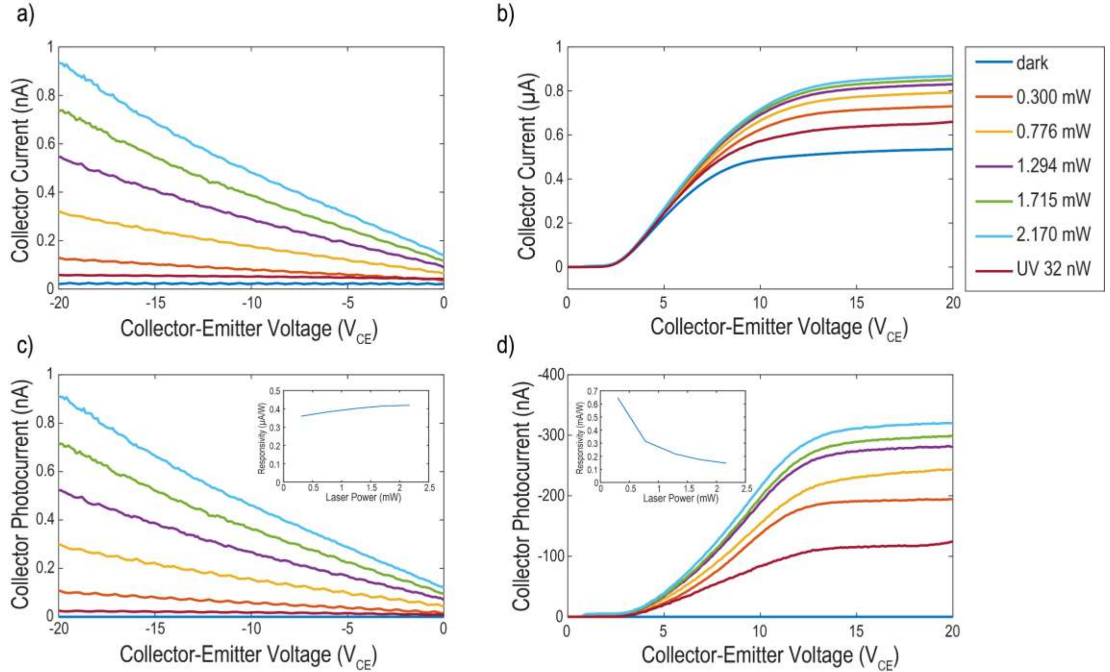

Figure 4.5. a) Current-voltage (I-V_{CE}) characteristics in the dark and under various 444 nm light intensities and 32 nW of 370 nm light in SC mode. b) Photocurrent-voltage (I-V_{CE}) characteristics under various 444 nm light intensities and 32 nW of 370 nm light in SC mode. c) Current-voltage (I-V_{CE}) characteristics in the dark and under various 444 nm light intensities and 32 nW of 370 nm light in SE mode. d) Photocurrent-voltage (I-V_{CE}) characteristics under various 444 nm light intensities and 32 nW of 370 nm light in SE mode.

The SEPT device displays little to no dark current in SC mode (**Figure 4.5c**). Photocurrent-voltage curves (**Figure 4.5d**) show an increasing photocurrent with increasing sub-bandgap illumination power, demonstrating a maximum responsivity of 4.49×10^{-7} A/W at 2.17 mW of 444 nm light. The photocurrent remains linear until V_{CE} = -10 V and show exponential behavior reminiscent of avalanche gain at $V_{CE} \leq$ -10 V. The increase in photocurrent responsivity is related to the avalanche gain. At V_{CE} = -10 V, the responsivity does not vary much with increasing laser power. In comparison, 32 nW of 370 nm above-bandgap excitation leads to a responsivity of 7.76×10^{-4} A/W, leading to a visible rejection ratio of ~1850 in SC mode (370:444 nm). By comparing the responsivities of the current from the SPCM maps under 444 nm and 370 nm light (**Figures 4.4a** and **4.4b**), a VRR of 1682 is calculated in SC mode – in agreement with the current-voltage measurements. This is smaller than the reported value of 5600 reported for 270:400 nm initially. This may be due to different comparison wavelengths, as well as possible wavelength dependence and area dependence of the avalanche gain present in these devices.

4.6.2 Calculation of gain

The large UV responsivity observed for the device is a direct consequence of the large bipolar gain g that is achieved in SE mode. Previously, g has been calculated on the basis of the observed photocurrent, and an estimate of the maximum base responsivity, R_b, that could be generated by light absorption within the entire base width W_B from the known absorption coefficient α_{abs} of 4H-SiC (80 cm^{-1} at 370 nm[93]) and the energy of 370 nm light in eV, E_{370}.[85,116] In the present device, such an analysis predicts a maximum base current responsivity, $R_b = {(1 - e^{-\alpha \cdot W_B})}/{E_{370}}$, of 0.0291 A/W. The observed

responsivity at 370 nm in SE mode was 3.88 A/W, indicating current gain of at least $g = 132$ for the present device in SE mode. This is comparable to the previously reported gain of > 120 for wide area illumination. For sub-bandgap excitation at 444 nm, the maximum responsivity in SE mode was 6.47×10^{-4} A/W. The 4H- polytype is nominally transparent at 444 nm (bandgap ~3.2 eV or 387 nm) and absorption at this wavelength is attributed to donor-acceptor pairs in the base epilayer that thermalize to the band edge.[116] Comparison of the observed responsivities can be used to assign a minimum absorption coefficient α_{abs} at 444 nm if g is considered to be independent of the photon energy: that is, that the transport process following visible excitation is fundamentally the same as following UV excitation. This notion is supported by the similarity of the SPCM images between UV and visible excitation (**Figures 4.3** and **4.4**). $\alpha_{\text{abs}} \approx {(R_b E_{444})}/{W}$ and $R_b = {R}/{(g+1)}$. The attributed absorption coefficient, $\alpha_{abs} \approx 0.0106\ \text{cm}^{-1}$, is much smaller than our previous estimate for a 30 μm 4H-SiC epilayer (~0.052 cm^{-1}).[116]

Using the same value of R_b compared to the responsivity of 444 nm light, the gain can be calculated for SC mode, $g = {R}/{R_B} - 1$. Using the maximum responsivity of 4.49×10^{-7} A/W, no gain is calculated in SC mode. Using the responsivity and base responsivity values for 370 nm illumination also leads to the calculation of no gain. The attribution of gain from the wide area responsivity measurements must have been due to enhanced avalanche effects, only present at smaller wavelengths, or due to other effects only present under wide area illumination.

4.7. Photocurrent mapping of neighboring floating devices

In SPCM maps of the graphene mesa in both SC and SE modes, a large enhancement of the photocurrent is seen at the edge of the device. Two possible reasons are due to

scattering of light at the edge of the mesa or avalanche breakdown at the edge of the mesa. If we map a neighboring unconnected device, we expect to only see a signal from the edge of that device if there is strong enough scattering to reflect the excitation light into the *p*-SiC base epilayer, which will generate electron-hole pairs close enough to the connected device to result in a photocurrent.

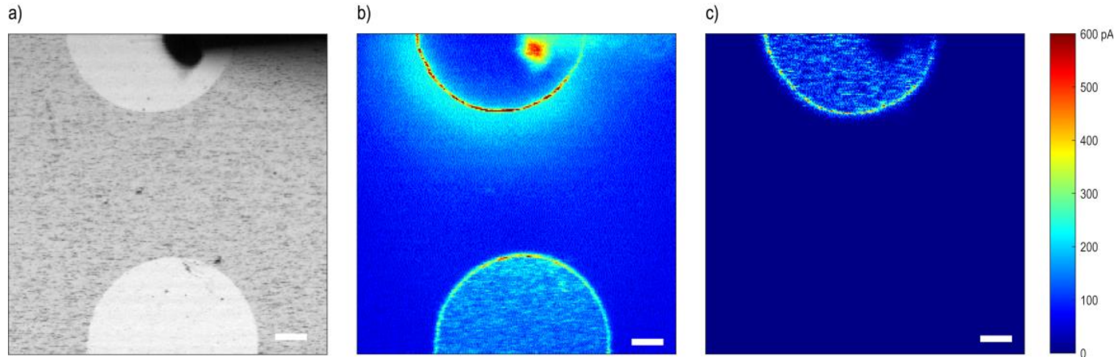

Figure 4.6. a) Reflected optical signal of two graphene mesas with a tungsten probe making electrical contact to the top device. b) SPCM image of the same area defined in a) where the top device is in SE mode (V_{CE} = 20 V) and the bottom device is left floating. The floating device has a large photocurrent signal that is similar to connected devices in SC mode. c) SPCM image of the same area defined in a) where the top device is in SC mode (V_{CE} = 20 V) and the bottom device is left floating. The floating device provides no localized photocurrent signal. All scale bars are 50 µm.

Figure 4.6a shows a reflected signal micrograph of half of a graphene mesa contacted with a tungsten probe and half of a neighboring graphene mesa, which is electrically floating. **Figures 4.6b** and **4.6c** show the resulting SPCM maps of the same area in SE mode (V_{CE} = 20 V) and SC mode (V_{CE} = -20 V), respectively. In SE mode, the connected device has the same photocurrent characteristics as before: a dark (non-zero) photocurrent in the center of the mesa, an enhanced signal due to scattering off the connected prove, an enhancement at the edge of the mesa, and a “halo” that decays in signal with distance. However, the neighboring unconnected device not only shows an

enhanced signal at the edge of the graphene mesa, but a uniform photocurrent signal inside the device area. The floating device looks nearly identical to the SPCM maps of a connected graphene mesa in SC mode. However, when the connected device is in SC mode, the neighboring device shows no signal.

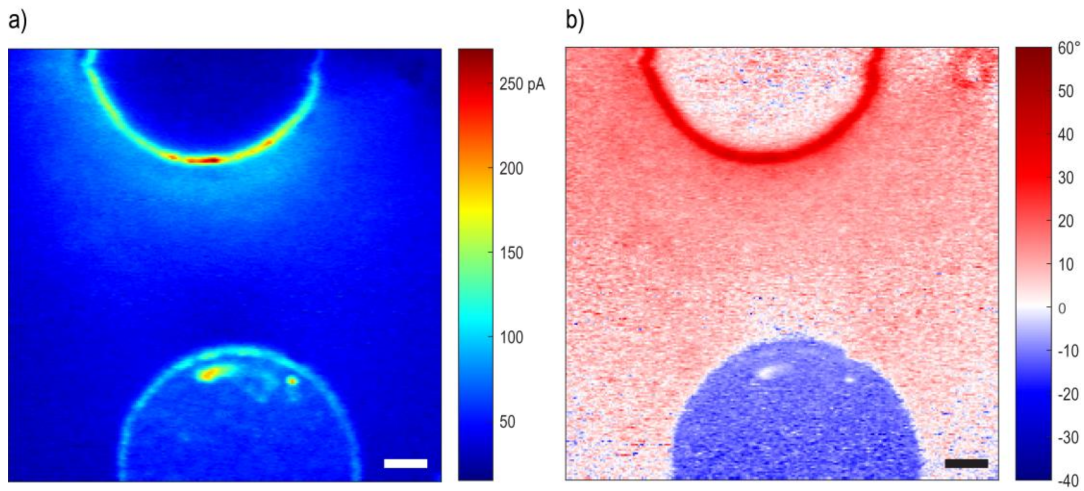

Figure 4.7. a) SPCM image of two graphene mesas with a tungsten probe making electrical contact to the top device. The top device is in SE mode (V_{CE} = 20 V) and the bottom device is left floating. The floating device has a large photocurrent signal that is similar to connected devices in SC mode. b) Phase map of the same area as the SPCM map in a). The phase is zeroed at the center of the top connected graphene mesa. All scale bars are 50 μm.

One possibility for this phenomenon is that the remote signal is due to surface conduction along the device. In this case, the remote device is essentially operating independently, but is linked to the connected emitter contact by some large resistance associated with surface conduction. Because of this, the expectation is that the remote signal would be biased in the same direction as the local device and would be in phase with the local signal. We note that the remote device does not seem to be biased in the same direction, as it seems to exhibit the same characteristics as SPCM maps in SC mode. Additionally, **Figure 4.7a** shows another photocurrent map of the same two

devices in SE mode, alongside the phase map (**Figure 4.7b**) of the lock-in signal, which has been zeroed inside the connected graphene device. The phase changes quite drastically, increasing by 40-50° at the edge of the connected device, and then inverting the phase to ~-15° on the unconnected, floating graphene mesa.

Another possibility is the devices are interacting capacitively. The remote device could act as a capacitance, permitting AC base current generation due to photovoltaic behavior at the unbiased EG/SiC Schottky junction. Resistance of the base and capacitance to the remote EG device and the collector (substrate) could lead to a phase shift at higher frequency with a roll-off at low frequency. This may explain why the remote SPCM signal has some characteristics of SC mode, as well as the roll-off of 150 μm measured before as an RC delay in SE mode. Additional work needs to be done to properly investigate and model this behavior.

4.8. AC versus DC characteristics

If separate devices on the same chip are interacting capacitively, there should be distinct differences between current measurements of AC and DC. To examine the roll-off in SE mode, which was previously measured to be ~150 μm at V_{CE} = 20 V and 287 Hz, the sub-bandgap photocurrent was measured as a function of distance away from the edge of a connected graphene mesa. **Figure 4.8a** shows photocurrent-voltage curves stepped by 50 μm starting from distance zero, which is centered directly on the edge of a graphene mesa. The photocurrent initially decreases, as expected, due to the enhanced signal at the graphene edge as seen from the SPCM maps. The photocurrent at 50, 100, and 150 μm is extremely similar. This is the same characteristic distance measured for roll-off in the SPCM maps (AC). At 250 μm and greater, the photocurrent decreases in a

linear fashion all the way to the last gathered data point at 700 µm away from the edge of the connected device. DC measurements show ~39% of the original photocurrent exists 700 µm away from the edge and after 250 µm the photocurrent decreases linearly at a rate of ~178 pA/µm. This suggests that photocurrent may still exist up to 1 mm away from the edge of a connected graphene mesa.

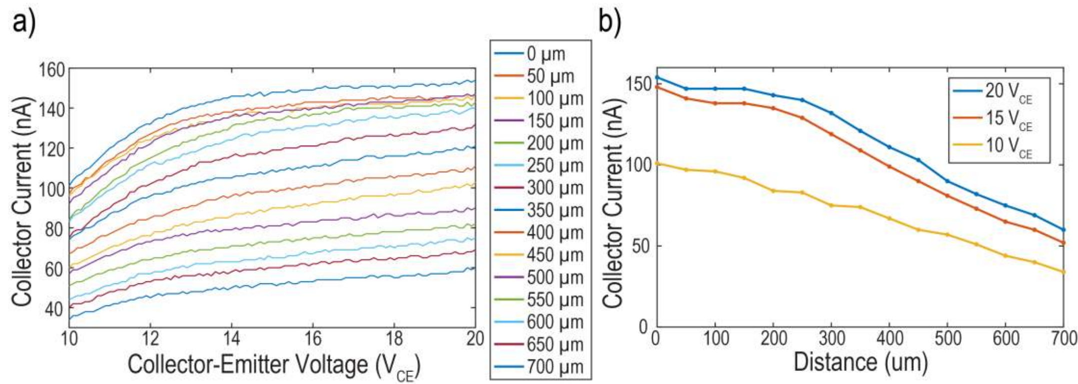

Figure 4.8. a) Photocurrent-voltage characteristics of a SEPT device in SE mode (V_{CE} > 0 V) with respect to distance under 0.300 mW of 444 nm light. b) Photocurrent at several voltages with respect to illumination at increasing distances away from the connected graphene mesa edge. The photocurrent initially decreases as the excitation spot is moved away from edge, stays roughly the same until 200 µm, and at distances greater than 250 µm the photocurrent decreases in a linear fashion.

4.9. Working hypothesis of device operation

Based on the SPCM images and spot current-voltage curves mentioned above, we propose a working model of carrier transport in a SEPT device. In SE mode (**Figure 4.9a**), bipolar gain depends on holes lowering the barrier at the emitter-base junction. In the case of an electron-hole pair being generated under the EG in the epilayer, the electrons traverse towards the n^+-SiC substrate. Holes must migrate to the emitter-base junction and lower the barrier for electrons to emit from the graphene into the epilayer, which may then travel to the substrate to be collected, creating gain. When an electron-hole pair is generated far from the EG/*p*-SiC interface, the holes must travel towards the

emitter-base junction to lower the barrier. This is estimated to be ~150 μm from the fitting of the photocurrent decay in **Figure 4.3c** but may be as long as 1 mm as determined by DC current-voltage characteristics. The frequency dependence and varying phase with distance in AC measurements suggests that the AC signal could be attenuated by an RC (resistance-capacitance) delay due to series resistance in the base, at long distances. Avalanche breakdown may be possible at the edge of the device if the electric field is strong enough, although we do not expect it. This may be the possible explanation of the large photocurrent signal at the edge of the device, but this may also be due to scattering. In each of these processes, electrons and holes can also recombine (noted by a star), which in turn limits the bipolar gain. The probability of this process depends on distance of the generated light away from the interface, as well as the epilayer thickness. We expect most electrons and holes to recombine when generated at distances of several hundreds of μm away from the EG/p-SiC interface, as well as some increase recombination near the interface.

In SC mode (**Figure 4.9b**), bipolar gain depends on the electrons' ability to travel from the emitter-base junction (n^+-SiC/*p*-SiC) to the base-collector junction (EG/*p*-SiC). In the case of an electron-hole pair being generated under the EG in the epilayer, electrons will inject into the graphene, while holes will remain in the epilayer. Excess holes create a charge imbalance, which can lead to emission of electrons from the n^+-SiC, which can then travel to the graphene to be collected, creating gain. When an electron-hole pair is generated far from the EG/*p*-SiC interface, the electrons must diffuse towards the EG/*p*-SiC junction to be collected. The distance at which this still creates gain is the diffusion length for electrons in the *p*-SiC epilayer. This is estimated to be <7μm from the fitting of

the photocurrent decay in **Figure 4.4c**. Large photocurrents are enhanced at the edge and sometimes extremely large photocurrent signals are seen just outside of the graphene mesa edge (**Figure 4.4f**), indicative of avalanche gain.[132,133] In each of these processes, electrons and holes can also recombine (noted by a star), which in turn limits the bipolar gain. Electrons traveling through the epilayer are likely to encounter many excess holes, increasing the probability of recombination. This limits the diffusion length and the bipolar gain and makes it unlikely that electron-hole pairs generated far away from the EG/*p*-SiC junction will be collected.

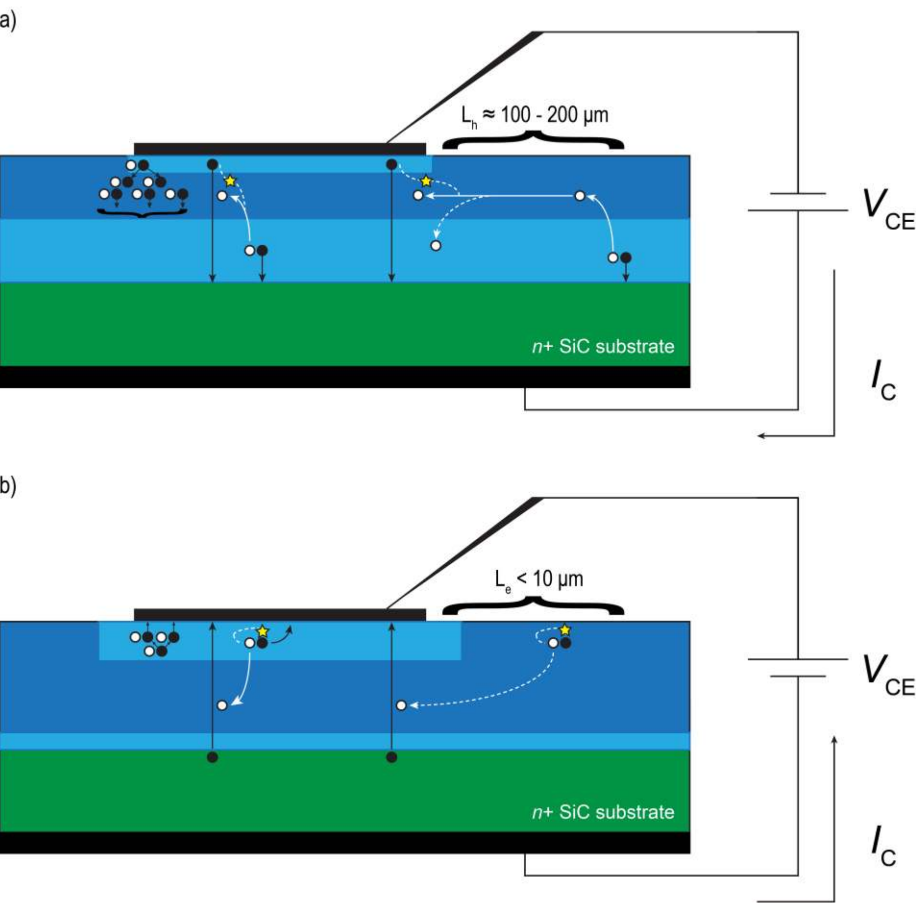

Figure 4.9. Working hypothesis of a SEPT device in SE mode, a), and SC mode, b), with respect to carrier generation at various locations on the device. Electrons are indicated by black circles, holes are indicated by white circles and recombination is indicated by yellow stars.

4.10. Summary and future work

In summary, a working hypothesis of device operation under different localized excitation has been achieved. In SE mode, the device exhibits bipolar gain of ~132, a visible rejection ratio of ~5990 (370:444 nm), and generated charges can be collected over a large area of the device. In SC mode, the device does not exhibit bipolar gain, a visible rejection ratio of ~1850 (370:444 nm), shows an extreme localization of photocurrent detection to the area of the graphene mesa, and at larger voltages exhibits avalanche gain.

In the future, the SiF_4 growth of different graphene layer thicknesses to fabricate SEPT devices should be investigated. Additional modeling to determine the signals present on unconnected devices, to compare device performance in AC and DC modes, and to determine the mysterious darker signal of the graphene mesa in the in SE SPCM maps is needed. Bipolar gain has still yet to be realized in SC mode consistently. Field-plate techniques can be used to suppress avalanche gain[123] or they can be exploited as in avalanche photodiodes.[134] The EG/Schottky barrier could be used in conjunction with deposited quantum dot layers to form photosensors in which charge transfer modulates conductivity or the barrier height of the EG layer.[135–138]

4.11. Methods and materials

4.10.1 Device fabrication

For the phototransistor device fabrication, the 12.8 μm thick *p*-SiC base epilayer is grown on an 8°offcut n^+-4H-SiC (0001) substrate by a CVD reactor using dichlorosilane (DCS) and propane in hydrogen ambient at 300 Torr and 1600°C at a C/Si ratio of 1.9,[139] giving a growth rate of ~26 μm/h for 30 minutes to produce the 12.8 μm thick film

determined by Fourier transform infrared reflectance (FTIR). The resultant doping of the epilayer, due to site-competition epitaxy,[99] was found to be *p*-type 3.7×10^{14} cm^{-3} by the Hg-probe capacitance-voltage (C-V) measurement. This thickness was based on previous work, where a diffusion length of ~10 μm was measured in the 30 μm base.[85,116] Thus, to improve the base transit factor and hence the current gain, a thinner layer was used, although this always comes at the expense of lower light absorption for long wavelengths (~30 μm for λ = 365 nm[85,116]). To achieve reasonable absorption in the range of 250–400 nm,[118] while maintaining adequate current gain, the 10 μm base thickness range was chosen, with the resultant 12.8 μm base obtained for our standard 30 min growth.

The EG top electrode layer is then grown on the SiC base at 1600 °C and 300 Torr, in the same reactor, using the SiF_4 precursor in Argon for 10 min using a chemically accelerated Si-removal process developed at our lab.[117] From FTIR and X-ray photoelectron spectroscopy,[140] the thickness of the EG is estimated to be ~15 monolayers for these growth conditions. Circular graphene regions of diameter ~250 μm are defined for the device, using photolithography followed by O_2 plasma reactive-ion etching (RIE).

4.10.2 SPCM and current-voltage characteristics

A home-built microscope with a motion-controlled stage was used for simultaneous reflection imaging and photocurrent mapping. A diode laser (λ = 444 nm) is mechanically chopped (~287 Hz) and focused to a diffraction-limited spot through a 20x objective lens (NA = 0.42, Mitutoyo Corporation). At each point the reflected signal was recorded for imaging by a lock-in amplifier (Ametek 7230), and the photocurrent was recorded by a pre-amplifier (DL Instruments 1211) and lock-in amplifier combination (SRS SR830). A Keithley 2636A sourcemeter was used to apply voltage, as well as measure spot current-

voltage characteristics. Reflected and photocurrent maps were plotted and analyzed using MATLAB. All images were measured at a 2 μm step size.

CHAPTER 5

PHOTOCURRENT STUDY OF CADMIUM SULFIDE NANOWIRES AND LEAD SULFIDE QUANTUM DOTS

5.1. Introduction

Semiconductor nanostructures are promising candidates for active components of optoelectronic nanoscale devices. Over the past few decades, several fabrication routes for multiple types of nanowires (NWs) and quantum dots (QDs) have been developed, allowing for controlled morphologies and optical properties. The breadth of composition, size, and structure allow semiconductor nanostructure-based devices to cover a large spectral range and flexible modification to suit specific needs in optoelectronic devices.

5.1.2 Nanowires

Semiconductor nanowires have been widely studied due to their unique properties such as high aspect ratio, high carrier mobility, and high surface-to-volume ratio. These properties make them suitable in many electronic devices, such as nanosensors, photovoltaics and photodetectors. Due to their large surface-to-volume ratio the surface plays an extremely important role in the optical and electronic properties of the nanowire. Surface traps and defects can lead to mid-gap trap states, decreasing the efficiency of charge separation.

Nanowires possess potential for photoconductive applications due to their tunable geometric effects, high carrier mobility compared to thin films, and inexpensive low-

temperature processing. Other advantages include decreased net reflectance, increased junction area, and reduced material use.[37]

5.1.3 Quantum Dots

Colloidal quantum dots (QDs) are semiconductor nanoparticles in solution phase that can be deposited to create films by low-cost, facile processing methods. Due to their strong quantum confinement, they exhibit unique optical properties such as increased optical absorption and emission with size tunable bandgaps.[141] This makes them a strong candidate for optoelectronic devices, such as photodetectors.[135]

Lead sulfide (PbS) quantum dots are the most well studied quantum dot material for photodetection.[142] Bulk PbS possesses a bandgap of ~0.4 eV (3100 nm), but the quantum confinement of nanocrystals allows for a tunable band gap from bulk PbS to 2.50 eV (496 nm) bandgap PbS QDs by reducing the size or changing the shape of the nanocrystal.[143] This extremely large spectral range makes them an optimal material for photodetection over many wavelengths, and opens the potential for gradient devices with several QD sizes to capture specific spectral ranges.

For good quality conductive QD films, monodisperse quantum dots are needed. The native insulating ligands on the as-synthesized quantum dots are not suitable for making conductive films. These ligands are dielectric insulators and must be replaced with shorter ligands to reduce interparticle distance. Due to their confinement in size in all three dimensions, the surface-to-volume ratio is extremely high. Therefore, QDs are even more sensitive to surface conditions and surface effects than other semiconductors with reduce dimensionality. Good quality quantum dot thin films are obtained if QDs are closely packed.[144] This is favored when the size distribution is narrow and the QDs are

spherical.[145] Many different ligand configurations and passivation techniques have been studied to ensure close-packed conductive QD films.[38]

5.2. Nanowire growth

Various synthetic procedures have been used to synthesize nanowires including, vapor-liquid-solid (VLS) growth, solution-liquid-solid (SLS) growth, direct deposition methods, template-directed methods, and oriented-attachment methods.[30] The most widely studied methods have been VLS and SLS growth. SLS growth is a low-temperature (<~350 °C)[30] solution-based method adopted to grow colloidal semiconductor nanowires. Some advantages of SLS growth include systematic control of nanowire diameters as low as the quantum confinement regime, control of surface passivation, nanowire solubility, and large-scale production.[30] VLS growth was discovered in 1964 by Wagner and Ellis[146] and offers high flexibility. VLS growth is a high-temperature (~350-1000 °C)[30] growth method that offers a large range of nanowire sizes and highly crystalline wires. The higher temperature of VLS growth helps to anneal out crystal defects such as stacking faults.

The VLS growth mechanism has been widely studied and consists of three stages: alloying, nucleation, and growth.[30,34,147] The process involves metal nanoclusters as catalysts. These catalysts are heated above the eutectic temperature in the presence of a vapor-phase source of the semiconductor material. This results in a liquid droplet of an alloy of the metal/semiconductor. As the semiconductor source is continually supplied, the droplet will supersaturate, leading to nucleation of a solid semiconductor material. Additional supply of the semiconductor leads to more precipitation of a solid nanowire

through the solid-liquid interface until the temperature is reduced, yielding an end to the process and leaving a metal tip at the end of the nanowire.[34,147]

5.3. Nanowire device preparation

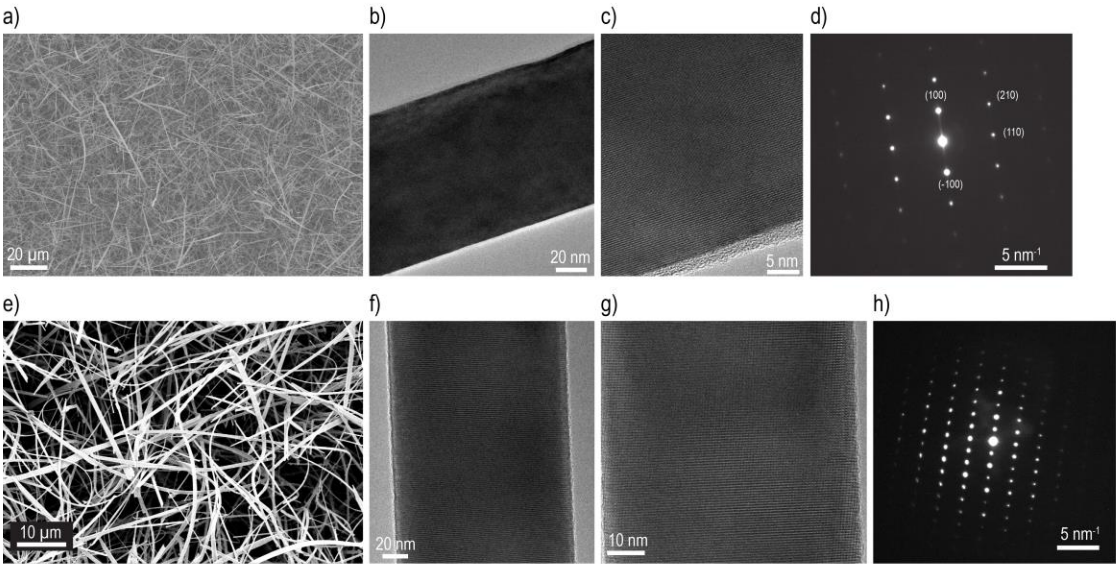

Figure 5.1. a) SEM image of as grown CdS NWs. NW diameter is ~100nm. Scale bar is 20 µm. b) TEM image of CdS NWs. Scale bar is 20nm. c) High resolution TEM image of CdS NWs showing little to no defects. Scale bar is 5 nm. d) Electron diffraction of CdS NWs showing zinc blende structure. The zone axis is [-220] with growth in the [110] direction. Scale bar is 5 nm^{-1}. e) SEM image of as grown CdSe NWs. NW diameter is on the order of 200-400nm. Scale bar is 10 µm. f) SEM image of transferred nanowires onto silicon substrate. Scale bar is 20 nm. g) High resolution TEM image of CdSe NWs showing little to no defects. Scale bar is 10 nm. h) Electron diffraction of CdSs NWs. Scale bar is 5 nm^{-1}.

VLS grown CdS and CdSe nanowires have been synthesized using CdS or CdSe powder as the precursor and Si wafer (100) as a substrate. Either CdS or CdSe powder is used as the precursor with argon gas (or a mixture of argon/hydrogen for CdSe) as a carrier gas. An SEM image of CdS and CdSe grown nanowires show a dense formation of nanowires with diameters on the size range of the gold catalyst used and presence of a gold tip at the end of the nanowire, verifying VLS growth (**Figures 5.1a** and **5.1e**). **Figure 5.1b** shows a transmission electron microscopy (TEM) image of a CdS nanowire

possessing smooth edges. High resolution TEM, shown in **Figure 5.1c**, shows mostly monocrystalline low defect nanowires. Electron diffraction of the same nanowire, shown in **Figure 5.1d**, suggests wurtzite crystal structure with nanowire growth in the [110] direction with a zone axis of [-220]. SEM of as-grown CdSe nanowires is shown in **Figure 5.1e**. TEM of a CdSe nanowire is shown in **Figure 5.1f**, alongside a higher resolution TEM image in **Figure 5.1g** revealing smooth edges and high quality of the nanowire structure. The resulting electron diffraction pattern for the CdSe NW is shown in **Figure 5.1h**.

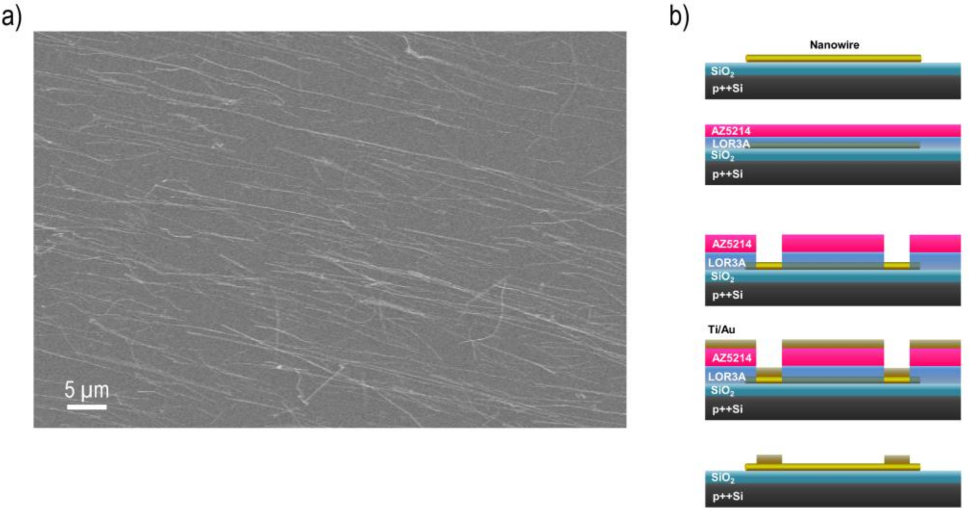

Figure 5.2. a) SEM image of CdS NWs transferred onto a fresh substrate. Scale bar is 5 µm. b) Photolithography process showing bare NW device all the way to a metal contacted NW device (top to bottom).

To study charge transport across semiconductors nanowires, CdS nanowires are transferred onto oxidized silicon wafers to make field-effect transistors (FETs). **Figure 5.2a** shows an SEM image of transferred CdS nanowires via physical contact. Metal contact areas are defined by a photolithography process. After rinsing the transferred nanowires, the substrate is pre-baked at 180°C for 5 minutes. Then, 0.4 µm of liftoff resist LOR3A and 1.25 µm of AZ5214 are deposited one after another. After another

bake, the substrate is aligned with a mask aligner and exposed to UV light for 8-12 seconds. After exposure, the substrates are developed using a 1:4 solution of AZ400 developer solution and DI water. Development time can vary from 25 to 90 seconds, until a rich golden color of the contact pattern is achieved.

Metal contacts are deposited using an electron beam physical vapor deposition system. To create low-barrier, ohmic contacts 30 nm of titanium follows by 70 nm of gold are deposited one after another. After deposition, the substrates are dipped in Remover PG solution for an hour and sonicated to remove excess photoresist and leave define metal contacts. This entire process from transfer to metal deposition is illustrated in **Figure 5.2b**.

Based on the work function of titanium (4.33 eV[148]), an estimated work function of CdS (4.7 eV[149]), the electron affinity of CdS (3.6 eV), and the band gap of CdS (2.41 eV), an accumulation region is expected to develop between the metal-semiconductor interface. However, the electron affinity of CdS can change depending on the actual surface potential of the nanowire. Therefore, while an ohmic contact is expected, a Schottky barrier could be present, which can be controlled by surface modification or the doping level of the nanowire.

5.4. Nanowire photocurrent measurements

Following device fabrication, suitable devices with nanowires spanning electrodes are found using an optical microscope. **Figure 5.3a** shows a resulting device with several electrodes. **Figure 5.3b** shows a nanowire in a device channel spanning two electrodes. After location of a suitable device, the substrate is moved onto a stage consisting of

copper tape to connect the back of the device. Two tungsten probes are used to make contact to the top source and drain electrodes.

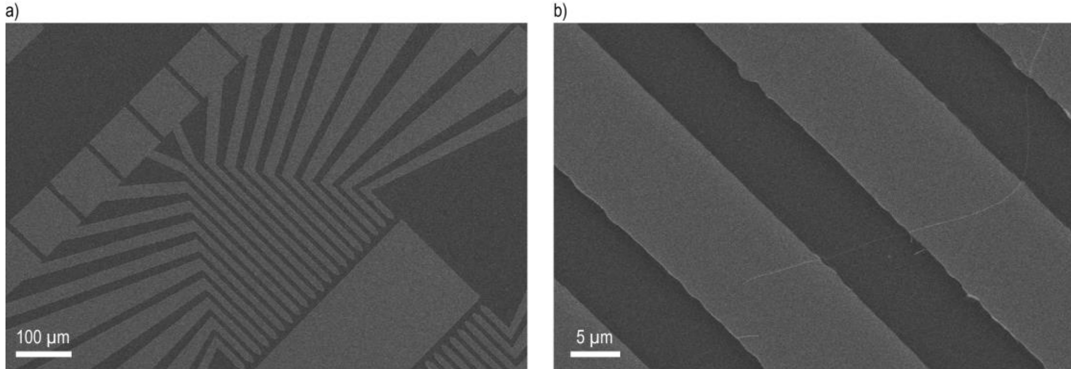

Figure 5.3. a) SEM image of an example device pattern for NW photocurrent measurements. Scale bar is 100 μm. b) SEM image of a NW spanning several Ti/Au contacts, creating a conductive channel. Scale bar is 5 μm.

Initially, current is measured in the absence of light (dark current). A voltage bias is applied across the drain and source electrodes and the drain current is measured. CdS nanowires that are not intentionally doped demonstrate low conductivity and typically higher noise levels. This is due to low intrinsic carrier concentrations or non-ohmic behavior of the metal-semiconductor junction. **Figure 5.4a** shows a representative dark current measured in both forward and reverse directions. An unnatural larger current is seen at the beginning of the sweep, but nearly all the current lies in the sub 10 pA range, indicating little conductivity in the dark. The dark resistance of the channel is calculated at 10V to be 980.4 GΩ.

Under illumination the current increases significantly (resistance decreases). **Figure 5.4b** shows current-voltage curves of the same nanowire under several different laser powers of 444 nm laser illumination. The current increases with increasing illumination power and looks fairly linear under higher powers, indicating ohmic conduction. Responsivity of the device to 444 nm light decreases from 0.0607 A/W to 0.0230 A/W

from the lowest to highest illumination powers. In addition, the on/off ratio between light and dark currents increases from 1.39 x 10^6 to 2.47 x 10^6 from the lowest to highest powers.

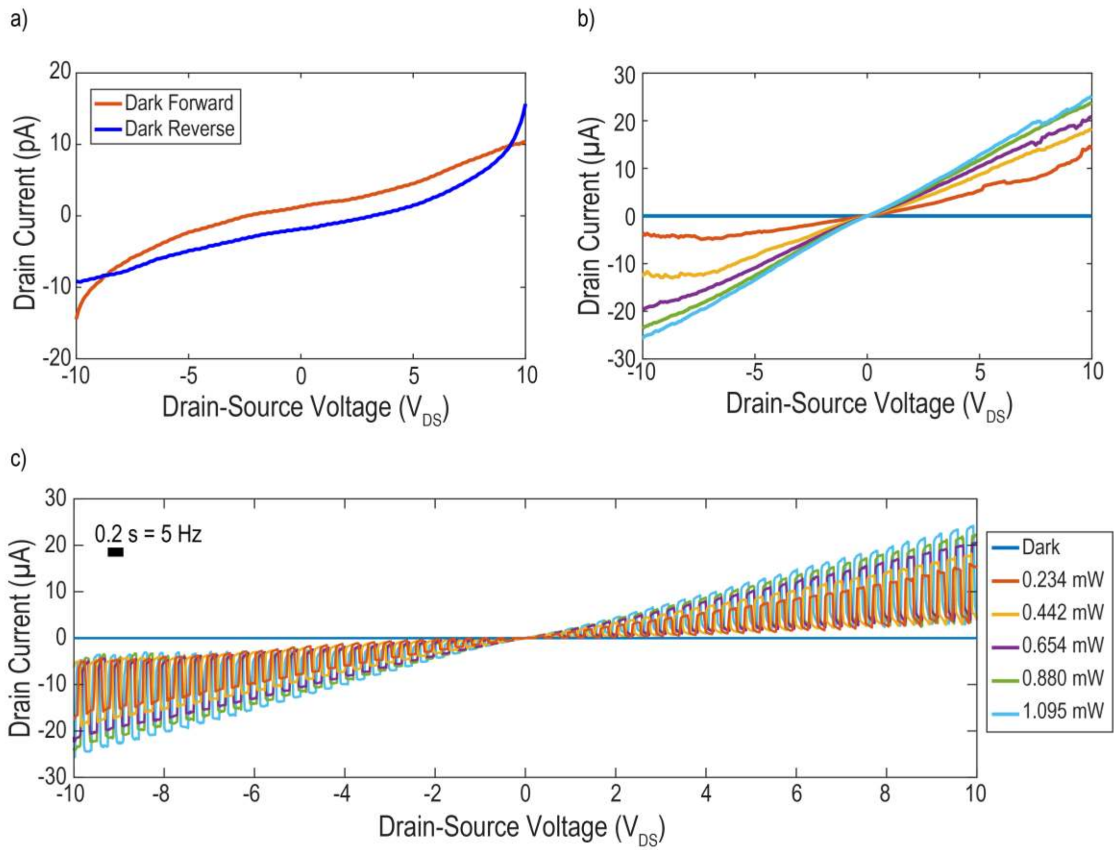

Figure 5.4. a) Dark current of the CdS nanowire device in forward and reverse voltage directions. b) Current-voltage characteristics of the device in the dark and under various 444 nm light intensities. c) Current-voltage characteristics of the device under various 444 nm light intensities that are mechanically chopped at 5 Hz.

To further compare the difference in conduction modes with and without illumination and to describe the rise and fall times of the device, a chopper measurement was performed using mechanically chopped laser light at 5 Hz (**Figure 5.4c**). The top currents represent a similar light current to the previous measurement, but the dark current clearly does not return to pA level currents. This reduces the working on/off ratio at this timescale. The current features are square on the light current side of the response, but

clearly showing an exponential decay towards the dark current. A possible reason for this outcome is the presence of persistent photocurrent.

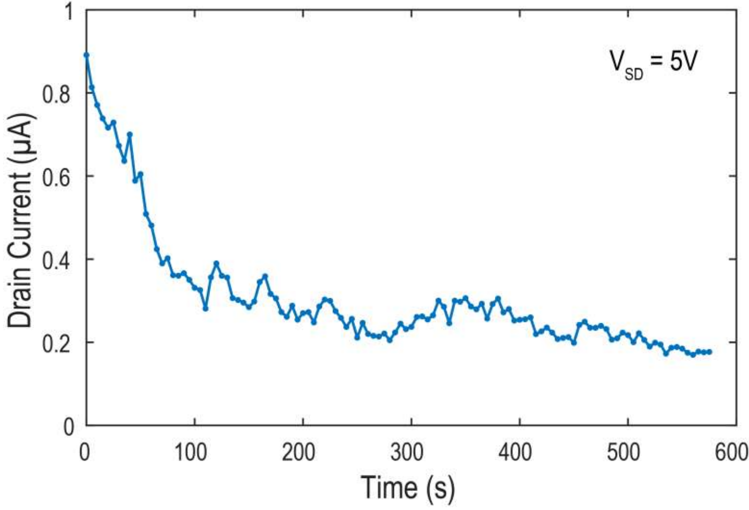

Figure 5.5. Current of a CdS nanowire held at a potential of 5 volts after exposure to light. Illumination is stopped at time 0. After 9.5 minutes, the persistent photocurrent is still more than 20% of the original photocurrent.

Persistent photocurrent represents a photocurrent that exists for up to seconds or hours after the illumination source is terminated. This has been commonly seen in nanowire devices.[150–152] Defect states in the nanowire may be a cause of persistent photoconductivity. Defect states can trap the charge carriers, potentially for a long time, and the interactions to release charges from these states may be extremely slow. For ZnO nanowires, this phenomena was explained by oxygen vacancy states.[151] In our case, we have seen persistent photocurrent that lasts up to several minutes. **Figure 5.5** shows an example of persistent photocurrent from a different CdS nanowire at 5 volts. The photocurrent signal is still showing greater than 100 nA after 575 seconds. This result is similar to decay studies in CdS nanorod thin films, where decay depended on a fast decay of a few seconds followed by a slow decay of about 100 seconds.[153] In this case, the

photocurrent decays over a period of 100s and then decays slowly over several hundred seconds.

5.5. Quantum dot device preparation

Oleate-capped PbS quantum dots were synthesized via a previously reported synthetic route.[154] The quantum dots are then precipitated and redispersed (PR) under nitrogen atmosphere using anhydrous octane and methyl acetate, respectively. 250 nmol of PbS QDs are further purified by use of gel permeation chromatography (GPC) to remove impurities and to allow for stable, repeatable quantum dot starting materials after purification (which can be problematic by using only PR methods).[155] The QD solution is then passed through a 0.2 μm filter, concentrated to 30 mg/mL by removing excess solvent, and filtered again. The resultant PbS QDs have an absorption peak centered at 941 nm as shown in **Figure 5.6**, calculated to yield 2.73 nm diameter quantum dots possessing a bandgap of 1.32 eV.

To create conductive quantum dot films, the oleate ligands are replaced by 1,2-ethanedithiol (EDT) in a layer-by-layer spin coating process to passivate QD surface traps and reduce the interparticle distance – increasing the coupling strength of the quantum dots. PbS-EDT films have been shown to increase the mobility of QD films and have been used in FET and solar cell configurations.[156,157] 25 μL of the PbS solution is deposited onto a silicon oxide substrate patterned with pre-deposited Au contacts (15 nm Ti / 35 nm Au) fabricated by the same photolithography process illustrated for the semiconductor nanowire devices shown in **Figure 5.2b**. The QD solution is spun at 3000 rpm for 30s. 3 drops of 2% by volume EDT in acetonitrile is added and spun for 3000 rpm for an additional 30s. Finally, 2 drops of acetonitrile is added and spun at 3000 rpm

for 30s to wash off excess EDT and 2 drops of toluene is spun at 3000 rpm for 30s to wash off excess oleic acid. The film is then annealed for 15 minutes at 60°C. Following 1 minute of cooling, this entire process is repeated three times to create a three-layer PbS-EDT film. To reduce deterioration of the film to oxygen, a layer of poly(methyl methacrylate) (PMMA) is added to the top of the film. 2 drops of 4% PMMA by weight in toluene is added and spun at 3000 rpm for 60s. This entire process is done under nitrogen atmosphere in a glove box.

SEM images of the quantum dot films are shown in **Figure 5.7**. PbS-EDT films show a mostly smooth, homogenous film but does possess some small range cracking. These cracks can be as large as several tens of nm. This is an improvement over other earlier reported PbS-EDT films, which have shown large cracks on the order of several hundred nanometers to even possibly 1μm.[158] Three-layer PbS-EDT films have a thickness of ~120 nm determined by cross-sectional SEM shown in **Figure 5.7c**. The PMMA capping layer has been determined to be about 300 nm by profilometry.

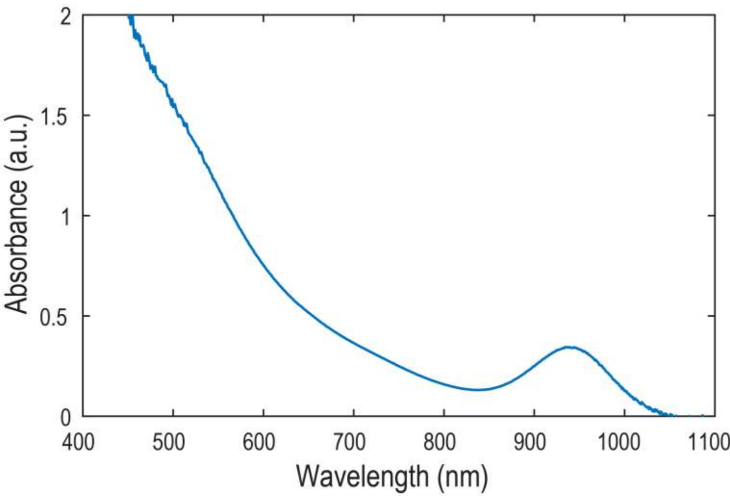

Figure 5.6. Absorption spectrum of PbS quantum dots after purification.

5.6. Quantum dot photocurrent measurements

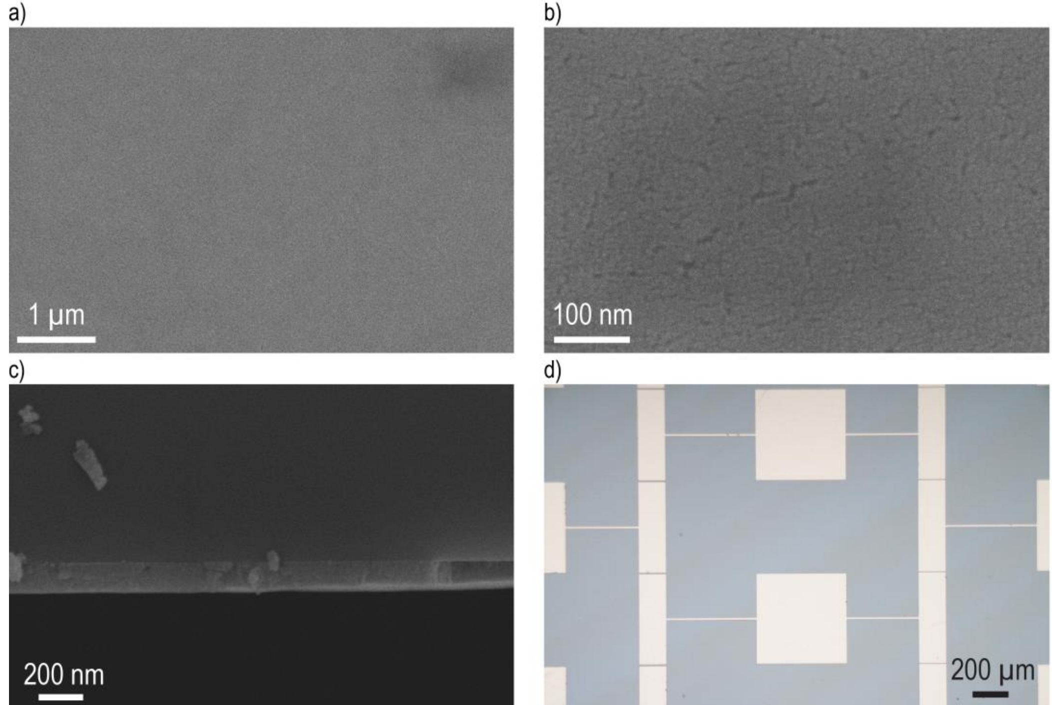

Figure 5.7. a) SEM image of a PbS-EDT film. b) Higher magnification SEM image of a PbS-EDT film showing small cracks of several nanometers. c) Cross-sectional SEM image of the QD film on Si, showing film thickness ~120 nm. d) Optical microscope image of QD test patterns.

After film deposition, the substrate is moved onto a stage consisting of copper tape to connect the back of the device. Two tungsten probes are used to make contract to the top source and drain electrodes. **Figure 5.7d** shows the contact pattern used for testing QD devices. The device pattern consists of several rectangular Au contacts consisting of channels of various lengths and widths. The device to be described below was measured through a channel length of 20 µm and a width of 50 µm.

Initially, current is measured in the absence of light (dark current). A voltage bias is applied across the drain and source electrodes and the drain current is measured. **Figure 5.8a** shows a representative dark current measured from -10 to 10 volts. The dark current shows extremely linear and symmetrical behavior, indicating good ohmic contacts

between PbS-EDT and Au. This is expected as the QD film is expected to be p-type and form ohmic contacts with Au.[142,159] The dark resistance of the channel is calculated at 10V to be 10.8 GΩ and the dark current density is calculated to be 18.5 μA/cm^2 at 10V. Conductivity suggests the successful removal of insulating oleate ligands for conductive EDT ligands.

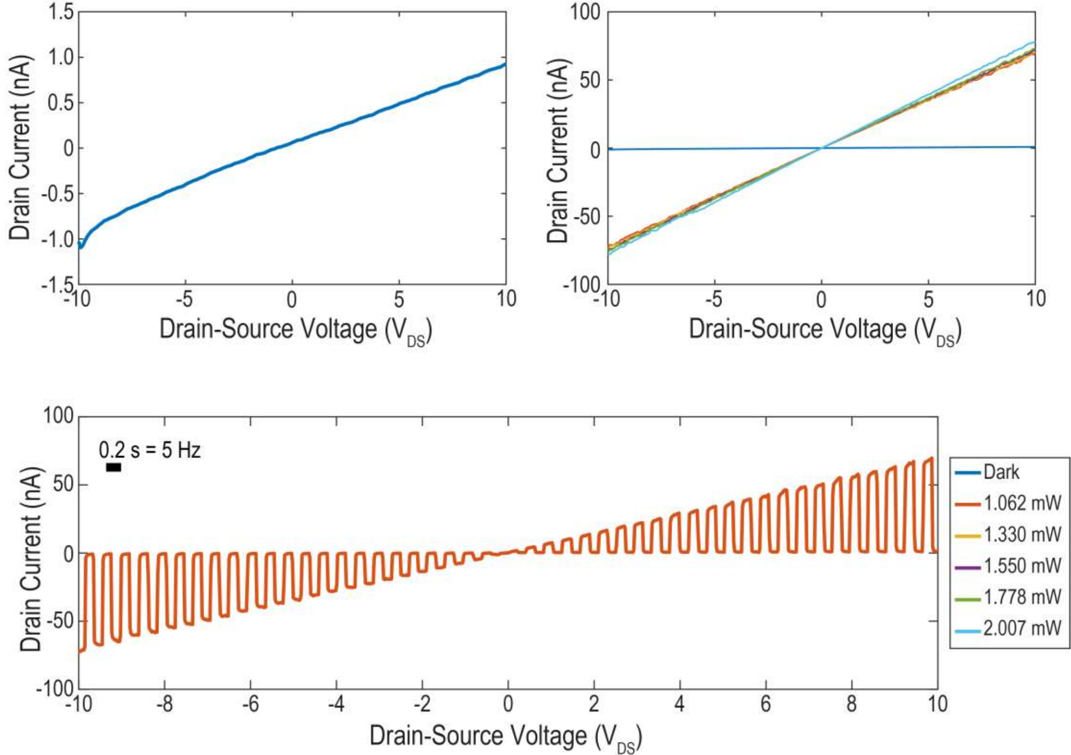

Figure 5.8. a) Dark current of the PbS-EDT device. b) Current-voltage characteristics of the device in the dark and under various 444 nm light intensities. c) Current-voltage characteristics of the device under 1.062 mW of 444 nm light that is mechanically chopped at 5 Hz.

Under 444 nm illumination the current increases significantly. **Figure 5.8b** shows current-voltage curves of the same QD device under several different laser powers of 444 nm laser illumination. The current increases (resistance decreases) with increasing illumination power and looks continues its linear response, indicating ohmic conduction. Responsivity of the device to 444 nm light decreases from 79.8 μA/W to 39.0 μA/W

from the lowest to highest illumination powers as shown in **Figure 5.8b**. In addition, the on/off ratio between light and dark currents increases from 64.30 to 75.72 from the lowest to highest powers.

To further compare the difference in conduction modes with and without illumination, and to describe the rise and fall times of the device, a chopper measurement was performed using mechanically chopped laser light at 5 Hz (**Figure 5.8c**). The device shows similar on/off ratios as the standalone measurements, as the device returns to its natural dark currents over the 0.2s chopping time. The edges of the rise and fall profiles indicate fast response of the device.

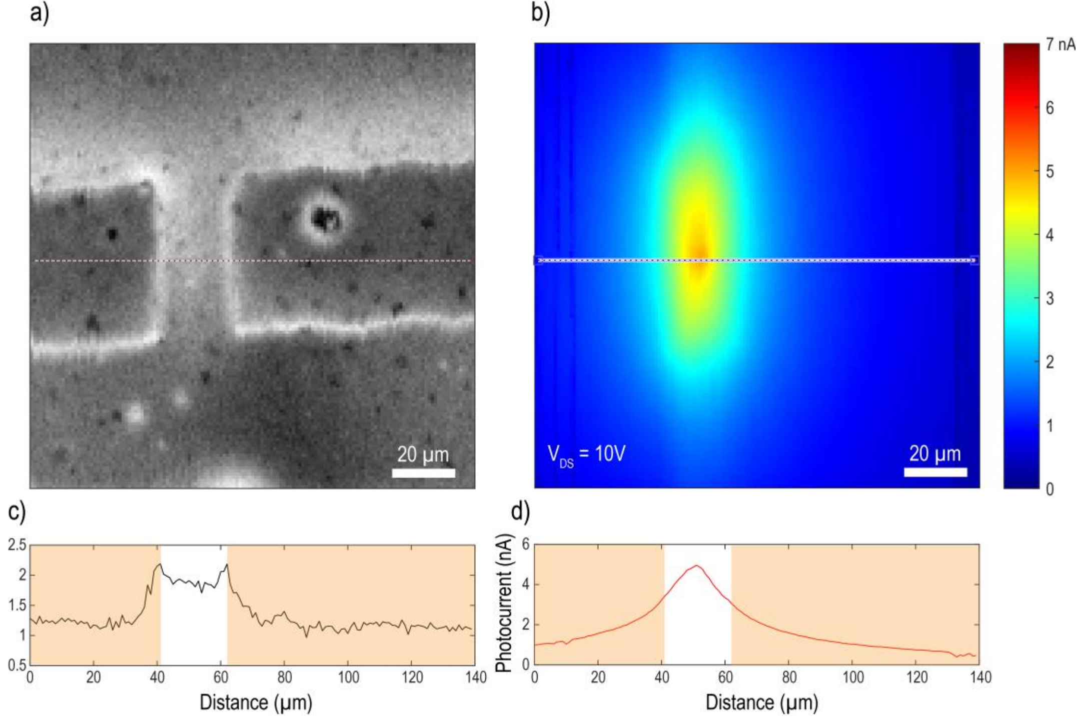

Figure 5.9. a) Reflected signal of a PbS-EDT device covered in PMMA over Au contacts with a channel width of 20 μm. b) Scanning photocurrent image of the same PbS-EDT device, showing a symmetrical photocurrent signal with a peak in the center of the conductive channel. c) and d) Reflected signal profile and photocurrent profile along the dotted line indicated in a) and b). Colored background indicates the position of the Au contacts. Scale bars are 20 μm.

5.7. SPCM of quantum dot device

Scanning photocurrent maps can also give details about the contact behavior in lateral quantum dot films. **Figure 5.9a** shows a reflected signal image of a quantum dot film covered in PMMA on top of Au contacts – indicated by the large rectangles in the center of the image. **Figure 5.9b** shows a photocurrent image at 10 volts over the same device area shown in **Figure 5.9a**. A peak photocurrent exists directly between the two contacts and then decreases exponentially with distance. A similar photocurrent image has been seen previously in PbS quantum dot devices to indicate ohmic contacts.[17] In the case of Schottky barriers at the contacts, the photocurrent signal would be localized to the reverse biased contact. The profiles of each image along the dotted line is shown in **Figures 5.9c** and **5.9d**. The shaded boxes indicate the position of the Au contacts with a 20 μm channel between the two contacts.

5.8. Summary and future work

In summary, CdS nanowires and PbS quantum dots have been prepared and fabricated into optoelectronic devices. Their photocurrents have been measured leading to an on/off ratio of ~10^6 and ~70 and a responsivity of ~10^{-2} A/W and 10^{-6} A/W for devices made with CdS NWs and PBS-EDT QDs, respectively. Persistent photocurrent exists for up to 10 minutes in CdS NW devices. The linear nature of the current-voltage curves indicates ohmic transport in both NW and QD devices. This is further demonstrated by the SPCM map of a QD film showing a symmetrical photocurrent signal with a peak centered between the two contacts.

The results of this work have adequately prepared our lab up for future investigation of nanoscale electronics. Specific projects based on ligand and surface chemistry of both NWs and QDs, where the surface states and surface potentials can alter their optical and electronic properties will be investigated. Electronic characterization of photodoped NWs, as well as, SLS NWs and doped SLS NWs will also be studied in the future. Additionally, QD surface chemistry will be monitored electronically by FET measurements. Further current-voltage studies and SPCM on QD and NW FETs will be studied to measure device mobility and diffusion length. Suitable QDs may additionally be deposited on graphene to make infrared photodetectors.

5.9. Methods and materials

5.9.1 Synthesis of VLS CdS (CdSe) NWs

1.5 cm by 1 cm silicon substrates (100) were cleaned by sonication in acetone, rinsed with DI water, and blown dry with nitrogen gas. poly-L-Lysine (Ted Pella Inc.) was pipeted onto the substrate to cover the surface. After 5 minutes, the substrate was rinsed with DI water and blown dry with nitrogen gas. Small droplets of 40, 80, or 100 nm diameter Au colloids (BBI International) were deposited onto the silicon substrate to designate catalytic growth areas. After 5 minutes, the substrate was rinsed with DI water and blown dry with nitrogen gas. The substrates are then transferred into a small quartz tube, which is placed into a 55 cm long quartz tube alongside 0.05g of CdS precursor in a boat. The tube was moved into a tube furnace assembly (Lindberg Blue M, Thermo Scientific). The system was evacuated on one end to 10^{-4} torr, while the pressure in the tube is held at 300 torr. Argon was passed as a carrier gas at a rate of 100 standard cubic centimeters per minute (sccm) and the reactor is heated to 780°C. The precursor boat was

moved inside the assembly to heat the CdS powder (99.999%, Alfa Aesar) to the furnace temperature. The growth substrate was located further downstream at the temperature of ~550°C. After 30 minutes of growth, the furnace was returned to room temperature, the vacuum was removed, and the nanowire substrate was removed from the system.

The process is similar for CdSe nanowire growth with a few modifications. The growth catalyst was a 3-10 nm Au film, CdSe precursor powder was used, and the carrier gas was a mixture of 25 sccm of Ar and 55 sccm of H_2 gases. The precursor powder was heated to 900°C and the growth substrate is downstream at ~400°C. The nanowires are then grown for 60 minutes.

5.9.2 Synthesis of PbS QDs

0.225g of PbO (99.9 %, Alfa Aesar), 1g of oleic acid (OA) (99%, BeanTown Chemical), 5g of 1-octadecene (ODE) (90%, Acros Organics) are loaded into a 50 mL three-neck round bottom flask fitted with a condenser and adapter. The mixture was then degassed on a schlenk line for 30 minutes at room temperature and then the temperature is raised to 110°C for 60 minutes to obtain a clear solution of lead oleate under vacuum. 105 µL of bis(trimethylsilyl) sulfide ($(TMS)_2S$) (95%, Acros Organics) was mixed with 2.5 mL of ODE inside a nitrogen-filled glove box to create the sulfur precursor. $(TMS)_2S$ was quickly injected into the reaction mixture at 95.0°C. Upon QD nucleation, the reaction was rapidly quenched to 25°C by removing the heating mantle. Absorption of the stock crude was taken by dissolving 25 µL of the crude sample in 2.5 mL of anhydrous octane (Cary 5000 UV-Vis-NIR).

5.9.3 Purification of PbS QDs

The crude reaction mixture was transferred into a septa-capped centrifuge tube under nitrogen. 30 mL of methyl acetate (dried over molecular sieves) was added to the crude solution to precipitate the quantum dots. The resulting mixture was centrifuged at 7000 rpm for 10 minutes. After centrifugation, the clear supernatant was extracted and the QDs were pumped dry by vacuum. The dry sample was transferred into a nitrogen-filled glove box and redispersed in 5 mL anhydrous toluene. Absorption following precipitation and redissolution was taken by a Cary 5000 UV-Vis-NIR.

The PbS QDs were subsequently purified by gel permeation chromatography (GPC). To pack the column, 4g of Bio-Beads were swollen in toluene overnight. Clean solvent was placed into a glass column (1 cm diameter) with a 0.2 μm pore size filter, glass wool, and a Teflon valve. All of the swollen beads were transferred to the column, resulting in a height of ~30 cm. A small amount of sand was carefully placed at the top of the column and pure solvent was used to rinse the column until no free polystyrene was present in the eluent (confirmed by UV-Vis absorption). 250 nmol of QDs were injected by a syringe into the top of the GPC column. After passing through the column, the QDs were collected and concentrated up to 30 mg/mL. Absorption post-GPC was taken by a Cary 5000 UV-Vis-NIR.

5.9.4 Device Fabrication

200nm SiO_2 thin film silicon wafers were cleaned by sonication in acetone, rinsed with isopropanol and water, and then dried by nitrogen gas. The substrate was then heated at 180°C for 5 minutes. The chip was covered with LOR3A liftoff resist and spin coated at 2000 rpm for 30s to deposit a 0.4 μm film. The resulting photolithographic film was soft

baked at 180°C for 5 minutes. A positive photoresist, AZ5214, was deposited onto the chip and spun at 5000 rpm for 60s to create a 1.25 μm film. The substrate was soft baked at 110°C for 1 minute. The photoresist layers were then exposed to UV light under a specific photomask pattern for 8-12s. Following exposure, the photolithographic patterns are developed in 1:4 AZ400K:H_2O until a golden color of the SiO_2 layer was seen at the UV-exposed regions of the substrate. The chip is then dried by nitrogen and moved to a metal deposition chamber.

The substrate is loaded in a metal deposition chamber, which was then evacuated to 1.3 x 10^{-6} torr. High voltage was applied (5 kV) and Ti and Au were deposited by raising the emission current to promote physical vapor deposition. Following deposition, the chamber is brought to atmospheric pressure and the substrate is submerged in Remover PG solution to remove excess photoresist, leaving patterned metal contacts on the substrate.

5.9.5 Photocurrent Setup

All current-voltage curves were measured using tungsten probes (Micromanipulator 7B) to contact the gold contact surfaces. Voltage and current were applied and measured by a Keithley 2636A sourcemeter.

5.9.6 SPCM Setup

A home-built microscope with a motion-controlled stage was used for simultaneous reflection imaging and photocurrent mapping. A diode laser (λ = 444 nm) is mechanically chopped (~287 Hz) and focused to a diffraction-limited spot through a 20x objective lens (NA = 0.42, Mitutoyo Corporation). At each point the reflected signal was recorded for imaging by a lock-in amplifier (Ametek 7230), and the photocurrent was recorded by a

pre-amplifier (DL Instruments 1211) and lock-in amplifier combination (SRS SR830). A Keithley 2636A sourcemeter was used to apply voltage. Reflected and photocurrent maps were plotted and analyzed using MATLAB. All images were measured at a 2 μm step size.

REFERENCES

(1) Graham, R.; Yu, D. Scanning Photocurrent Microscopy in Semiconductor Nanostructures. *Mod. Phys. Lett. B* **2013**, *27* (25), 1330018.

(2) Ahn, Y.; Dunning, J.; Park, J. Scanning Photocurrent Imaging and Electronic Band Studies in Silicon Nanowire Field Effect Transistors. *Nano Lett.* **2005**, *5* (7), 1367–1370.

(3) Gu, Y.; Romankiewicz, J. P.; David, J. K.; Lensch, J. L.; Lauhon, L. J. Quantitative measurement of the electron and hole mobility-lifetime products in semiconductor nanowires. *Nano Lett.* **2006**, *6* (5), 948–952.

(4) Howell, S. L.; Padalkar, S.; Yoon, K.; Li, Q.; Koleske, D. D.; Wierer, J. J.; Wang, G. T.; Lauhon, L. J. Spatial mapping of efficiency of GaN/InGaN nanowire array solar cells using scanning photocurrent microscopy. *Nano Lett.* **2013**, *13* (11), 5123–5128.

(5) Tang, J.; Huo, Z.; Brittman, S.; Gao, H.; Yang, P. Solution-processed core-shell nanowires for efficient photovoltaic cells. *Nat. Nanotechnol.* **2011**, *6* (9), 568–572.

(6) Yang, Y.; Li, J.; Wu, H.; Oh, E.; Yu, D. Controlled Ambipolar Doping and Gate Voltage Dependent Carrier Diffusion Length in Lead Sulfide Nanowires. *Nano Lett.* **2012**, *12* (11), 5890–5896.

(7) Burghard, M.; Mews, A. High-Resolution Photocurrent Mapping of Carbon Nanostructures. *ACS Nano* **2012**, *6* (7), 5752–5756.

(8) Ahn, Y. H.; Tsen, W.; Kim, B.; Park, Y. W.; Park, J. Photocurrent Imaging of p-n

Junctions and Local Defects in Ambipolar Carbon Nanotube Transistors. *Nano Lett.* **2007**, *7* (11), 3320–3323.

(9) Barkelid, M.; Steele, G. A.; Zwiller, V. Probing Optical Transitions in Individual Carbon Nanotubes Using Polarized Photocurrent Spectroscopy. *Nano Lett.* **2012**, *12* (11), 5649–5653.

(10) Lee, E. J. H.; Balasubramanian, K.; Weitz, R. T.; Burghard, M.; Kern, K. Contact and edge effects in graphene devices. *Nat. Nanotechnol.* **2008**, *3* (8), 486–490.

(11) Park, J.; Ahn, Y. H.; Ruiz-Vargas, C. Imaging of Photocurrent Generation and Collection in Single-Layer Graphene. *Nano Lett.* **2009**, *9* (5), 1742–1746.

(12) Xia, F.; Mueller, T.; Golizadeh-Mojarad, R.; Freitag, M.; Lin, Y.; Tsang, J.; Perebeinos, V.; Avouris, P. Photocurrent Imaging and Efficient Photon Detection in a Graphene Transistor. *Nano Lett.* **2009**, *9* (3), 1039–1044.

(13) Xu, X.; Gabor, N. M.; Alden, J. S.; van der Zande, A. M.; McEuen, P. L. Photo-Thermoelectric Effect at a Graphene Interface Junction. *Nano Lett.* **2010**, *10* (2), 562–566.

(14) Howell, S. L.; Jariwala, D.; Wu, C. C.; Chen, K. S.; Sangwan, V. K.; Kang, J.; Marks, T. J.; Hersam, M. C.; Lauhon, L. J. Investigation of Band-Offsets at Monolayer-Multilayer MoS_2 Junctions by Scanning Photocurrent Microscopy. *Nano Lett.* **2015**, *15* (4), 2278–2284.

(15) Lana-Villarreal, T.; Monllor-Satoca, D.; Gómez, R.; Salvador, P. Determination of electron diffusion lengths in nanostructured oxide electrodes from photopotential maps obtained with the scanning microscope for semiconductor characterization. *Electrochem. commun.* **2006**, *8* (11), 1784–1790.

(16) Park, J. K.; Kang, J. C.; Kim, S. Y.; Son, B. H.; Park, J. Y.; Lee, S.; Ahn, Y. H. Diffusion length in nanoporous photoelectrodes of dye-sensitized solar cells under operating conditions measured by photocurrent microscopy. *J. Phys. Chem. Lett.* **2012**, *3* (23), 3632–3638.

(17) Strasfeld, D. B.; Dorn, A.; Wanger, D. D.; Bawendi, M. G. Imaging Schottky Barriers and Ohmic Contacts in PbS Quantum Dot Devices. *Nano Lett.* **2012**, *12* (2), 569–575.

(18) Otto, T.; Miller, C.; Tolentino, J.; Liu, Y.; Law, M.; Yu, D. Gate-Dependent Carrier Diffusion Length in Lead Selenide Quantum Dot Field-Effect Transistors. *Nano Lett.* **2013**, *13*, 3463–3469.

(19) Liu, S.; Wang, L.; Lin, W. C.; Sucharitakul, S.; Burda, C.; Gao, X. P. A. Imaging the Long Transport Lengths of Photo-generated Carriers in Oriented Perovskite Films. *Nano Lett.* **2016**, *16* (12), 7925–7929.

(20) Xiao, R.; Hou, Y.; Fu, Y.; Peng, X.; Wang, Q.; Gonzalez, E.; Jin, S.; Yu, D. Photocurrent Mapping in Single-Crystal Methylammonium Lead Iodide Perovskite Nanostructures. *Nano Lett.* **2016**, *16* (12), 7710–7717.

(21) National Renewable Energy Laboratory. Best Research-Cell Efficiencies https://www.nrel.gov/pv/assets/images/efficiency-chart.png (accessed Feb 10, 2018).

(22) Xu, X.; Randorn, C.; Efstathiou, P.; Irvine, J. T. S. A red metallic oxide photocatalyst. *Nat. Mater.* **2012**, *11* (7), 595–598.

(23) Babu, R.; Giribabu, L.; Singh, S. P. Recent Advances in Halide-Based Perovskite Crystals and Their Optoelectronic Applications. *Cryst. Growth Des.* **2018**,

acs.cgd.7b01767.

(24) Bi, D.; Yang, L.; Boschloo, G.; Hagfeldt, A.; Johansson, E. M. J. Effect of Different Hole Transport Materials on Recombination in $CH_3NH_3PbI_3$ Perovskite-Sensitized Mesoscopic Solar Cells. *J. Phys. Chem. Lett.* **2013**, *4* (9), 1532–1536.

(25) Subbiah, A. S.; Halder, A.; Ghosh, S.; Mahuli, N.; Hodes, G.; Sarkar, S. K. Inorganic Hole Conducting Layers for Perovskite-Based Solar Cells. *J. Phys. Chem. Lett.* **2014**, *5* (10), 1748–1753.

(26) You, J.; Meng, L.; Song, T.-B.; Guo, T.-F.; Yang, Y. (Michael); Chang, W.-H.; Hong, Z.; Chen, H.; Zhou, H.; Chen, Q.; Liu, Y.; De Marco, N.; Yang, Y. Improved air stability of perovskite solar cells via solution-processed metal oxide transport layers. *Nat. Nanotechnol.* **2015**, *11* (1), 75–81.

(27) Beshkova, M.; Hultman, L.; Yakimova, R. Device applications of epitaxial graphene on silicon carbide. *Vacuum* **2016**, *128*, 186–197.

(28) Mishra, N.; Boeckl, J.; Motta, N.; Iacopi, F. Graphene growth on silicon carbide: A review. *Phys. status solidi* **2016**, *213* (9), 2277–2289.

(29) de Heer, W. A.; Berger, C.; Ruan, M.; Sprinkle, M.; Li, X.; Hu, Y.; Zhang, B.; Hankinson, J.; Conrad, E. Large area and structured epitaxial graphene produced by confinement controlled sublimation of silicon carbide. *Proc. Natl. Acad. Sci. U. S. A.* **2011**, *108* (41), 16900–16905.

(30) Dasgupta, N. P.; Sun, J.; Liu, C.; Brittman, S.; Andrews, S. C.; Lim, J.; Gao, H.; Yan, R.; Yang, P. 25th Anniversary Article: Semiconductor Nanowires - Synthesis, Characterization, and Applications. *Adv. Mater.* **2014**, *26* (14), 2137–

2184.

(31) Barrelet, C. J.; Wu, Y.; Bell, D. C.; Lieber, C. M. Synthesis of CdS and ZnS Nanowires Using Single-Source Molecular Precursors. *J. Am. Chem. Soc.* **2003**, *125* (38), 11498–11499.

(32) Dayeh, S. A.; Soci, C.; Bao, X.-Y.; Wang, D. Advances in the synthesis of InAs and GaAs nanowires for electronic applications. *Nano Today* **2009**, *4* (4), 347–358.

(33) Duan, X.; Lieber, C. M. Laser-Assisted Catalytic Growth of Single Crystal GaN Nanowires. *J. Am. Chem. Soc.* **2000**, *122* (1), 188–189.

(34) Wu, Y.; Yang, P. Direct Observation of Vapor−Liquid−Solid Nanowire Growth. *J. Am. Chem. Soc.* **2001**, *123* (13), 3165–3166.

(35) Desnica, U. V. Doping limits in II–VI compounds — Challenges, problems and solutions. *Prog. Cryst. Growth Charact. Mater.* **1998**, *36* (4), 291–357.

(36) Maiolo III, J. R.; Atwater, H. A.; Lewis, N. S. Macroporous Silicon as a Model for Silicon Wire Array Solar Cells. *J. Phys. Chem. C* **2008**, *112* (15), 6194–6201.

(37) DeMeo, D.; MacNaughton, S.; Sonkusale, S.; Vandervelde, T. Electrodeposited Copper Oxide and Zinc Oxide Core-Shell Nanowire Photovoltaic Cells. In *Nanowires - Implementations and Applications*; InTech, 2011.

(38) Kagan, C. R.; Murray, C. B. Charge transport in strongly coupled quantum dot solids. *Nat. Nanotechnol.* **2015**, *10*, 1013–1026.

(39) Smith, A. M.; Nie, S. Semiconductor Nanocrystals: Structure, Properties, and Band Gap Engineering. *Acc. Chem. Res.* **2010**, *43* (2), 190–200.

(40) Lim, S. J.; Ma, L.; Schleife, A.; Smith, A. M. Quantum dot surface engineering:

Toward inert fluorophores with compact size and bright, stable emission. *Coord. Chem. Rev.* **2016**, *320–321*, 216–237.

(41) Liu, Y.; Gibbs, M.; Puthussery, J.; Gaik, S.; Ihly, R.; Hillhouse, H. W.; Law, M. Dependence of Carrier Mobility on Nanocrystal Size and Ligand Length in PbSe Nanocrystal Solids. *Nano Lett.* **2010**, *10*, 1960–1969.

(42) Miyano, K.; Tripathi, N.; Yanagida, M.; Shirai, Y. Lead Halide Perovskite Photovoltaic as a Model p-i-n Diode. *Acc. Chem. Res.* **2016**, *49* (2), 303–310.

(43) Kim, H.; Lim, K.-G.; Lee, T.-W. Planar heterojunction organometal halide perovskite solar cells: roles of interfacial layers. *Energy Environ. Sci.* **2016**, *9* (1), 12–30.

(44) Belisle, R. A.; Jain, P.; Prasanna, R.; Leijtens, T.; McGehee, M. D. Minimal Effect of the Hole-Transport Material Ionization Potential on the Open-Circuit Voltage of Perovskite Solar Cells. *ACS Energy Lett.* **2016**, *1* (3), 556–560.

(45) Sheng, R.; Ho-Baillie, A.; Huang, S.; Chen, S.; Wen, X.; Hao, X.; Green, M. A. Methylammonium Lead Bromide Perovskite-Based Solar Cells by Vapor-Assisted Deposition. *J. Phys. Chem. C* **2015**, *119* (7), 3545–3549.

(46) Chang, J.; Xiao, J.; Lin, Z.; Zhu, H.; Xu, Q.-H.; Zeng, K.; Hao, Y.; Ouyang, J. Elucidating the charge carrier transport and extraction in planar heterojunction perovskite solar cells by Kelvin probe force microscopy. *J. Mater. Chem. A* **2016**, *4* (44), 17464–17472.

(47) Gao, P.; Cho, K. T.; Abate, A.; Grancini, G.; Reddy, P. Y.; Srivasu, M.; Adachi, M.; Suzuki, A.; Tsuchimoto, K.; Grätzel, M.; Nazeeruddin, M. K. An efficient perovskite solar cell with symmetrical Zn(II) phthalocyanine infiltrated buffering

porous Al_2O_3 as the hybrid interfacial hole-transporting layer. *Phys. Chem. Chem. Phys.* **2016**, *18* (39), 27083–27089.

(48) Han, J.; Wang, H.-Y.; Wang, Y.; Yu, M.; Yuan, S.; Sun, P.; Qin, Y.; Guo, Z.-X.; Zhang, J.-P.; Ai, X.-C. Efficient promotion of charge separation and suppression of charge recombination by blending PCBM and its dimer as electron transport layer in inverted perovskite solar cells. *RSC Adv.* **2016**, *6* (113), 112512–112519.

(49) Liu, X.; Kong, F.; Tan, Z.; Cheng, T.; Chen, W.; Yu, T.; Guo, F.; Chen, J.; Yao, J.; Dai, S. Diketopyrrolopyrrole or benzodithiophene-arylamine small-molecule hole transporting materials for stable perovskite solar cells. *RSC Adv.* **2016**, *6* (90), 87454–87460.

(50) Handa, T.; Tex, D. M.; Shimazaki, A.; Wakamiya, A.; Kanemitsu, Y. Charge Injection Mechanism at Heterointerfaces in $CH_3NH_3PbI_3$ Perovskite Solar Cells Revealed by Simultaneous Time-Resolved Photoluminescence and Photocurrent Measurements. *J. Phys. Chem. Lett.* **2017**, *8* (5), 954–960.

(51) Xing, G.; Mathews, N.; Sun, S.; Lim, S. S.; Lam, Y. M.; Graetzel, M.; Mhaisalkar, S.; Sum, T. C.; Grätzel, M.; Mhaisalkar, S.; Sum, T. C. Long-Range Balanced Electron-and Hole-Transport Lengths in Organic-Inorganic $CH_3NH_3PbI_3$. *Science (80-.).* **2013**, *342* (6156), 344–347.

(52) Stranks, S. D.; Eperon, G. E.; Grancini, G.; Menelaou, C.; Alcocer, M. J. P.; Leijtens, T.; Herz, L. M.; Petrozza, A.; Snaith, H. J. Electron-Hole Diffusion Lengths Exceeding 1 Micrometer in an Organometal Trihalide Perovskite Absorber. *Science (80-.).* **2013**, *342* (6156), 341–344.

(53) Piatkowski, P.; Cohen, B.; Ponseca, C. S.; Salado, M.; Kazim, S.; Ahmad, S.;

Sundstrom, V.; Douhal, A. Unraveling Charge Carriers Generation, Diffusion, and Recombination in Formamidinium Lead Triiodide Perovskite Polycrystalline Thin Film. *J. Phys. Chem. Lett.* **2016**, *7* (1), 204–210.

(54) Johnston, M. B.; Herz, L. M. Hybrid Perovskites for Photovoltaics: Charge-Carrier Recombination, Diffusion, and Radiative Efficiencies. *Acc. Chem. Res.* **2016**, *49* (1), 146–154.

(55) Brauer, J. C.; Lee, Y. H.; Nazeeruddin, M. K.; Banerji, N. Ultrafast charge carrier dynamics in CH3NH3PbI3 evidence for hot hole injection into spiro-OMeTAD. *J. Mater. Chem. C* **2016**, *4* (25), 5922–5931.

(56) Piatkowski, P.; Cohen, B.; Javier Ramos, F.; Di Nunzio, M.; Nazeeruddin, M. K.; Grätzel, M.; Ahmad, S.; Douhal, A. Direct monitoring of ultrafast electron and hole dynamics in perovskite solar cells. *Phys. Chem. Chem. Phys.* **2015**, *17* (22), 14674–14684.

(57) Ponseca, C. S.; Hutter, E. M.; Piatkowski, P.; Cohen, B.; Pascher, T.; Douhal, A.; Yartsev, A.; Sundstroem, V.; Savenije, T. J. Mechanism of Charge Transfer and Recombination Dynamics in Organo Metal Halide Perovskites and Organic Electrodes, PCBM, and Spiro-MeOTAD: Role of Dark Carriers. *J. Am. Chem. Soc.* **2015**, *137* (51), 16043–16048.

(58) Leng, J.; Liu, J.; Zhang, J.; Jin, S. Decoupling Interfacial Charge Transfer from Bulk Diffusion Unravels Its Intrinsic Role for Efficient Charge Extraction in Perovskite Solar Cells. *J. Phys. Chem. Lett.* **2016**, *7* (24), 5056–5061.

(59) Corani, A.; Li, M.-H.; Shen, P.-S.; Chen, P.; Guo, T.-F.; El Nahhas, A.; Zheng, K.; Yartsev, A.; Sundstroem, V.; Ponseca, C. S. Ultrafast Dynamics of Hole Injection

and Recombination in Organometal Halide Perovskite Using Nickel Oxide as p-Type Contact Electrode. *J. Phys. Chem. Lett.* **2016**, *7* (7), 1096–1101.

(60) Brauer, J. C.; Lee, Y. H.; Nazeeruddin, M. K.; Banerji, N. Charge Transfer Dynamics from Organometal Halide Perovskite to Polymeric Hole Transport Materials in Hybrid Solar Cells. *J. Phys. Chem. Lett.* **2015**, *6* (18), 3675–3681.

(61) Marchioro, A.; Teuscher, J.; Friedrich, D.; Kunst, M.; van de Krol, R.; Moehl, T.; Grätzel, M.; Moser, J.-E. Unravelling the mechanism of photoinduced charge transfer processes in lead iodide perovskite solar cells. *Nat. Photonics* **2014**, *8* (3), 250–255.

(62) Lim, S. S.; Chong, W. K.; Solanki, A.; Dewi, H. A.; Mhaisalkar, S.; Mathews, N.; Sum, T. C. Modulating carrier dynamics through perovskite film engineering. *Phys. Chem. Chem. Phys.* **2016**, *18* (39), 27119–27123.

(63) Peng, B.; Yu, G.; Zhao, Y.; Xu, Q.; Xing, G.; Liu, X.; Fu, D.; Liu, B.; Tan, J. R. S.; Tang, W.; Lu, H.; Xie, J.; Deng, L.; Sum, T. C.; Loh, K. P. Achieving Ultrafast Hole Transfer at the Monolayer MoS_2 and $CH_3NH_3PbI_3$ Perovskite Interface by Defect Engineering. *ACS Nano* **2016**, *10* (6), 6383–6391.

(64) Yanagida, M.; Shimomoto, L.; Shirai, Y.; Miyano, K. Effect of carrier transport in NiO on the photovoltaic properties of lead iodide perovskite solar cells. *Electrochem. (Tokyo, Japan)* **2017**, *85* (5), 231–235.

(65) Islam, M. B.; Yanagida, M.; Shirai, Y.; Nabetani, Y.; Miyano, K. NiOx Hole Transport Layer for Perovskite Solar Cells with Improved Stability and Reproducibility. *ACS Omega* **2017**, *2* (5), 2291–2299.

(66) Tripathi, N.; Yanagida, M.; Shirai, Y.; Masuda, T.; Han, L.; Miyano, K.

Hysteresis-free and highly stable perovskite solar cells produced via a chlorine-mediated interdiffusion method. *J. Mater. Chem. A* **2015**, *3* (22), 12081–12088.

(67) Khadka, D. B.; Shirai, Y.; Yanagida, M.; Masuda, T.; Miyano, K. Enhancement in efficiency and optoelectronic quality of perovskite thin films annealed in MACl vapor. *Sustain. Energy Fuels* **2017**, *1* (4), 755–766.

(68) Oku, T. Crystal Structures of $CH_3NH_3PbI_3$ and Related Perovskite Compounds Used for Solar Cells. In *Solar Cells - New Approaches and Reviews*; InTech, 2015.

(69) Xie, Z.; Liu, S.; Qin, L.; Pang, S.; Wei, W.; Yu, Y.; Li, Y.; Chen, Z.; Wang, S.; Du, H.; Yu, M.; Qin, G. G. Refractive index and extinction coefficient of $CH_3NH_3PbI_3$ studied by spectroscopic ellipsometry. *Opt. Mater. Express* **2015**, *5* (1), 29–43.

(70) Price, M. B.; Butkus, J.; Jellicoe, T. C.; Sadhanala, A.; Briane, A.; Halpert, J. E.; Broch, K.; Hodgkiss, J. M.; Friend, R. H.; Deschler, F. Hot-carrier cooling and photoinduced refractive index changes in organic-inorganic lead halide perovskites. *Nat. Commun.* **2015**, *6*, 8420.

(71) Anand, B.; Sampat, S.; Danilov, E. O.; Peng, W.; Rupich, S. M.; Chabal, Y. J.; Gartstein, Y. N.; Malko, A. V. Broadband transient absorption study of photoexcitations in lead halide perovskites: towards a multiband picture. *Phys. Rev. B* **2016**, *93* (16), 161205/1-161205/5.

(72) Manser, J. S.; Kamat, P. V. Band filling with free charge carriers in organometal halide perovskites. *Nat. Photonics* **2014**, *8* (9), 737–743.

(73) Sum, T. C.; Mathews, N.; Xing, G.; Lim, S. S.; Chong, W. K.; Giovanni, D.; Dewi, H. A. Spectral Features and Charge Dynamics of Lead Halide Perovskites:

Origins and Interpretations. *Acc. Chem. Res.* **2016**, *49* (2), 294–302.

(74) Wehrenfennig, C.; Eperon, G. E.; Johnston, M. B.; Snaith, H. J.; Herz, L. M. High Charge Carrier Mobilities and Lifetimes in Organolead Trihalide Perovskites. *Adv. Mater.* **2014**, *26* (10), 1584–1589.

(75) Sakamoto, S.; Okumura, M.; Zhao, Z.; Furukawa, Y. Raman spectral changes of PEDOT-PSS in polymer light-emitting diodes upon operation. *Chem. Phys. Lett.* **2005**, *412* (4–6), 395–398.

(76) Endres, J.; Kulbak, M.; Zhao, L.; Rand, B. P.; Cahen, D.; Hodes, G.; Kahn, A. Electronic structure of the CsPbBr3/polytriarylamine (PTAA) system. *J. Appl. Phys.* **2017**, *121* (3), 035304/1-035304/8.

(77) Guo, Z.; Manser, J. S.; Wan, Y.; Kamat, P. V; Huang, L. Spatial and temporal imaging of long-range charge transport in perovskite thin films by ultrafast microscopy. *Nat. Commun.* **2015**, *6*, 7471.

(78) Staub, F.; Hempel, H.; Hebig, J.-C.; Mock, J.; Paetzold, U. W.; Rau, U.; Unold, T.; Kirchartz, T. Beyond bulk lifetimes: insights into lead halide perovskite films from time-resolved photoluminescence. *Phys. Rev. Appl.* **2016**, *6* (4), 044017/1-044017/13.

(79) Dong, Q.; Fang, Y.; Shao, Y.; Mulligan, P.; Qiu, J.; Cao, L.; Huang, J. Electron-hole diffusion lengths > 175 µm in solution-grown $CH_3NH_3PbI_3$ single crystals. *Science (80-.).* **2015**, *347* (6225), 967–970.

(80) Elbaz, G. A.; Straus, D. B.; Semonin, O. E.; Hull, T. D.; Paley, D. W.; Kim, P.; Owen, J. S.; Kagan, C. R.; Roy, X. Unbalanced Hole and Electron Diffusion in Lead Bromide Perovskites. *Nano Lett.* **2017**, *17* (3), 1727–1732.

(81) Semonin, O. E.; Elbaz, G. A.; Straus, D. B.; Hull, T. D.; Paley, D. W.; van der Zande, A. M.; Hone, J. C.; Kymissis, I.; Kagan, C. R.; Roy, X.; Owen, J. S. Limits of Carrier Diffusion in *n* -Type and *p* -Type $CH_3NH_3PbI_3$ Perovskite Single Crystals. *J. Phys. Chem. Lett.* **2016**, *7* (17), 3510–3518.

(82) Olthof, S.; Meerholz, K. Substrate-dependent electronic structure and film formation of $MAPbI_3$ perovskites. *Sci. Rep.* **2017**, *7*, 40267.

(83) Miyano, K.; Yanagida, M.; Tripathi, N.; Shirai, Y. Hysteresis, Stability, and Ion Migration in Lead Halide Perovskite Photovoltaics. *J. Phys. Chem. Lett.* **2016**, *7* (12), 2240–2245.

(84) Khadka, D. B.; Shirai, Y.; Yanagida, M.; Ryan, J. W.; Miyano, K. Exploring the effects of interfacial carrier transport layers on device performance and optoelectronic properties of planar perovskite solar cells. *J. Mater. Chem. C* **2017**, *5* (34), 8819–8827.

(85) Chava, V. S. N.; Omar, S. U.; Brown, G.; Shetu, S. S.; Andrews, J.; Sudarshan, T. S.; Chandrashekhar, M. V. S. Evidence of minority carrier injection efficiency >90% in an epitaxial graphene/SiC Schottky emitter bipolar junction phototransistor for ultraviolet detection. *Appl. Phys. Lett.* **2016**, *108* (4).

(86) Davydov, S. Y.; Lebedev, A. A.; Posrednik, O. V. Estimation of the energy characteristics of the 3C-SiC/2H-, 4H-, 6H-, and 8H-SiC heterojunctions. *Semiconductors* **2005**, *39* (12), 1391–1393.

(87) Kakanakova-Georgieva, A.; Yakimova, R.; Henry, A.; Linnarsson, M. K.; Syväjärvi, M.; Janzén, E. Cathodoluminescence identification of donor-acceptor related emissions in as-grown 4H-SiC layers. *J. Appl. Phys.* **2002**, *91* (5), 2890–

2895.

(88) Omar, S. U.; Song, H. Z.; Sudarshan, T. S.; Chandrashekhar, M. V. S. Room Temperature Photoluminescence from 4H-SiC Epilayers: Non-Destructive Estimation of In-Grown Stacking Fault Density. *Mater. Sci. Forum* **2012**, *717–720* (May), 399–402.

(89) Chandrashekhar, M. V. S.; Chowdhury, I.; Kaminski, P.; Kozlowski, R.; Klein, P. B.; Sudarshan, T. High Purity Semi-Insulating 4H-SiC Epitaxial Layers by Defect-Competition Epitaxy: Controlling Si Vacancies. *Appl. Phys. Express* **2012**, *5* (2), 25502.

(90) Coletti, C.; Forti, S.; Principi, A.; Emtsev, K. V.; Zakharov, A. A.; Daniels, K. M.; Daas, B. K.; Chandrashekhar, M. V. S.; Ouisse, T.; Chaussende, D.; MacDonald, A. H.; Polini, M.; Starke, U. Revealing the electronic band structure of trilayer graphene on SiC: An angle-resolved photoemission study. *Phys. Rev. B* **2013**, *88* (15), 155439.

(91) Daniels, K. M.; Jadidi, M. M.; Sushkov, A. B.; Nath, A.; Boyd, A. K.; Sridhara, K.; Drew, H. D.; Murphy, T. E.; Myers-Ward, R. L.; Gaskill, D. K. Narrow plasmon resonances enabled by quasi-freestanding bilayer epitaxial graphene. *2D Mater.* **2017**, *4* (2), 25034.

(92) Coletti, C.; Riedl, C.; Lee, D. S.; Krauss, B.; Patthey, L.; von Klitzing, K.; Smet, J. H.; Starke, U. Charge neutrality and band-gap tuning of epitaxial graphene on SiC by molecular doping. *Phys. Rev. B* **2010**, *81* (23), 235401.

(93) Sridhara, S. G.; Devaty, R. P.; Choyke, W. J. Absorption cofficient of 4H silicon carbide from 3900 to 3950 Å. *Math. Intell.* **1998**, *20* (2), 54.

(94) Grekov, A.; Maximenko, S.; Sudarshan, T. S. Effect of basal plane dislocations on characteristics of difused 4H-SiC p-i-n diodes. *IEEE Trans. Electron Devices* **2005**, *52* (12), 2546–2551.

(95) Mahadik, N. A.; Stahlbush, R. E.; Ancona, M. G.; Imhoff, E. A.; Hobart, K. D.; Myers-Ward, R. L.; Eddy, C. R.; Kurt Gaskill, D.; Kub, F. J. Observation of stacking faults from basal plane dislocations in highly doped 4H-SiC epilayers. *Appl. Phys. Lett.* **2012**, *100* (4).

(96) Harris, G. L. *Properties of silicon carbide*; 1995; Vol. 93.

(97) Feng, G.; Suda, J.; Kimoto, T. Triple Shockley type stacking faults in 4H-SiC epilayers. *Appl. Phys. Lett.* **2009**, *94* (9).

(98) Feng, G.; Suda, J.; Kimoto, T. Characterization of stacking faults in 4H-SiC epilayers by roomerature microphotoluminescence mapping. *Appl. Phys. Lett.* **2008**, *92* (22), 1–4.

(99) Larkin, D. J.; Neudeck, P. G.; Powell, J. A.; Matus, L. G. Site-competition epitaxy for superior silicon carbide electronics. *Appl. Phys. Lett.* **1994**, *65* (13), 1659–1661.

(100) Helava, H.; N. Mokhov, E.; A. Avdeev, O.; Ramm, M.; Litvin, D.; V. Vasiliev, A.; D. Roenkov, A.; S. Nagalyuk, S.; Makarov, Y. Growth of Low-Defect SiC and AlN Crystals in Refractory Metal Crucibles. *Mater. Sci. Forum* **2013**, *740–742*, 85–90.

(101) Schaffer, W. J.; Negley, G. H.; Irvine, K. G.; Palmour, J. W. CONDUCTIVITY ANISOTROPY IN EPITAXIAL 6H AND 4H SiC. *Mater. Res.* **2017**, *339* (1), 595–600.

(102) Hayashi, T.; Asano, K.; Suda, J.; Kimoto, T. Impacts of reduction of deep levels and surface passivation on carrier lifetimes in p-type 4H-SiC epilayers. *J. Appl. Phys.* **2011**, *109* (11).

(103) Riedl, C.; Coletti, C.; Starke, U. Structural and electronic properties of epitaxial graphene on SiC(0 0 0 1): a review of growth, characterization, transfer doping and hydrogen intercalation. *J. Phys. D. Appl. Phys.* **2010**, *43* (37), 374009.

(104) Nomani, M. W. K.; Shields, V.; Tompa, G.; Sbrockey, N.; Spencer, M. G.; Webb, R. A.; Koley, G. Correlated conductivity and work function changes in epitaxial graphene. *Appl. Phys. Lett.* **2012**, *100* (9).

(105) Chen, J.-W.; Huang, H.-C.; Convertino, D.; Coletti, C.; Chang, L.-Y.; Shiu, H.-W.; Cheng, C.-M.; Lin, M.-F.; Heun, S.; Chien, F. S.-S.; Chen, Y.-C.; Chen, C.-H.; Wu, C.-L. Efficient n-type doping in epitaxial graphene through strong lateral orbital hybridization of Ti adsorbate. *Carbon N. Y.* **2016**, *109*, 300–305.

(106) Emtsev, K. V.; Zakharov, A. A.; Coletti, C.; Forti, S.; Starke, U. Ambipolar doping in quasifree epitaxial graphene on SiC(0001) controlled by Ge intercalation. *Phys. Rev. B* **2011**, *84* (12), 125423.

(107) Dubrovskii, G. B.; Lepneva, A. A.; Radovanova, E. I. Optical absorption associated with superlattice in silicon carbide crystals. *Phys. Status Solidi* **1973**, *57* (1), 423–431.

(108) Chandrashekhar, M. V. S.; Thomas, C. I.; Lu, J.; Spencer, M. G. Electronic properties of a 3C/4H SiC polytype heterojunction formed on the Si face. *Appl. Phys. Lett.* **2007**, *90* (17), 1–4.

(109) Chandrashekhar, M. V. S.; Thomas, C. I.; Lu, J.; Spencer, M. G. Observation of a

two dimensional electron gas formed in a polarization doped C-face 3C/4H SiC heteropolytype junction. *Appl. Phys. Lett.* **2007**, *91* (3), 1–4.

(110) Lu, J.; Chandrashekhar, M. V. S.; Parks, J. J.; Ralph, D. C.; Spencer, M. G. Quantum confinement and coherence in a two-dimensional electron gas in a carbon-face 3C-SiC/6H-SiC polytype heterostructure. *Appl. Phys. Lett.* **2009**, *94* (16).

(111) Ambacher, O.; Foutz, B.; Smart, J.; Shealy, J. R.; Weimann, N. G.; Chu, K.; Murphy, M.; Sierakowski, A. J.; Schaff, W. J.; Eastman, L. F.; Dimitrov, R.; Mitchell, A.; Stutzmann, M. Two dimensional electron gases induced by spontaneous and piezoelectric polarization in undoped and doped AlGaN/GaN heterostructures. *J. Appl. Phys.* **2000**, *87* (1), 334–344.

(112) Brown, J. D.; Borges, R.; Piner, E.; Vescan, A.; Singhal, S.; Therrien, R. AlGaN/GaN HFETs fabricated on 100-mm GaN on silicon (111) substrates. *Solid. State. Electron.* **2002**, *46* (10), 1535–1539.

(113) Levine, B. F. Quantum-well infrared photodetectors. *J. Appl. Phys.* **1993**, *74* (8).

(114) Fissel, A. Artificially layered heteropolytypic structures based on SiC polytypes: Molecular beam epitaxy, characterization and properties. *Phys. Rep.* **2003**, *379* (3–4), 149–255.

(115) Anderson, T. J.; Hobart, K. D.; Greenlee, J. D.; Shahin, D. I.; Koehler, A. D.; Tadjer, M. J.; Imhoff, E. A.; Myers-Ward, R. L.; Christou, A.; Kub, F. J. Ultraviolet detector based on graphene/SiC heterojunction. *Appl. Phys. Express* **2015**, *8* (4), 41301.

(116) Barker, B. G.; Chava, V. S. N.; Daniels, K. M.; Chandrashekhar, M. V. S.;

Greytak, A. B. Sub-bandgap response of graphene/SiC Schottky emitter bipolar phototransistor examined by scanning photocurrent microscopy. *2D Mater.* **2018**, *5* (1).

(117) Rana, T.; Chandrashekhar, M. V. S.; Daniels, K.; Sudarshan, T. Epitaxial growth of graphene on SiC by Si selective etching using SiF4 in an inert ambient. *Jpn. J. Appl. Phys.* **2015**, *54*.

(118) Sridhara, S. .; Eperjesi, T. .; Devaty, R. .; Choyke, W. . Penetration depths in the ultraviolet for 4H, 6H and 3C silicon carbide at seven common laser pumping wavelengths. *Mater. Sci. Eng. B* **1999**, *61–62*, 229–233.

(119) Balachandran, A.; Song, H. Z.; Sudarshan, T. S.; Shetu, S. S.; Chandrashekhar, M. V. S. Study of SiC Epitaxial Growth Using Tetrafluorosilane and Dichlorosilane in Vertical Hotwall CVD Furnace. *Mater. Sci. Forum* **2015**, *821–823*, 137–140.

(120) Balachandran, A. High Quality Low Offcut 4H-SiC Epitaxy and Integrated Growth of Epitaxial Graphene for Hybrid Graphene/SiC Devices, University of South Carolina, 2017.

(121) Balachandran, A.; Song, H.; Sudarshan, T. S.; Chandrashekhar, M. V. S. 4H–SiC homoepitaxy on nearly on-axis substrates using TFS-towards high quality epitaxial growth. *J. Cryst. Growth* **2016**, *448*, 97–104.

(122) Chen, X.; Zhu, H.; Cai, J.; Wu, Z. High-performance 4H-SiC-based ultraviolet p-i-n photodetector. *J. Appl. Phys.* **2007**, *102* (2), 24505.

(123) Baliga, B. J. *Fundamentals of Power Semiconductor Devices*; Springer US: Boston, MA, 2008.

(124) Monroy, E.; Omnès, F.; Calle, F. Wide-bandgap semiconductor ultraviolet

photodetectors. *Semicond. Sci. Technol.* **2003**, *18* (4), R33–R51.

(125) Sze, S. M.; Ng, K. K. *Physics of Semiconductor Devices*; John Wiley & Sons, Inc.: Hoboken, NJ, USA, 2006.

(126) Kimoto, T.; Cooper, J. A. *Fundamentals of Silicon Carbide Technology*; John Wiley & Sons Singapore Pte. Ltd: Singapore, 2014.

(127) Osinsky, A.; Gangopadhyay, S.; Lim, B. W.; Anwar, M. Z.; Khan, M. A.; Kuksenkov, D. V.; Temkin, H. Schottky barrier photodetectors based on AlGaN. *Appl. Phys. Lett.* **1998**, *72* (6), 742.

(128) Osinsky, A.; Gangopadhyay, S.; Yang, J. W.; Gaska, R.; Kuksenkov, D.; Temkin, H.; Shmagin, I. K.; Chang, Y. C.; Muth, J. F.; Kolbas, R. M. Visible-blind GaN Schottky barrier detectors grown on Si(111). *Appl. Phys. Lett.* **1998**, *72* (5), 551.

(129) Mazzillo, M.; Condorelli, G.; Castagna, M. E.; Catania, G.; Sciuto, A.; Roccaforte, F.; Raineri, V. Highly Efficient Low Reverse Biased 4H-SiC Schottky Photodiodes for UV-Light Detection. *IEEE Photonics Technol. Lett.* **2009**, *21* (23), 1782–1784.

(130) Bai, X.; Guo, X.; Mcintosh, D. C.; Liu, H.-D.; Campbell, J. C. High Detection Sensitivity of Ultraviolet 4H-SiC Avalanche Photodiodes. *IEEE J. Quantum Electron.* **2007**, *43* (12), 1159–1162.

(131) Muhtadi, S.; Hwang, S. M.; Coleman, A. L.; Lunev, A.; Asif, F.; Chava, V. S. N.; Chandrashekhar, M. V. S.; Khan, A. High-speed solar-blind UV photodetectors using high-Al content $Al_{0.64}Ga_{0.36}N/Al_{0.34}Ga_{0.66}N$ multiple quantum wells. *Appl. Phys. Express* **2017**, *10* (1), 11004.

(132) Beck, A. L.; Yang, B.; Guo, X.; Campbell, J. C. Edge Breakdown in 4H-SiC

Avalanche Photodiodes. *IEEE J. Quantum Electron.* **2004**, *40* (3), 321–324.

(133) Guo, X.; Beck, A. L.; Huang, Z.; Duan, N.; Campbell, J. C.; Emerson, D.; Sumakeris, J. J. Performance of Low-Dark-Current 4H-SiC Avalanche Photodiodes With Thin Multiplication Layer. *IEEE Trans. Electron Devices* **2006**, *53* (9), 2259–2265.

(134) Campbell, J. C. Recent Advances in Telecommunications Avalanche Photodiodes. *J. Light. Technol.* **2007**, *25* (1), 109–121.

(135) Konstantatos, G.; Sargent, E. H. Solution-Processed Quantum Dot Photodetectors. *Proc. IEEE* **2009**, *97* (10), 1666–1683.

(136) Konstantatos, G.; Badioli, M.; Gaudreau, L.; Osmond, J.; Bernechea, M.; de Arquer, F. P. G.; Gatti, F.; Koppens, F. H. L. Hybrid graphene–quantum dot phototransistors with ultrahigh gain. *Nat. Nanotechnol.* **2012**, *7* (6), 363–368.

(137) Sun, Z.; Liu, Z.; Li, J.; Tai, G.; Lau, S.-P.; Yan, F. Infrared Photodetectors Based on CVD-Grown Graphene and PbS Quantum Dots with Ultrahigh Responsivity. *Adv. Mater.* **2012**, *24* (43), 5878–5883.

(138) Chang, H.; Lv, X.; Zhang, H.; Li, J. Quantum dots sensitized graphene: In situ growth and application in photoelectrochemical cells. *Electrochem. commun.* **2010**, *12* (3), 483–487.

(139) Song, H.; Chandrashekhar, M. V. S.; Sudarshan, T. S. Study of Surface Morphology, Impurity Incorporation and Defect Generation during Homoepitaxial Growth of 4H-SiC Using Dichlorosilane. *ECS J. Solid State Sci. Technol.* **2014**, *4* (3), P71–P76.

(140) Daas, B. K.; Daniels, K. M.; Sudarshan, T. S.; Chandrashekhar, M. V. S. Polariton

enhanced infrared reflection of epitaxial graphene. *J. Appl. Phys.* **2011**, *110* (11), 113114.

(141) Kim, J. Y.; Voznyy, O.; Zhitomirsky, D.; Sargent, E. H. 25th Anniversary Article: Colloidal Quantum Dot Materials and Devices: A Quarter-Century of Advances. *Adv. Mater.* **2013**, *25* (36), 4986–5010.

(142) De Iacovo, A.; Venettacci, C.; Colace, L.; Scopa, L.; Foglia, S. PbS Colloidal Quantum Dot Photodetectors operating in the near infrared. *Sci. Rep.* **2016**, *6* (1), 37913.

(143) Miller, E. M.; Kroupa, D. M.; Zhang, J.; Schulz, P.; Marshall, A. R.; Kahn, A.; Lany, S.; Luther, J. M.; Beard, M. C.; Perkins, C. L.; Van De Lagemaat, J. Revisiting the Valence and Conduction Band Size Dependence of PbS Quantum Dot Thin Films. *ACS Nano* **2016**, *10*, 3302–3311.

(144) Hetsch, F.; Zhao, N.; Kershaw, S. V.; Rogach, A. L. Quantum dot field effect transistors. *Mater. Today* **2013**, *16* (9), 312–325.

(145) Shevchenko, E. V.; Talapin, D. V.; O'Brien, S.; Murray, C. B. Polymorphism in AB_{13} Nanoparticle Superlattices: An Example of Semiconductor−Metal Metamaterials. *J. Am. Chem. Soc.* **2005**, *127* (24), 8741–8747.

(146) Wagner, R. S.; Ellis, W. C. VAPOR-LIQUID-SOLID MECHANISM OF SINGLE CRYSTAL GROWTH. *Appl. Phys. Lett.* **1964**, *4* (5), 89–90.

(147) Lu, W.; Lieber, C. M. Semiconductor nanowires. *J. Phys. D. Appl. Phys.* **2006**, *39* (21), R387–R406.

(148) Mishra, U. K.; Singh, J. *Semiconductor Device Physics and Design*; Springer, 2008.

(149) Liu, G.; Schulmeyer, T.; Brötz, J.; Klein, A.; Jaegermann, W. Interface properties and band alignment of Cu_2S/CdS thin film solar cells. *Thin Solid Films* **2003**, *431–432*, 477–482.

(150) Soci, C.; Zhang, A.; Xiang, B.; Dayeh, S. A.; Aplin, D. P. R.; Park, J.; Bao, X. Y.; Lo, Y. H.; Wang, D. ZnO Nanowire UV Photodetectors with High Internal Gain. *Nano Lett.* **2007**, *7* (4), 1003–1009.

(151) Bao, J.; Shalish, I.; Su, Z.; Gurwitz, R.; Capasso, F.; Wang, X.; Ren, Z. Photoinduced oxygen release and persistent photoconductivity in ZnO nanowires. *Nanoscale Res. Lett.* **2011**, *6* (1), 404.

(152) Lu, M.-P.; Lu, M.-Y.; Chen, L.-J. Multibit Programmable Optoelectronic Nanowire Memory with Sub-femtojoule Optical Writing Energy. *Adv. Funct. Mater.* **2014**, *24* (20), 2967–2974.

(153) Paul, G. S.; Agarwal, P. Persistent photocurrent and decay studies in CdS nanorods thin films. *J. Appl. Phys.* **2009**, *106* (10), 103705.

(154) Zhang, J.; Crisp, R. W.; Gao, J.; Kroupa, D. M.; Beard, M. C.; Luther, J. M. Synthetic Conditions for High-Accuracy Size Control of PbS Quantum Dots. *J. Phys. Chem. Lett.* **2015**, *6* (10), 1830–1833.

(155) Shen, Y.; Gee, M. Y.; Greytak, A. B. Purification technologies for colloidal nanocrystals. *Chem. Commun.* **2017**, *53* (5), 827–841.

(156) Jeong, K. S.; Tang, J.; Liu, H.; Kim, J.; Schaefer, A. W.; Kemp, K.; Levina, L.; Wang, X.; Hoogland, S.; Debnath, R.; Brzozowski, L.; Sargent, E. H.; Asbury, J. B. Enhanced Mobility-Lifetime Products in PbS Colloidal Quantum Dot Photovoltaics. *ACS Nano* **2012**, *6* (1), 89–99.

(157) Klem, E. J. D.; Shukla, H.; Hinds, S.; MacNeil, D. D.; Levina, L.; Sargent, E. H. Impact of dithiol treatment and air annealing on the conductivity, mobility, and hole density in PbS colloidal quantum dot solids. *Appl. Phys. Lett.* **2008**, *92* (21), 212105.

(158) Luther, J. M.; Law, M.; Song, Q.; Perkins, C. L.; Beard, M. C.; Nozik, A. J. Structural, Optical, and Electrical Properties of Self-Assembled Films of PbSe Nanocrystals Treated with 1,2-Ethanedithiol. *ACS Nano* **2008**, *2* (2), 271–280.

(159) Voznyy, O.; Zhitomirsky, D.; Stadler, P.; Ning, Z.; Hoogland, S.; Sargent, E. H. A Charge-Orbital Balance Picture of Doping in Colloidal Quantum Dot Solids. *ACS Nano* **2012**, *6* (9), 8448–8455.

APPENDIX A – COPYRIGHT PERMISSIONS

Title:	Direct Observation of Ultrafast Hole Injection from Lead Halide Perovskite by Differential Transient Transmission Spectroscopy
Author:	Kunie Ishioka, Bobby G. Barker, Masatoshi Yanagida, et al
Publication:	Journal of Physical Chemistry Letters
Publisher:	American Chemical Society
Date:	Aug 1, 2017

Copyright © 2017, American Chemical Society

LOGIN

If you're a copyright.com user, you can login to RightsLink using your copyright.com credentials.

Already **a RightsLink user** or want to learn more?

PERMISSION/LICENSE IS GRANTED FOR YOUR ORDER AT NO CHARGE

This type of permission/license, instead of the standard Terms & Conditions, is sent to you because no fee is being charged for your order. Please note the following:

- Permission is granted for your request in both print and electronic formats, and translations.
- If figures and/or tables were requested, they may be adapted or used in part.
- Please print this page for your records and send a copy of it to your publisher/graduate school.
- Appropriate credit for the requested material should be given as follows: "Reprinted (adapted) with permission from (COMPLETE REFERENCE CITATION). Copyright (YEAR) American Chemical Society." Insert appropriate information in place of the capitalized words.
- One-time permission is granted only for the use specified in your request. No additional uses are granted (such as derivative works or other editions). For any other uses, please submit a new request.

BACK CLOSE WINDOW

Copyright © 2018 Copyright Clearance Center, Inc. All Rights Reserved. Privacy statement. Terms and Conditions.
Comments? We would like to hear from you. E-mail us at customercare@copyright.com

Title:	2D materials
Article ID:	2053-1583
Publication:	Publication1
Publisher:	CCC Republication
Date:	Jan 1, 2014

Copyright © 2014, CCC Republication

Logged in as:
Bobby Barker
University of South Carolina
Account #:
3001246422
LOGOUT

Order Completed

Thank you for your order.

This Agreement between Bobby G Barker ("You") and IOP Publishing ("IOP Publishing") consists of your order details and the terms and conditions provided by IOP Publishing and Copyright Clearance Center.

License number	Reference confirmation email for license number
License date	Feb, 25 2018
Licensed content publisher	IOP Publishing
Licensed content title	2D materials
Licensed content date	Jan 1, 2014
Type of use	Thesis/Dissertation
Requestor type	Author of requested content
Format	Print, Electronic
Portion	chapter/article
The requesting person/organization	Bobby G. Barker Jr.
Title or numeric reference of the portion(s)	Chapter 3
Title of the article or chapter the portion is from	Sub-bandgap response of graphene/SiC Schottky emitter bipolar phototransistor examined by scanning photocurrent microscopy
Editor of portion(s)	N/A
Author of portion(s)	Bobby G. Barker Jr.
Volume of serial or monograph	N/A
Page range of portion	
Publication date of portion	May 2018
Rights for	Main product and any product related to main product
Duration of use	Life of current and all future editions
Creation of copies for the disabled	no
With minor editing privileges	yes
For distribution to	Worldwide
In the following language(s)	Original language of publication
With incidental promotional use	no
Lifetime unit quantity of new product	Up to 999
Title	Sub-bandgap response of graphene/SiC Schottky emitter bipolar phototransistor examined by scanning photocurrent microscopy
Instructor name	Andrew Greytak
Institution name	University of South Carolina
Expected presentation date	May 2018
Requestor Location	University of South Carolina 1000 Whaley St Apt 4066 Columbia, SC 29201 United States Attn: University of South Carolina
Billing Type	Invoice
Billing address	University of South Carolina 1000 Whaley St Apt 4066 Columbia, SC 29201 United States Attn: Bobby G Barker
Total (may include CCC user fee)	0.00 USD
Total	0.00 USD

CLOSE WINDOW

Copyright © 2018 Copyright Clearance Center, Inc. All Rights Reserved. Privacy statement. Terms and Conditions.
Comments? We would like to hear from you. E-mail us at customercare@copyright.com

AIP PUBLISHING LICENSE
TERMS AND CONDITIONS

Apr 19, 2018

This Agreement between University of South Carolina -- Bobby Barker ("You") and AIP Publishing ("AIP Publishing") consists of your license details and the terms and conditions provided by AIP Publishing and Copyright Clearance Center.

License Number	4325481057008
License date	Apr 10, 2018
Licensed Content Publisher	AIP Publishing
Licensed Content Publication	Applied Physics Letters
Licensed Content Title	High detectivity visible-blind SiF4 grown epitaxial graphene/SiC Schottky contact bipolar phototransistor
Licensed Content Author	Venkata S. N. Chava, Bobby G. Barker, Anusha Balachandran, et al
Licensed Content Date	Dec 11, 2017
Licensed Content Volume	111
Licensed Content Issue	24
Type of Use	Thesis/Dissertation
Requestor type	Author (original article)
Format	Print and electronic
Portion	Excerpt (> 800 words)
Will you be translating?	No
Order reference number	CAO2744
Title of your thesis / dissertation	Investigation of the Spatial Dependence of Carrier Dynamics in Semiconductor Optoelectronic Devices
Expected completion date	Apr 2018
Estimated size (number of pages)	159
Requestor Location	University of South Carolina 1000 Whaley St Apt 4066 Columbia, SC 29201 United States Attn: University of South Carolina
Billing Type	Invoice
Billing Address	University of South Carolina 1000 Whaley St Apt 4066 Columbia, SC 29201 United States Attn: Bobby G Barker
Total	0.00 USD

Terms and Conditions

AIP Publishing -- Terms and Conditions: Permissions Uses